

Aus der Chirurgische Klinik der Medizinischen Fakultät Mannheim
(Direktor: Prof. Dr. Med Christoph Reissfelder)

Photobiomodulation of blue light irradiation on human keratinocytes,
fibroblasts, and endothelial cells involved in wound healing and
angiogenesis

Inauguraldissertation
zur Erlangung des Doctor scientiarum humanarum (Dr. sc. hum.)
der
Medizinischen Fakultät Mannheim
der Ruprecht-Karls-Universität
zu
Heidelberg

vorgelegt von
Jingbo Shao

aus
Jiangsu, China
2025

Dekan: Prof. Dr. med. Sergij Goerdt
Referent: PD Dr. med. Patrick Téoule

CONTENTS

	Page
ABBREVIATIONS	1
1 INTRODUCTION	3
1.1 Role and structure of human skin	3
1.2 Complexity and demands for wound healing	4
1.3 Phases of wound healing	5
1.3.1 Keratinocytes and their role in re-epithelialization	6
1.3.2 Fibroblasts and their function of producing ECM	6
1.3.3 Endothelial cells and angiogenesis	7
1.4 Concept and mechanism of photobiomodulation	9
1.5 Light-emitting diode light	10
1.6 Wound managements and clinical applications of blue light on wound healing	11
1.7 Aim of the study	11
2 MATERIAL AND METHODS	13
2.1 Material	13
2.1.1 Blue light device	13
2.1.2 Device for temperature measurement	15
2.1.3 Photodiode-based device	15
2.1.4 Consumables	16
2.1.5 Chemicals and reagents	17
2.1.6 Instruments	17
2.1.7 Software	18
2.2 Methods	18
2.2.1 Blue light irradiation	18
2.2.2 Cell lines and cell culture	20
2.2.3 Temperature measurements	23
2.2.4 The distribution of light intensity	25
2.2.5 Cell viability assay	25

2.2.6 Cell proliferation assay	26
2.2.7 ATP quantification	26
2.2.8 Migration assay	27
2.2.9 Apoptosis assay	28
2.2.10 Cell viability assays after medium irradiation and refreshment	29
2.2.11 Gene expression analysis	30
2.2.12 Statistical analysis	32
3 RESULTS	33
3.1 LED-based BLI prototype	33
3.1.1 Temperature measurements	33
3.1.2 Distribution of light intensities	36
3.2 Effects of BLI on cell viability and proliferation with different irradiances	38
3.3 Long-term BLI on three cell types	42
3.3.1 BLI utilizing 10 mW/cm ² irradiance for 7h	42
3.3.2 BLI utilizing 23 mW/cm ² irradiance for long-time irradiation	43
3.3.3 Sequential light treatments	44
3.3.4 Cell viability after alteration of cell culture conditions	50
3.4 Effects of BLI on ATP quantification	53
3.5 Effects of the low-fluence irradiation (4.5 J/cm ²) on cell migration	54
3.6 Effect of 4.5 and and 18 J/cm ² BLI on cell apoptosis	58
3.7 Gene expression analysis after RNA sequencing	60
4 DISCUSSION	67
4.1 Influence of BLI on cell lines of HaCaT, NHDF and HUVEC	67
4.2 Experimental settings of temperature measurements	67
4.3 New LED-based BLI prototype	68
4.4 PBM after BLI on HaCaTs	69
4.5 PBM after BLI on NHDF	70
4.6 PBM after BLI on HUVEC	72
4.7 The inhibitory effect after BLI on cell lines	73
4.8 The influence from cell culture condition and treatment protocol	75

5 SUMMARY	77
6 REFERENCES	79
7 APPENDIX	93
8 CURRICULUM VITAE AND PUBLICATIONS	96
9 ACKNOWLEDGEMENT	98

ABBREVIATIONS

aBL	Antimicrobial blue light
Ang-1	Angiopoietin-1
ATP	Adenosine triphosphate
BLI	Blue light irradiation
BP	Biological process
BrdU	5-Bromo-2-deoxyuridine
CCO	Cytochrome c oxydase
DMEM	Dulbecco's modified Eagle medium
DPBS	Dulbecco's Phosphate-Buffered Saline
EC	Endothelial cell
ECM	Extracellular matrix
EGF	Epidermal growth factor
EREG	Epiregulin
FAD	Flavin adenine dinucleotide
FBS	Fetal bovine serum
FC	Fold change
FDR	False discovery rate
FGF	Fibroblast growth factor
FMN	Flavin mononucleotide
GAGs	Glycosaminoglycans
GO	Gene Ontology
GSEA	Gene set enrichment analysis
h	Hours
HA	Hyaluronic acid
HaCaT	Human immortalized keratinocyte cell line
HUVEC	Human umbilical vein endothelial cell
IGF	Insulin-like growth factor
IL-1	Interleukin-1
IL-6	Interleukin-6
ILs	Interleukins
IQR	Interquartile range

ABBREVIATIONS

J	Joules
LED	Light emitting diode
LLLT	Low-level laser therapy
m	milli
MCC	Maximal clique centrality
min	minutes
MMPs	Matrix metalloproteinases
NES	Normalized enrichment score
NHDF	Normal human dermal fibroblast
NIR	Near-infrared
NO	Nitric oxide
OPNs	Opsins
PBM	Photobiomodulation
PDGF	Platelet-derived growth factor
PI	Propidium iodide
PMS	N-methyl dibenzopyrazine methyl sulfate
PPI	Protein-protein interaction
RIN	RNA integrity
ROS	Reactive oxygen species
RT	Room temperature
SD	Standard deviation
SDH	Succinate dehydrogenase
SMCs	Smooth muscle cells
STRING	Search Tool for the Retrieval of Interacting Genes
TGF- β	Transforming growth factor beta
TNF- α	Tumour necrosis factor alpha
TRP	Transient receptor potential
TSP	Thrombospondin
VEGF	Vascular endothelial growth factor
W	Watt
XTT	Sodium 3'-[1-(phenylaminocarbonyl)-3, 4-tetrazolium] bis (4-methoxy-6-nitro) benzene sulfonic acid hydrate

1 INTRODUCTION

1.1 Role and structure of human skin

As the largest organ, the skin serves as the first barrier, shielding humans from various pathogens and hazardous substances from the external environment, for example, ultraviolet irradiation and allergen ¹⁻³. Moreover, it plays a critical role in preventing moisture loss and acting as a sensory organ (touch, temperature detection) ^{4, 5}.

The epidermis, dermis, and hypodermis are the three distinct layers that make up the skin (Figure 1) ^{6, 7}. We refer to the outermost layer of our skin as the stratum corneum, where completely differentiated keratinocytes (corneocytes) reside after gradually losing their nucleus and other organelles and simultaneously migrating to the stratum corneum ⁸⁻¹⁰. The differentiation, migration, and desquamation of keratinocytes are continuous and make the epidermis in a stable state ¹¹. Beneath the epidermis lies the dermis, where fibroblasts and extracellular matrix (ECM) are the main components. Collagenous fibres, as the major component (70%) of ECM that is produced by fibroblasts, play an essential role in providing a scaffold of connective tissue ^{7, 12-14}. The adjacent elastic fibers, as the main resilient component of elastic connective tissue, offer elasticity and flexibility ^{15, 16}. There are macrophages, dendritic cells, and mast cells involved in the immune and inflammatory response distributed on this layer ^{17, 18}. Meanwhile, numerous vessels originating from subcutaneous tissues supply hair follicles, sweat glands, sebaceous glands and sensory nerve endings ^{19, 20}. In addition to skin nutrition, arteriovenous anastomoses are found throughout the skin, and these direct shuntings between arteries and veins play a crucial role in thermal regulation by rapid blood flow ²¹. The lymphatic system within the dermis allows nutrient and oxygen delivery between different layers ^{22, 23}. It can also regulate interstitial pressure, facilitate immunological response, and eliminate waste ^{24, 25}. On the innermost layer of our skin is hypodermis, where networks of adipocytes are organized into lobules ²⁶. There are many connections between dermis and hypodermis by interconnecting collagen and elastin fibers ²⁷. The primary functions of the hypodermis are heat insulation as well as protecting the organism from physical shock ^{28, 29}. Under certain circumstances, the high energy storage of adipocytes is necessary to ensure survival ³⁰.

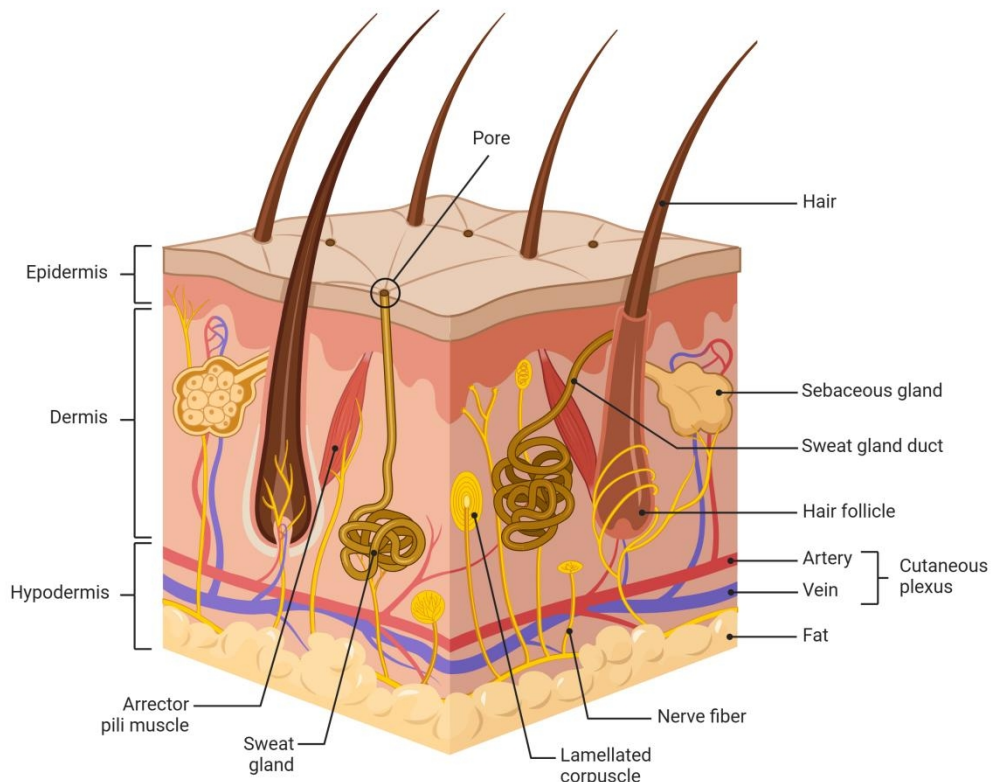


Figure 1. The structure of skin and the main components of three layers: epidermis, dermis, and hypodermis.

1.2 Complexity and demands for wound healing

A wound is the result of injuries to the skin caused by sharp or blunt trauma. Wound healing, as a spontaneous response for all multicellular organisms, is regarded as a series of biological reactions to prevent the deterioration of injury ^{31, 32}. During the process, there is extensive coordination among cell lines and interaction with the microenvironment, which is comprised of growth factors, chemokines, and ECM ³³⁻³⁶. Throughout the entire process of wound healing, these signals and structures play a critical role in transduction, communication, and feedback on the regulation and control mechanisms after injuries ^{37, 38}.

Although wound healing is an intricate process influenced by various systemic and external factors, it is not a problem in a healthy population ³⁹. While in a pathological state, several factors, such as age, obesity, circulatory disease, and metabolic disease, impede wound healing ³⁹⁻⁴¹. Furthermore, local tissue conditions, such as wound pressure or bacterial infection, also have a negative impact on wound healing ⁴². Due to the aging population, increasing incidence of chronic venous insufficiency,

peripheral artery disease, and diabetes worldwide, the burden of chronic wounds will therefore increase and significantly affect the health care system ⁴³. Despite significant advances in the understanding of wound healing mechanisms and the availability of several moderately effective wound care therapies, the demand for effective wound healing therapies is increasing and unmet ^{44, 45}.

1.3 Phases of wound healing

Wound healing is a complex and dynamic process involving several cellular and biochemical events after skin integrity is impaired ^{35, 46}. There are four sequential but overlapping stages: hemostasis, inflammation, proliferation, and remodeling ⁴⁷. In terms of angiogenesis, several growth factors, such as vascular endothelial growth factor (VEGF), platelet-derived growth factor (PDGF), and fibroblast growth factor (FGF), are mobilized to mediate angiogenic responses ^{48, 49}. With more growth factors released, the overexpression of stimulatory factors triggers the release of inhibitory factors like angiostatin and steroids ⁵⁰. Initially, skin injury exposes the dermis, activating the coagulation cascade through intrinsic and extrinsic pathways to prevent blood loss and ensure vascular integrity (Figure 2A) ⁵¹. After coagulation, a provisional matrix is gradually formed for the cell migration in the subsequent phases of wound healing ^{13, 52}. The release of cytokines and growth factors, such as PDGF, transforming growth factor beta (TGF- β), epidermal growth factor (EGF), and insulin-like growth factor (IGF), which act as promoters to initiate an inflammatory response immediately after injuries ⁵³. Neutrophils are the first immune cells to arrive at the site of the injury ^{54, 55}. They not only remove bacteria from the injury site but also produce inflammatory mediators that lead to dilation of the blood vessels and chemotaxis of monocytes from the adjacent tissue (Figure 2B) ⁵⁶. Monocytes transform into activated macrophages that release several factors, such as tumour necrosis factor alpha (TNF- α), TGF- β , and various interleukins (ILs) that stimulate fibroblasts and keratinocytes to proliferate and facilitate angiogenesis (Figure 2C) ⁵⁷. The remodeling phase is characterized by a balance between the synthesis and degradation of collagen, along with a replacement of fibronectin-rich matrices with scar tissues ^{52, 58}. Matrix metalloproteinases (MMPs) are responsible for the degradation of collagen ⁵⁹. Finally, the scar tissue is completely developed, with a reduced quantity of cells and blood supply but a high tensile strength (Figure 2D) ⁶⁰.

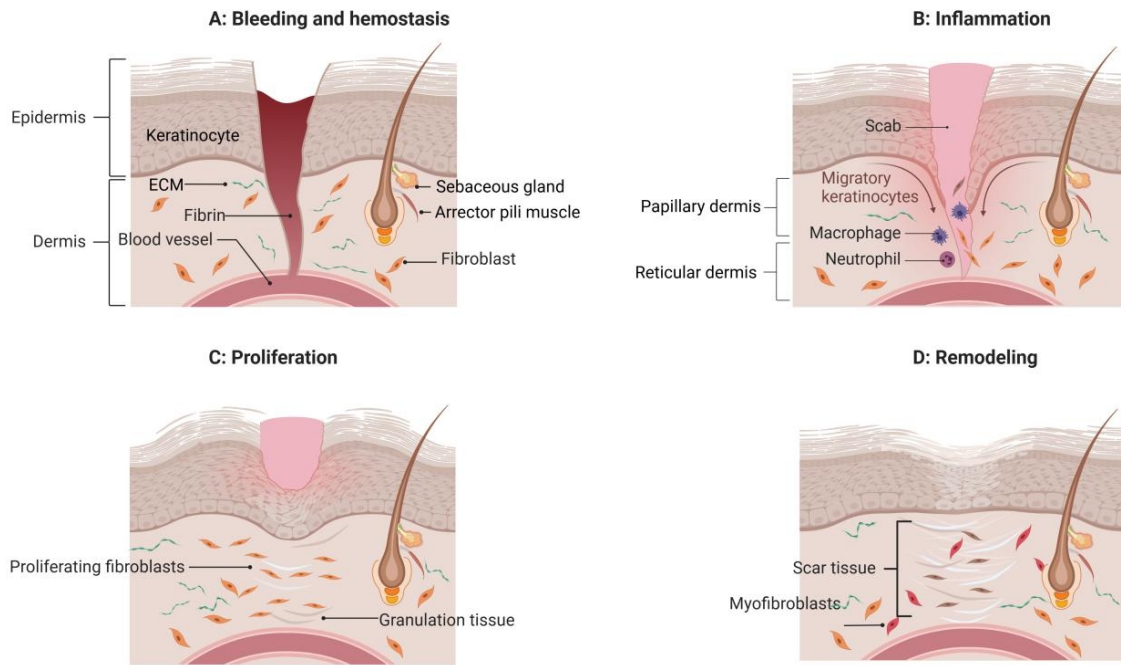


Figure 2. An illustration describing the stages of wound healing: hemostasis, inflammation, proliferation, and remodeling. Illustrations were plotted by BioRender.com (accessed on 12.09.2024).

1.3.1 Keratinocytes and their role in re-epithelialization

A crucial characteristic of complete re-epithelialization is the restoration of the integrity of the epidermal barrier by migration, proliferation, and differentiation of keratinocytes^{61, 62}. The three processes are overlapping during wound healing. Within the initial few hours after injuries, keratinocytes start migrating from the wound edges, accompanied by remarkable mitotic activities⁶³. Then cells migrate across the provisional matrix until encountering to form a new layer⁶⁴. Finally, keratinocyte differentiation is completed by losing the nucleus and forming a more flattened ovoid shape, which signifies the completion of re-epithelialization⁶⁵. The newly formed re-epithelialization protects the wound from infection.

1.3.2 Fibroblasts and their function of producing ECM

Fibroblasts are present in wound areas from the late inflammatory phase until the completion of re-epithelialization⁶⁶. In the inflammatory phase, injuries trigger inflammatory reactions and activate immune cells. Then an increased level of pro-inflammatory cytokines (interleukin-1 (IL-1), interleukin-6 (IL-6), and TNF- α , etc.) further promotes the inflammatory process and stimulates fibroblasts^{67, 68}.

Simultaneously, the recruitment, behavior, retention, and survival of immune cells can be influenced by fibroblasts as well^{69, 70}.

In the proliferation phase, fibroblasts become more important. Fibroblasts proliferate through the regulation of inflammatory mediators (fibronectin, PDGF, FGF, and TGF- β)⁷¹⁻⁷³. Then, fibroblasts promote granulation tissue formation by releasing VEGF, FGF, angiopoietin-1 (Ang-1), and thrombospondin (TSP)^{74, 75}. Meanwhile, fibroblasts infiltrate and produce various MMPs to degrade fibrin clots and induce ECM synthesis⁶⁶. Gradually, clots are replaced by ECM, which is made up of collagens, glycoproteins, proteoglycans, laminins, thrombospondins, glycosaminoglycans (GAGs), and hyaluronic acid (HA)^{34, 76, 77}. Moreover, abundant ECM is essential to the migration of keratinocytes to eventually form re-epithelialization⁷⁸. Finally, fibroblasts are induced to transition to the myofibroblast phenotype⁷⁹. At this stage, myofibroblasts actively extend their pseudopodia to attach to the surrounding ECM and increase traction force, promoting wound contraction (Figure 3)⁸⁰.

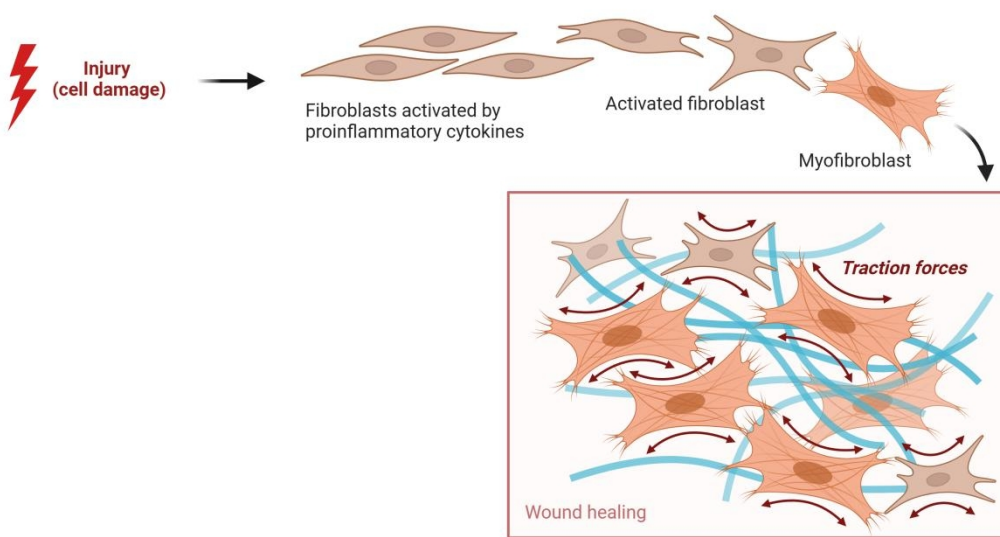


Figure 3. The differentiation of fibroblasts after injury and the mechanism of wound contraction.

1.3.3 Endothelial cells and angiogenesis

In terms of the wound healing process, angiogenesis has a profound impact on restoring blood flow, which ensures an adequate supply of oxygen and nutrients to the affected sites⁴⁷. Angiogenesis is the process by which new blood vessels are formed from existing ones⁸¹. It is highly dynamic and consists of a series of

processes, including proliferation of endothelial cells (EC), migration, tubulogenesis, remodeling, and recruitment of pericytes ⁸².

In the early step, endothelial tip cells guide the development of capillary sprout ⁸³. Tip cells exhibit elongated and motile filopodia that extend towards the source of pro-angiogenic growth factors ⁸⁴. The migration of endothelial cells occurs, and they are regulated by three ways: chemotaxis, haptotaxis, and mechanotaxis ⁸⁵. Then endothelial stalk cells proliferate, resulting in the elongation of the capillary sprout ⁸³. Through fusion of tip cells, a continuous lumen is formed that facilitates blood supplies (tubulogenesis) (Figure 4) ⁸⁴. Numerous angiogenic capillary sprouts infiltrate the fibrin clots ⁸⁶. A microvascular network forms and gradually permeates the newly formed granulation tissue. Angiogenesis that often occurs in wound beds provides neovascularization and is regulated by growth factors, such as FGF, PDGF, and VEGF ⁸⁷. Finally, in the remodeling phase, the adhesion of pericytes and smooth muscle cells (SMCs) to new capillaries and ECs has a pivotal influence on the maturity of blood vessels ^{88, 89}.

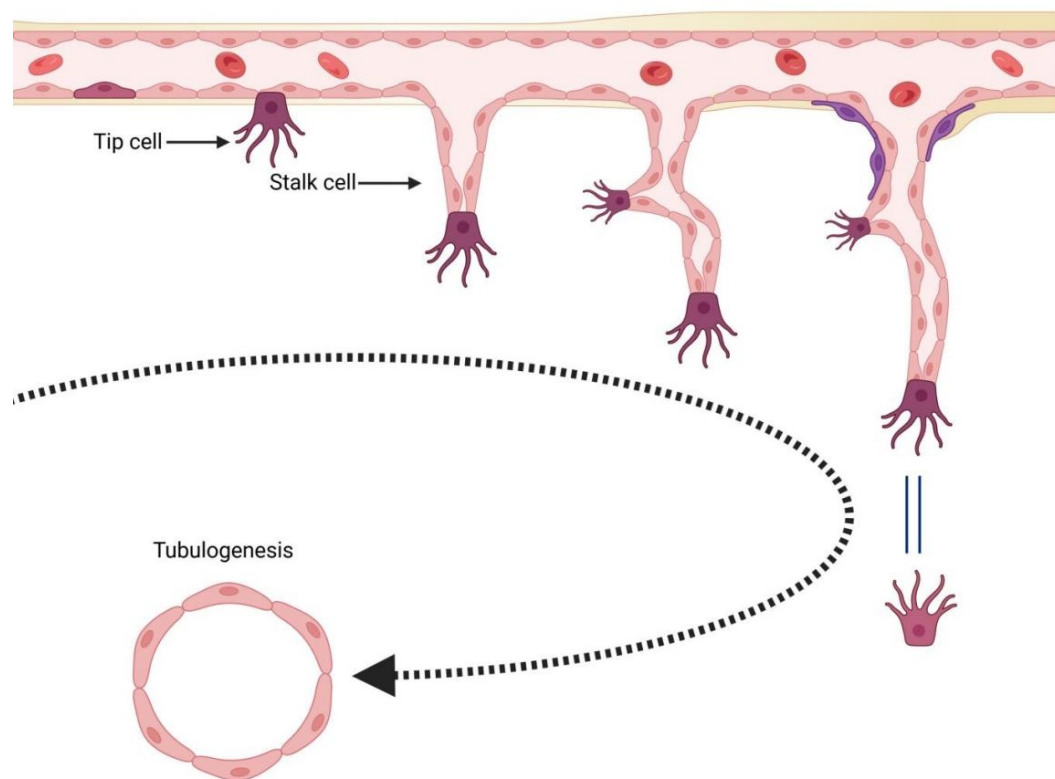


Figure 4. The process of capillary sprouting and function of endothelial cell on tubulogenesis.

1.4 Concept and mechanism of photobiomodulation.

Endre Mester first discovered and reported the photomodulatory effect in 1967. He found that laser irradiation on mice accelerated wound healing and had a biostimulation effect on hair growth ^{90, 91}. Thereafter, with an increasing number of researches on this effect and the development of technology, photobiomodulation (PBM) was conceptualized. It refers to the stimulatory biological effect on cellular activities following low-level laser therapy (LLLT) that uses photons at a non-thermal irradiance.

Visible light and near-infrared (NIR) light extensively activate photoreceptors of cytochrome c oxidase (CCO), also known as complex IV of the respiratory chain (Figure 5) ⁹². This subsequently stimulates the electron transport chains at the mitochondrial membrane. The release of nitric oxide (NO), reactive oxygen species (ROS), and adenosine triphosphate (ATP) modulates diverse cellular behaviors such as cellular metabolism, proliferation, and migration ⁹²⁻⁹⁴. CCO is proved to be the main photoreceptor for visible light and infrared radiation at wavelengths ranging from 700 to 1000 nm ⁹⁵. Depending on the wavelength, reports indicate that other photoreceptors also absorb photons after LLLT. Porphyrins absorb yellow/red light at the wavelength of 560-700 nm ⁹⁶. Flavins and flavoproteins absorb blue/green light at the wavelength of 400-550 nm ⁹⁶. Flavin mononucleotide (FMN) and flavin adenine dinucleotide (FAD) are coenzymes closely associated with flavoproteins. FMN/FAD is also an electron transducer on the respiratory chain (Figure 5). Therefore, blue light indirectly triggers an increase in ROS and causes oxidative stress via the FMN/FAD reaction. Additionally, transient receptor potential (TRP) calcium channels can mediate the PBM effect at wavelengths of 420 and 540 nm ⁹⁷. It is a ligand-gated ion channel to regulate the cytoplasm calcium gradient after activation. Upon absorption of light, the TRP channel opens, allowing a flood of calcium ions into the cytoplasm, which plays an essential role in cellular physiology. Opsins (OPNs) absorb visible light at the wavelength of 380-560 nm. As G-protein-coupled receptors, the opsin family was initially considered the primary photoreceptors in the eyes ⁹⁸. However, evidence of the photosensitivity of OPNs in skin is increasing, suggesting their potential role in wound healing after LLLT ⁹⁹. OPN2 receives photons and transduces signals that initiate calcium mobilization and melanogenesis ¹⁰⁰. Researchers recently

discovered that OPN3, typically a photoreceptor in pufferfish, stimulated the proliferation of outer root sheath keratinocytes ¹⁰¹. Researchers found that OPN4 functions on vasodilatation in mice after blue light irradiation (BLI) ¹⁰². Although increasing evidence confirms the beneficial effects of BLI on wound healing via OPNs, the underlying mechanism appears to be uncertain.

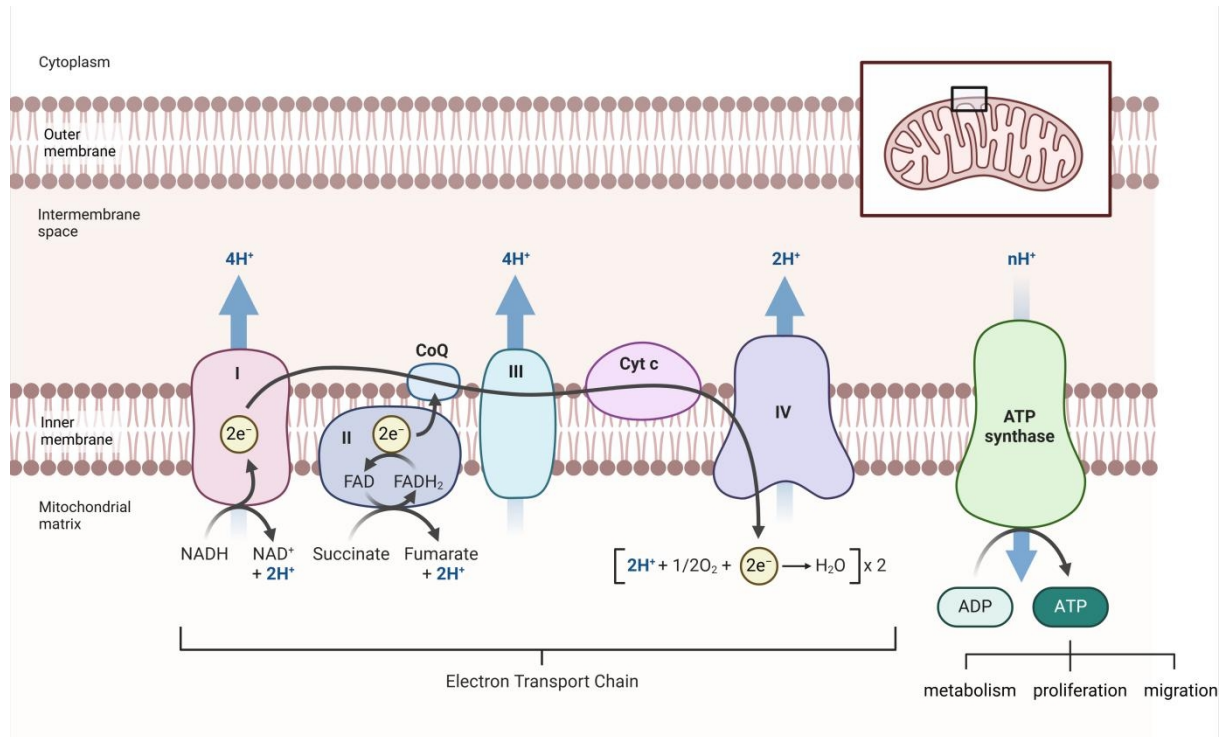


Figure 5. Components, structure of the electron transport chain, and the process of ATP synthesis.

1.5 Light-emitting diode light

Light-emitting diodes (LEDs) are semiconductor materials that convert electrical current into light via an electroluminescent process. One advantage of LED light emission is that it is non-thermal, unlike traditional light sources, which rely on electrical resistive heating and subsequent thermal radiation. Therefore, LEDs are better light sources for studies of PBM after light irradiation, avoiding thermal effects. Compared with lasers, which are monochromatic and coherent light beams, LEDs are much cheaper ¹⁰³. This advantage has led to the widespread use of various LED-based in-home devices. In contrast, the high expenditure of laser light source restricts its feasibility and primarily targets clinicians. LEDs have a broader bandwidth than lasers. Moreover, many LED devices can be easily arranged to enlarge the irradiation area. These advantages make it easier to adapt the LEDs irradiation area under different conditions.

1.6 Wound managements and clinical applications of blue light on wound healing

A variety of factors can influence the progression of wound healing, such as severity of tissue trauma, wound contamination, management strategies, and so on ³⁹. Clinicians consider complete tissue debridement and wound irrigation as primary treatments against contamination to reduce the likelihood of stagnation during wound healing ^{104, 105}. Then wound dressings can be applied. There are several categories, including traditional wound dressings, bioactive wound dressings, and tissue-engineered skin substitutes ¹⁰⁶⁻¹⁰⁸.

In terms of wound healing after light treatment, there is a widely acknowledged wavelength-dependent biological response following irradiation ¹⁰⁹. Scientists have widely reported beneficial influences on wound healing and angiogenesis following red or near-infrared irradiation ¹¹⁰⁻¹¹². However, there are still some controversies surrounding the effectiveness of BLI in wound healing. Preclinical studies revealed the stimulatory effect on wound healing after BLI on animal models ^{113, 114}. Recently, more and more clinical studies focus on the promotive effect of BLI. A clinical study demonstrated that BLI (7.2 J/cm²) at the 400-430 nm wavelength facilitates the healing process of skin ulcers caused by diabetes and arteriopathy ¹¹⁵. One study also demonstrated that BLI at a fluence of 2 J/cm² aided in the healing of skin lesions from various etiologies, including venous ulcers, post-traumatic skin lesions, and cutaneous vasculitis ¹¹⁶. Moreover, a clinical study using a maximum irradiance of 120 mW/cm² demonstrated pain relief and significant improvement in wound healing after irradiation ¹¹⁷. Lastly, BLI could accelerate the wound closure process and increase the collagen I level, as well as FGF2 and anti-inflammatory cytokines expression, with a power density varying from 55 to 129 mW/cm² ¹¹⁸.

1.7 Aim of the study

The previous studies conducted at Heidelberg University by the research group of Prof. Norbert Gretz and Prof. Micheal Keese (in collaboration with URG0) have revealed that BLI increases the migration and angiogenesis of the human umbilical vein endothelial cells (HUEVCs) with a low dose of energy (7.2 J/cm²). In contrast, with a high energy dose (28.8 J/cm²), these abilities are inhibited ¹¹⁹. In case of keratinocytes and fibroblasts, the same effects can be noted: low doses of blue light increase both proliferation and migration, leading to fast wound closure, while higher doses delay the wound healing due to decreased metabolic activity and proliferation.

These findings suggest that BLI can be used to develop potential treatment modalities for wound healing.

In this project, we aim to precisely characterize the effect of BLI on wound healing and angiogenesis using new LED-based BLI (wavelength: 450 nm) prototype from URGO (URGO RID, Chenôve, France). In the context of this project, key questions of the project are:

- What effects do different doses of BLI have on the human immortalized keratinocyte cell lines (HaCaTs), the normal human dermal fibroblasts (NHDFs), and the HUVECs?
- Is it possible to determine the optimal irradiation setting of light doses in terms of biostimulation after BLI on three cell lines?
- What biological effects can BLI have after long-term irradiation on three cell lines?
- Are there any differences in cellular responses under different irradiation schedules by comparing the sequential light treatments and the single irradiation?
- What are cellular responses when the treatment protocols are changed, including medium irradiation, medium refreshment, and altering the medium component (phenol red)?

2 MATERIAL AND METHODS

2.1 Material

2.1.1 Blue light device

The current prototype consists of two parts, an LED panel (Osram, Duris S5, GD PSLR31, Austria) and an electric control unit (Figure 6A). The irradiance (light power density, mW/cm^2) emitted by the LED is regulated by a control unit by adjusting the input current using the regulator knob. Of the two display panels in the control unit, one displays the input current for the LED panel (red rectangle), and the second screen displays the temperature measured at the center of the LED panel (yellow rectangle). The LED panel and control unit are connected via an electric strip. The LED panel consists of a 10×10 LED matrix in which each LED has an area of 1.5 cm^2 , and the whole area is $17.1 \times 16 \text{ cm}^2$. Below the LED panel, an aluminum heat sink passively evacuates the heat generated by the LED (Figure 6B). A reflective box made of Dibond mirrors is placed above the LED panel. The mirrors redirect and centralize peripheral light to provide homogeneity at the irradiation area. The current from the driver is conveyed through the electrical connection strip to the light source (LEDs) on the panel. The LED panel generates visible light at the wavelength of $450 \pm 5 \text{ nm}$ in a continuous irradiation mode (Figure 7). This prototype was designed and produced by URG0. The emission spectrum of the prototype was measured and calibrated by URG0 as well.

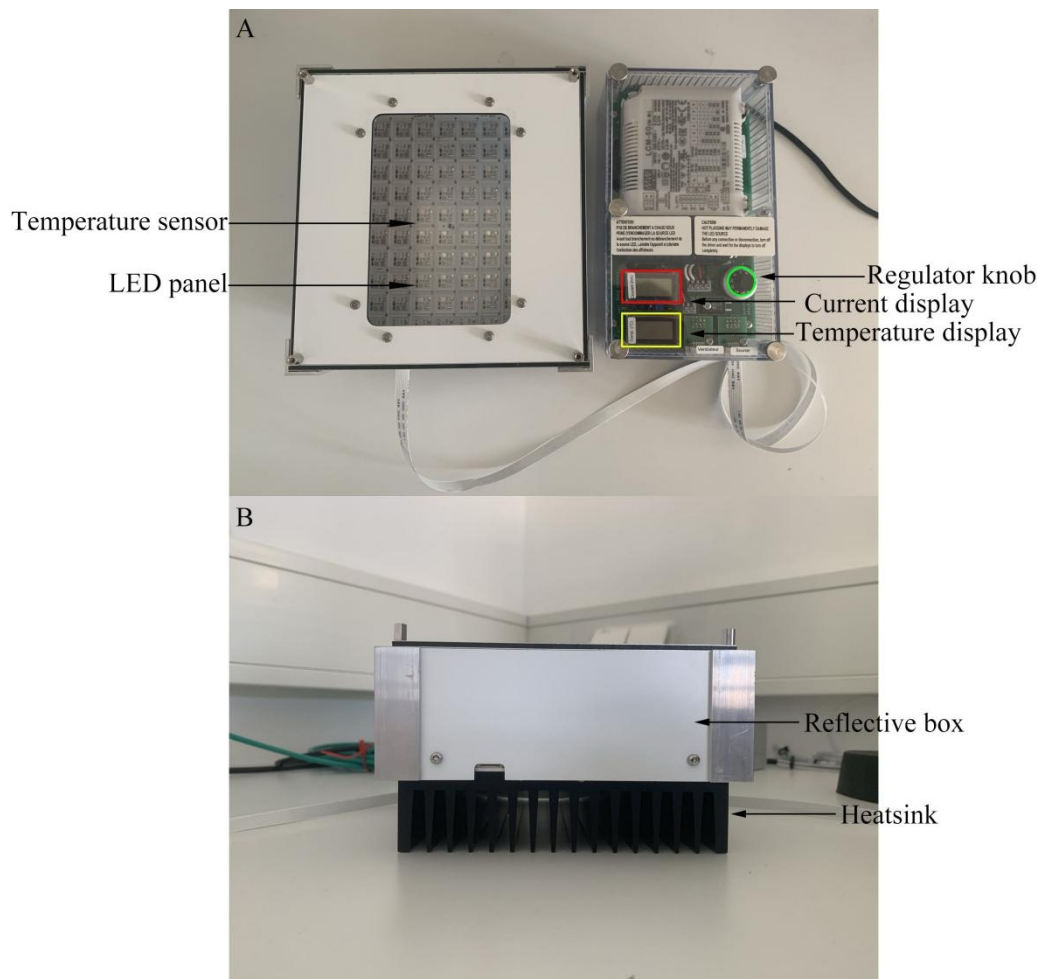


Figure 6. The components of the blue light prototype from URGO. A: Top view. B: Front view.

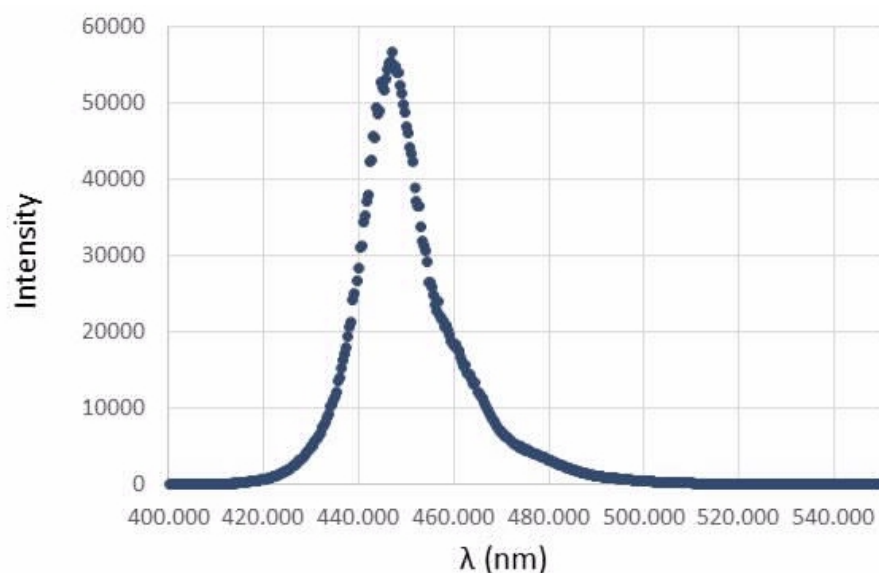


Figure 7. An important irradiation parameter of the prototype: The spectral emission at 450 ± 5 nm for the LED source.

2.1.2 Device for temperature measurement

The temperature was measured by a thermocouple sensor connected to a Pico Technology USB TC-08 data logger (Pico Technology, Cambridgeshire, UK) (Figure 8A). This experimental design allows for accurate and real-time temperature measurement. Multiple sensors collected temperature data from different areas simultaneously and then displayed via corresponding channels (Figure 8B). A USB cable connection to a computer enabled data visualization to be completed within seconds. The corresponding software (Picolog 6.1.15) allows for the simple and direct visualization of temperature fluctuations. Both real-time and historical temperature data can be obtained by adjusting the range of the x-axis.

2.1.3 Photodiode-based device

URGO provided a new photodiode (REUR2021-085SAF¹) that probes the light intensity. As described in Figure 9, this device is composed of a photodiode and electronic display interface, which are connected by a coaxial cable (Figure 9A). After the detection by the silicon sensor (Figure 9B), the displayed current can be read from the LCD screen (Figure 9C). By equating (equation provided by URGO, data not shown) the displayed current with irradiance measured by a spectrophotometer (AVANTES AvaSpec-3648, Apeldoorn, The Netherlands), this photodiode can indicate light intensity precisely and directly. Additionally, the photodiode was originally designed to characterize small-diameter light spots, especially the light at the bottom of 96-well cell culture plates.

To further facilitate the measurement of light intensity on cells, a 96-well metal plate (Dibond, aluminum composite material) with a polyurethane transparent film was designed to imitate the transparent plastic layer at the bottom of the 96-well black plate (Figures 9D and E).

¹ provided by URGO

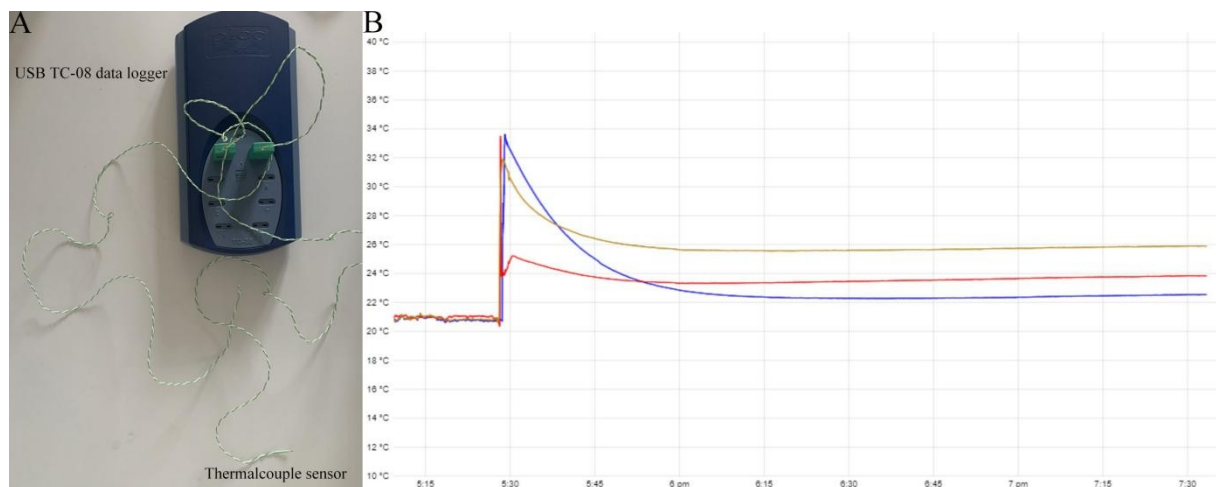


Figure 8. A: The components of the device for temperature measurement. B: The representative plots to show the change of temperature during irradiation.

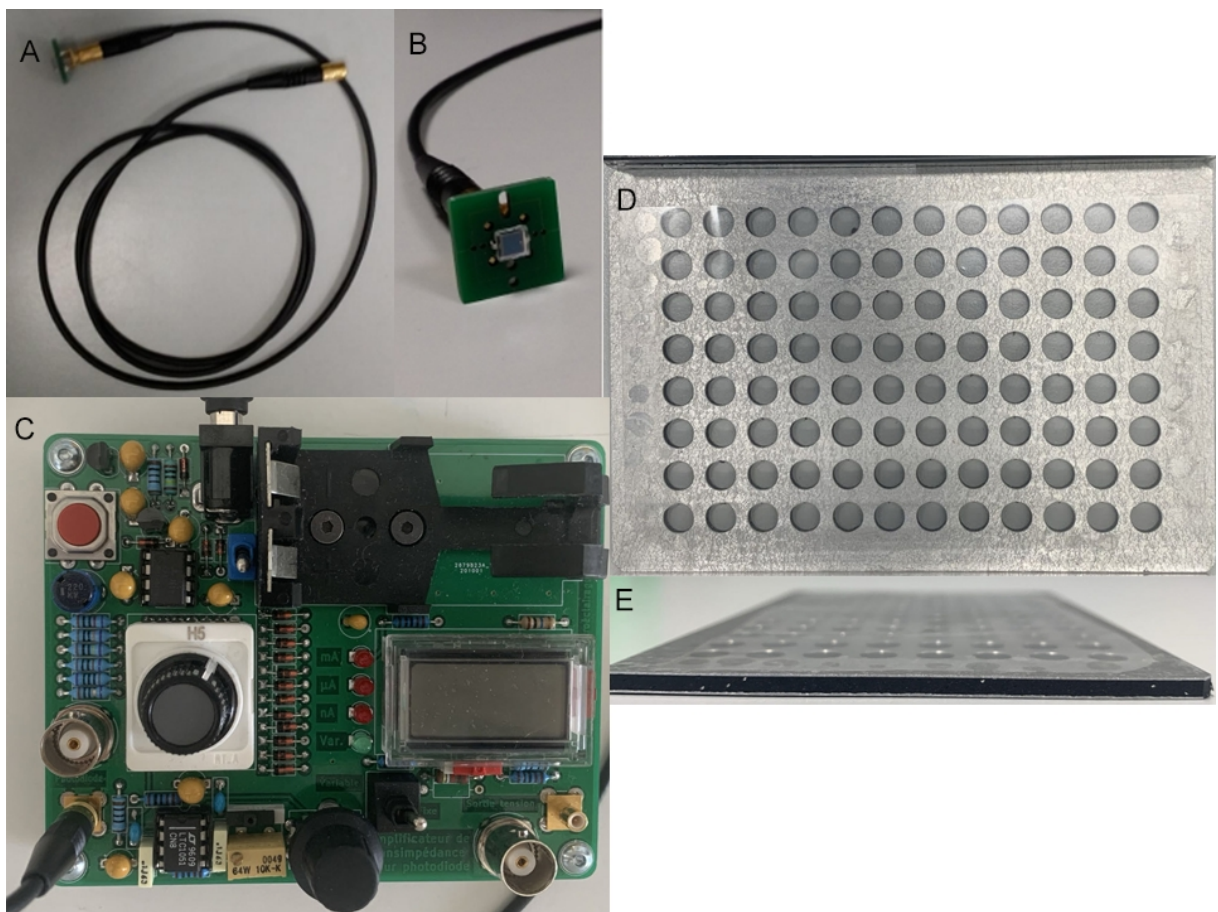


Figure 9. The components of photodiode-based device (A, B and C). A: The cable and sensor. B: Photodiode. C: The LCD screen and the control unit. D and E: Bottom view and side view of a 96-well metal plate.

2.1.4 Comsumables

Name	Supplier
96-well Black Polystyrene Microplate	Corning
Cell culture flask, different size	Greiner Bio-One

Cell culture plate, 6-well, transparent	Sarstedt
Cell culture plate, 12-well, transparent	Sarstedt
Falcon tube (15 and 50 mL)	Greiner Bio-One
Cytotube vials	Thermo Fisher Scientific
Pipette tips with filters	Eppendorf AG
0.22 µM filter	Carl Roth GmbH
Eppendorf tubes (0.5, 1 and 2 mL)	Eppendorf
5 mL round bottom tubes	neoLab Migge Laborbedarf-Vertriebs GmbH

2.1.5 Chemicals and reagents

Name	Supplier
Colorimetric Cell Viability Kit III (XTT)	PromoKine
Colorimetric ELISA-BrdU kit	Roche Diagnostics GmbH
CellTiter-Glo® Luminescent Cell Viability Kit	Promega Corporation
Staurosporine	Sigma-Aldrich
TrypLE selected enzymes	Thermo Fisher Scientific
FITC Annexin V Apoptosis Detection Kit I	BD Pharmingen
RNeasy mini kit	Qiagen
Endothelial cell growth medium	Provitro
DMEM GlutaMAX™	Thermo Fisher Scientific
Sodium pyruvate	Sigma-Aldrich Chemie GmbH
Penicillin/streptomycin	Sigma-Aldrich Chemie GmbH
SupplementMix - Fibroblast Growth Medium 3	PromoCell
FBS, Qualified, HI	Gibco
DPBS	Thermo Fisher Scientific
Collagenase IV	Sigma-Aldrich
Gelatin from bovine skin	Sigma-Aldrich
IDT for Illumina RNA index anchors	Illumina
DNA/RNA UD index set A	Illumina
RNA prep ligation	Illumina
Poly(A) capture	Illumina
NextSeq 500/550 High Output Kit v2.5 (75 Cycles)	Illumina

2.1.6 Instruments

Name	Supplier
Cell incubator, Galaxy 170 S	Eppendorf
Centrifuge, 5920R	Eppendorf
HERA freeze	Thermo Fisher Scientific
Microscope Zeiss Standard 25	Carl Zeiss Microscopy GmbH
Safe 2020 Class II Biological Safety Cabinet	Thermo Fisher Scientific
Power meter 843-R-USB	Newport Corporation
NanoQuant plate	Tecan Austria GmbH
Fluorescence microscope, Zeiss Axio Spark® Multimode Microplate reader	Zeiss
Water bath, TSGP15D	Tecan
	Thermo Fischer Scientific

Name	Supplier
Agilent 2100 Bioanalyzer	Agilent Technologies
NextSeq550	Illumina
USB TC-08 Thermocouple Data Logger	Pico Technology
Blue light prototype	URGO
Photodiode-based device (REUR2021-085SAF)	URGO

2.1.7 Software

Name	Supplier/Application
ImageJ	National Institution of Health, USA
GraphPad Prism 8	Graphpad Prism Software
Rstudio version 1.1.463	Posit PBC
R version 3.6.3	R core team
SparkControl	Tecan
SPSS Statistics	IBM
ZEN 2 (blue edition) Axio Scan software	Carl Zeiss
PicoLog 6 data logging software	Pico Technology
JMP Genomics version 7.1	SAS Institute Inc

2.2 Methods

2.2.1 Blue light irradiation

Our LED-based BLI prototype from URGO demonstrated a correlation between irradiance and required current, after measurement and calibration. We referred to the corresponding parameters and applied these to the in vitro experiments on the cell lines. During the following experiments of irradiation, irradiances of 7, 10, 23, and 40 mW/cm² were adapted and used. 96-well black plates (Corning Incorporated, Lowell, MA, USA) were used in order to avoid light scatter. Meanwhile, wells wrapped with aluminum foil were considered as control group to avoid direct light irradiation (Figure 10), while wells on the symmetrically opposite side were regarded as treatment groups.

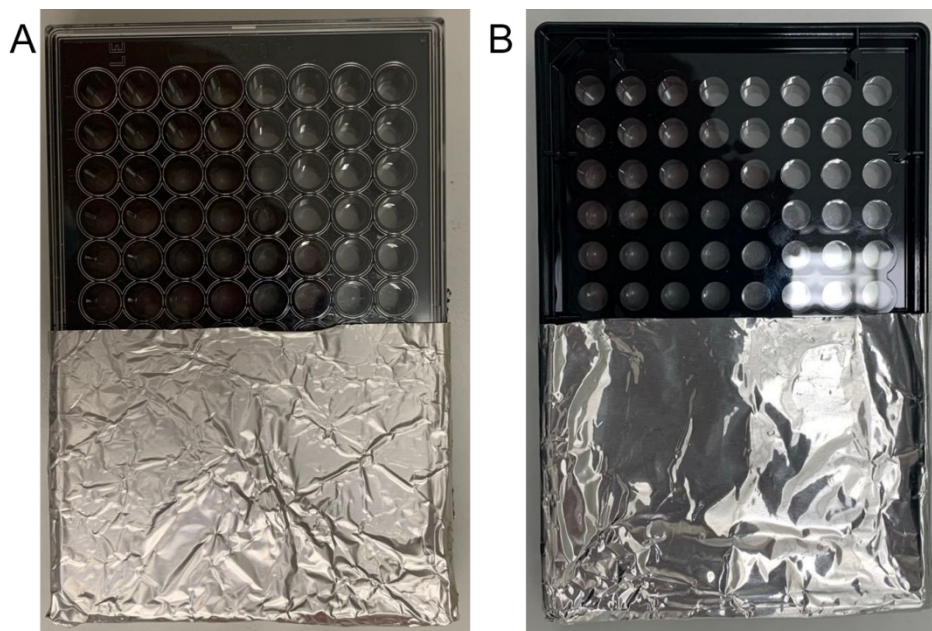


Figure 10. Schematic diagram of experimental setting (a 96-well plate). A:Top view. B: Bottom view.

2.2.1.1 Sequential light treatments.

The calculated irradiation parameters from URGO provided the basis for designing a sequential light treatment with two doses of irradiation. With a predefined seeding density of 6000/well, cell lines were seeded on a 96-well black plate first. Then, high doses of BLI with an irradiance of 23 mW/cm^2 for either 2 or 5 h were added to cells 24 h after the completion of the seeding process. The following table (Table 1) describes details of treatment protocols on cell lines. All cells in groups B and A received sequential light treatments with irradiances of 23 and 10 mW/cm^2 . Cells from groups C, D, and E acted as controls for comparison with different incubation times. Cells in groups B and D were harvested on the same day (day 4), and then XTT assays were performed. Cells in groups A and E were simultaneously harvested, and cell viability assays by XTT were measured on day 5.

Groups	Day 1	Day 2	Day 3	Day 4	Day 5
C			XTT		
D			-	XTT	
B	Cell seeding*	23 mW/cm ² irradiation for 2 h or 5 h	4.5 J/cm ² BLI	XTT	
E			-	-	XTT
A			-	4.5 J/cm ² BLI	XTT

*: The seeding density of each cell types was 6000/well.

Table 1. The schedule of sequential light treatments with irradiance of 10 and 23 mW/cm^2

2.2.2 Cell lines and cell culture

2.2.2.1 Immortalized human keratinocytes.

HaCaT, an immortal human keratinocyte cell line (spontaneously immortalized aneuploid human keratinocyte cell line), was purchased from CLS Cell Lines Service GmbH (Eppelheim, Germany). They were cultured in Dulbecco's modified Eagle medium with high glucose (DMEM GlutaMAX™, [+] 4.5 g/L Glucose, [-] Pyruvate, Thermo Fisher Scientific, Grand Island, New York, NY, USA) supplemented with 10% fetal bovine serum (FBS, Thermo Fisher Scientific, Grand Island, New York, NY, USA), 1 mM sodium pyruvate (Sigma-Aldrich Chemie GmbH, Taufkirchen, Germany), 10,000 units penicillin, and 10 mg streptomycin per mL (pen/strep, Sigma-Aldrich Chemie GmbH, Taufkirchen, Germany). HaCaTs were cultured at 37°C in a humidified atmosphere with 5% CO₂. Once the confluence observed under a microscope reached 70–80%, the process of subcultivation initiated with the removal of old culture medium from the flask. Then enough Dulbecco's Phosphate-Buffered Saline (DPBS, Thermo Fischer Scientific, Waltham, MA, USA) without Ca²⁺ and Mg²⁺ was added to cell culture flasks depending on surface area: 3-5 mL to the T25 flask and 5-10 mL to the T75 flask. After fully rinsing the adherent HaCaTs, DPBS was then discarded and replaced by TrypLE Express Solution (Thermo Fisher Scientific, Waltham, MA, USA) for cell detachment. The process of cell detachment was kept in an incubator with the standard culture conditions at 37°C and 5% CO₂ for 1–5 min. Cells were passaged at 1:4 or 1:3 for use every two to three days, depending on the confluence. The cells were used up to passage 50. The representative morphologies of HaCaTs are shown in Figure 11 and the scale bar is 200 µm.

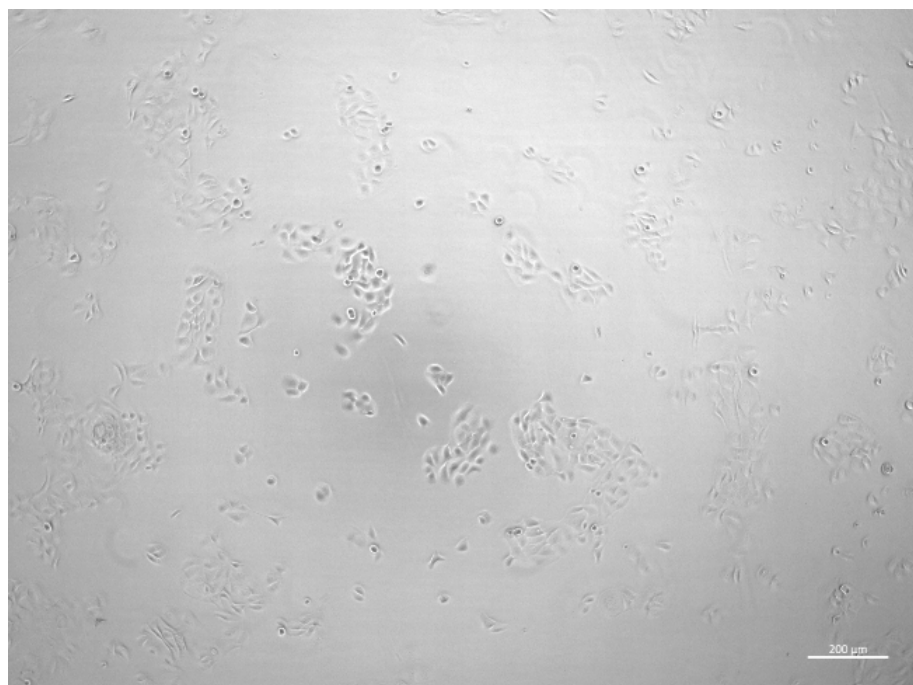


Figure 11. The morphologies of HaCaTs observed under a microscope with a scale bar of 200 μm . The image was captured by a Zeiss Axio fluorescence microscope (Carl Zeiss Microscopy, Göttingen, Germany) and showed the cell cluster distribution.

2.2.2.2 Normal human dermal fibroblasts.

NHDFs isolated from pooled dermis of juvenile foreskin or adult skin were purchased from PromoCell GmbH (Heidelberg, Germany). They were cultivated in Dulbecco's Modified Eagle Medium (DMEM, high glucose, GlutaMAXTM, Thermo Fisher Scientific, Grand Island, New York, NY, USA), supplemented with 10,000 units of penicillin and 10 mg of streptomycin per mL, SupplementMix-Fibroblast Growth Medium 3 from PromoCell (Heidelberg, Germany), and 1 mM sodium pyruvate. We used the cells with a maximum of 15 population doublings during the cell culture process to ensure logarithmic growth and prevent further senescence. According to the instruction of PromoCell, NHDFs were re-seeded once the subconfluence reached 70–80% in order to ensure the plating density varied from 3,500 to 7,000 cells/cm². For cell detachment, the TrypLE Express was warmed to 37°C. This pre-warmed solution was added based on the volume of the flask during cell culture: 1 mL in a T25 flask, 3 mL in a T75 flask. After gently rocking the flask to ensure the solution completely coats cells, incubation proceeded at 37°C for approximately 5 min until the cell detachments were confirmed by microscope. After cell quantification was completed with a cell counting chamber, NHDFs were seeded in a new flask or a multiwell plate for further experiments at a proper seeding density. Like keratinocytes, NHDFs culture were also maintained at the standard culture condition at 37°C under 5% CO₂.

NHDFs were passaged with the passaging ratio of 1:4 or 1:3 for use every three days. Figure 12 shows the morphologies of NHDFs with a scale bar of 200 μ m.

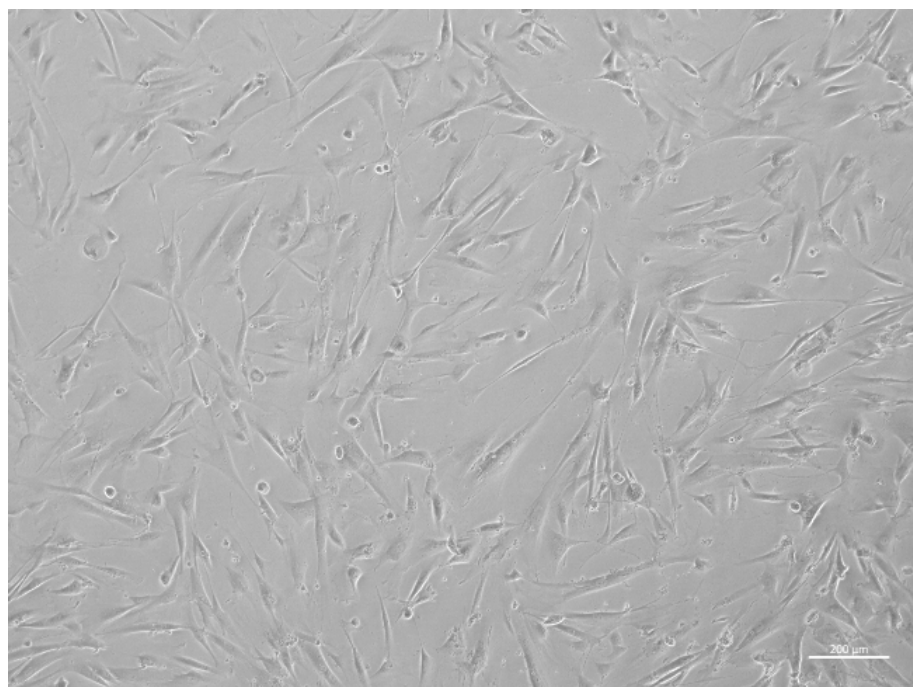


Figure 12. The morphologies of NHDFs with the scale bar (200 μ m). Most cells had a spindle or stellate shape. The image was captured in phase contrast with 5 \times magnification.

2.2.2.3 Human umbilical venous endothelial cells.

HUVECs were isolated from human umbilical cords using the methods described by Jaffe et al.¹²⁰. The fresh umbilical cords were obtained from donors from the Gynecology and Obstetrics Department of Universitätsklinik Mannheim, and HUVEC isolation was approved by the local ethics committee (Medizinische Ethik-Kommission II, Medizinische Fakultät Mannheim, 2015-581N-MA, Mannheim, Germany). The process of endothelial cell isolation was initiated immediately after a fresh umbilical cord was obtained. Briefly, after digesting with 1% collagenase IV, the vein was flushed with sterile and fresh endothelial growth medium (Provitro, Berlin, Germany) supplemented with 5% FBS (Gibco, Brasilia, Brazil), endothelial cell growth supplement mix (Provitro, Berlin, Germany), 10,000 units of penicillin, and 10 mg of streptomycin per mL. After the stop of the digesting process, the detached HUVECs were collected in a 15 mL tube. These isolated endothelial cells were cultured in a T25 flask pre-coated with 1% gelatin at 37°C under 5% CO₂. 24 h incubation after HUVEC isolation, medium refreshment was performed, and remaining cells were cultured at the abovementioned standard culture condition as same as the other two cell lines. The subcultivation of HUVECs was at a passaging

ratio of 1:3. HUVECs from three donors were pooled and used in experiments between passages two to five.

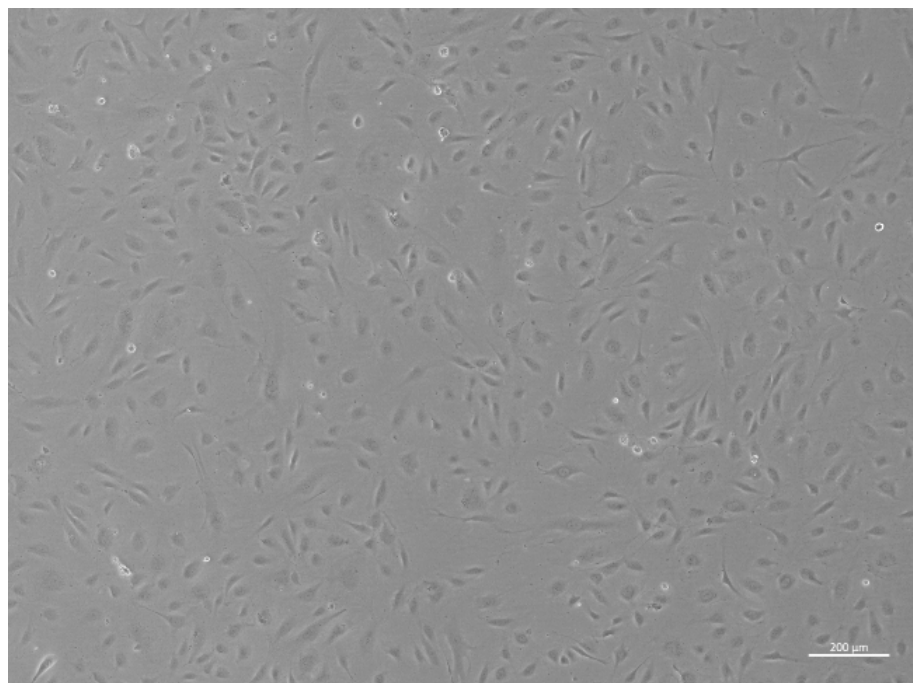


Figure 13. The morphologies of HUVECs seeded at a T25 flask in passage 3. The scale bar was 200 μ m.

2.2.2.4 Treatment protocols on cell culture prior to BLI

All adherent cell lines were replenished with the fresh medium 24 h after cells were seeded on plates. Subsequently, cells were continuously incubated at 37°C with 5% CO₂ for another 30 min prior to BLI. To be specific, the corresponding medium was renewed only before light exposure. During the further irradiation, fresh medium and cells were simultaneously exposed to light doses.

2.2.3 Temperature measurements

Blue light generated heat during the irradiation process, potentially causing irreversible changes in cell lines and leading to overheating over time. Initially, we conducted temperature measurements to determine a range of irradiances for subsequent experiments on three cell types, making sure the temperature stayed stable and safe for cell culture after long exposure to BLI. To understand the thermal effects of BLI, we measured the change of temperature in the wells of a black 96-well cell culture plate with cell culture medium (without cells). To this end, 100 μ L of the cell culture medium was added to the wells of a black 96-well cell culture plate, and this plate was placed in the incubator (37°C and 5% CO₂) for 30 minutes. Next, we

conducted a pre-run of the temperature measurements set up for 15 minutes at room temperature (RT) without light irradiation. Those data of RT acted as baselines for reference. Afterward, through openings constructed at the side of the cell culture plate shown in Figure 14, three thermocouples were placed at three different locations to record temperature variation:

- Thermocouple 1 was submerged into the medium,
- Thermocouple 2 was in the well above the medium, and
- Thermocouple 3 was placed between two wells without direct exposure to BLI.

Finally, the thermocouples were connected to a Pico Technology USB TC-08 data logger (Pico Technology, Cambridgeshire, UK). The plate was then irradiated with 10, 23, and 40 mW/cm² for 120 minutes each. All three temperature sensors recorded temperature, and the data visualization was proceeded by the corresponding software: Piclog 6. 1. 15 simultaneously.

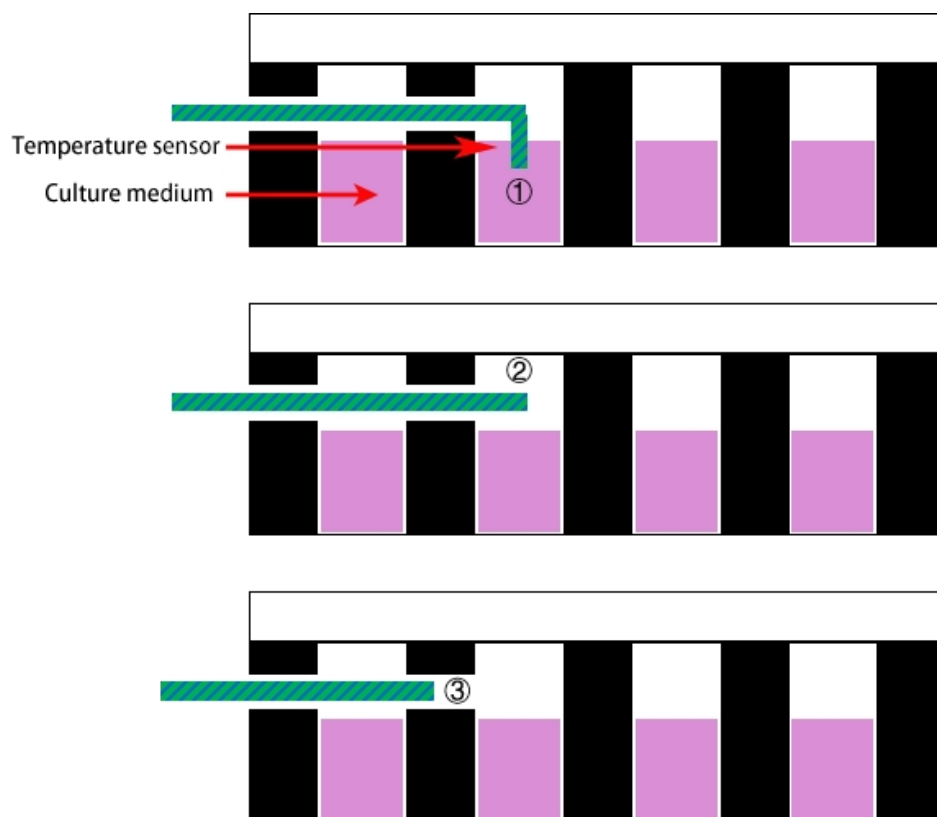


Figure 14. Experimental setup for temperature measurement in a black 96-well cell culture plate using thermocouples. Thermocouples were placed in three positions: (1) In the medium; (2) In the well above the medium, and (3) between two wells without the direct exposure to blue light. The data was captured by the Pico Technology USB TC-08 data logger.

2.2.4 The distribution of light intensity

Prior to conducting formal in vitro experiments on cell lines, it was necessary to have a comprehensive understanding of the light intensity distribution to make informed decisions about the irradiation areas, given the impact of irradiation treatment on different cell types. The light distribution was measured by a silicon photodiode (REUR2021-085SAF) mentioned above. Since the photodiode sensor cannot reach the bottom surface of the black 96-well cell culture plate, a metal sheet resembling a 96-well cell culture plate with a shorter well height was used to characterize the light distribution. Thereby, this plate is referred to as a custom-made black metal 96-well plate. The experimental setup for the measurement of light distribution is shown in Figure 15. The custom-made black metal 96-well plate was placed in the plate holder to mimic the cell culture environment in which cells are seeded at the bottom of a 96-well black cell culture plate. This custom-made black metal 96-well plate allows the sensor to directly touch the bottom of the plate. All measurements were performed with the irradiance of 23 mW/cm².

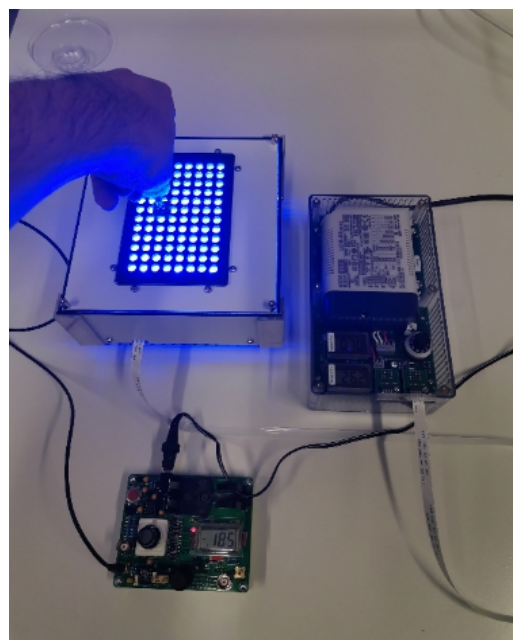


Figure 15. Measurement of light distribution by the photodiode. The silicon sensor detected light intensity and converted it into current, displaying the value of current on the LCD screen.

2.2.5 Cell viability assay.

Cell viability was assessed using the Colorimetric Cell Viability Kit III (XTT) from PromoKine (PromoCell GmbH, Heidelberg, Germany). Specifically, a spectrophotometer can measure the absorbance based on the property of activated mitochondrial enzymes converting tetrazolium salts into colored formazan

compounds. On the first day, 8×10^3 cells/well were seeded in a 96-well black plate. 24 h after cell planting, irradiation was initiated with the predefined exposure time from 2.5 to 120 min and irradiances (7, 10, and 23 mW/cm²) following medium refreshment and 30 min of incubation. After an additional 24 h of incubation under standard cell culture condition in the incubator, both the XTT reagent solution and the activation reagent PMS (N-methyl dibenzopyrazine methyl sulfate) were thawed in a 37°C water bath prior to use. We added the activation solution to XTT reagents with a ratio of 1:200 to derive the activated XTT solution. Then 25 μ L of reaction solution was added to each well. Subsequently, the plate was gently shaken to ensure even distribution of the dye before an incubation time of 1 h. A spectrophotometer finally measured the absorbance at wavelengths of 450 and 690 nm.

2.2.6 Cell proliferation assay.

The colorimetric ELISA-BrdU kit (Roche Diagnostics GmbH, Mannheim, Germany) was used to quantify the newly synthesized cells and the level of cell proliferation after irradiation. 10 μ L/well BrdU labeling solution was added to a 96-well black plate 1 h after the completion of predefined irradiation, which was scheduled and performed 24 h after the cell seeding. After another incubation time of 24 h, cell proliferation assays were performed through a series of processes of cell fixation, adding anti-BrdU antibody, sample washing, and chromogenic reaction. Cell fixation was completed 30 min after adding 200 μ L FixDenat into each well to induce DNA denaturation. Subsequently, the reaction took place after the addition of Anti-BrdU-POD antibodies, lasting for 90 min. Then the free and unbound antibodies were removed through washing (200 μ L/well washing solution) at least three times. In the last step, 100 μ L of substrate solution was added to each well to induce reactions for another 5 min. The reaction was stopped with a thorough mixture of 25 μ L of 1 M H₂SO₄. Within the next 5 min, a spectrophotometric absorption measurement was taken at 450 nm (with 690 nm as the reference wavelength).

2.2.7 ATP quantification.

The CellTiter-Glo® Luminescent Cell Viability Kit (Promega Corporation, Madison, WI, USA) was used on ATP quantification. The luciferase reaction catalyzes the mono-oxygenation of luciferin in the presence of Mg²⁺, ATP, and molecular oxygen, leading to cell lysis and producing a luminescent signal proportional to the amount of ATP. According to the protocol from the manufacturer, both the lyophilized CellTiter-Glo®

Substrate and CellTiter-Glo® Buffer should be equilibrated at RT prior to formal use. After that, the appropriate buffer was transferred into the substrate bottle for reconstitution, creating a mixture. Before adding to a well, those components were gently mixed to obtain a homogeneous solution. 24 h after irradiation, the same volume (100 μ L/well) of reagent as cell culture medium was added in the 96-well black plate. Then the mixed solution was shaken for 2 min to induce cell lysis. The luminescent signal stabilized after another 10 min of incubation time at RT, making it ready for luminescence recording. After setting the integration time at 1000 ms, the raw data was recorded by the Spark® microplate reader. A control well containing only medium without cells was prepared as well to record background luminescence.

2.2.8 Migration assay.

A seeding density of 8×10^4 /well was selected for three cell types on a 12-well plate. Cells grew to confluence within the next 24 to 48 h. A gap was made by a 10 μ L sterile pipette tip in the confluent monolayer. A specific scratch device (Figure 16A) for a 12-well plate was utilized to generate four artificial wounds in the middle of each well, simultaneously. In order to simulate the process of wound closure influence by light exposure, gaps were created prior to the irradiation. After wounds were created, the detached cells were washed twice with DPBS, and fresh cell culture medium containing 1% FBS was supplied to support the basic survival of cells. Images were captured by an inverted microscope (Carl Zeiss Microscopy, Göttingen, Germany) (Figure 16B) at predefined time intervals (0, 3, 6, 12, 24 h) until the wound closure. The analysis was completed by ImageJ software (version 1.53e, NIH Image, NIH, Bethesda, MD, USA). Figure 17 shows the method of calculating percentages of wound closure by comparing wound areas at different time points.

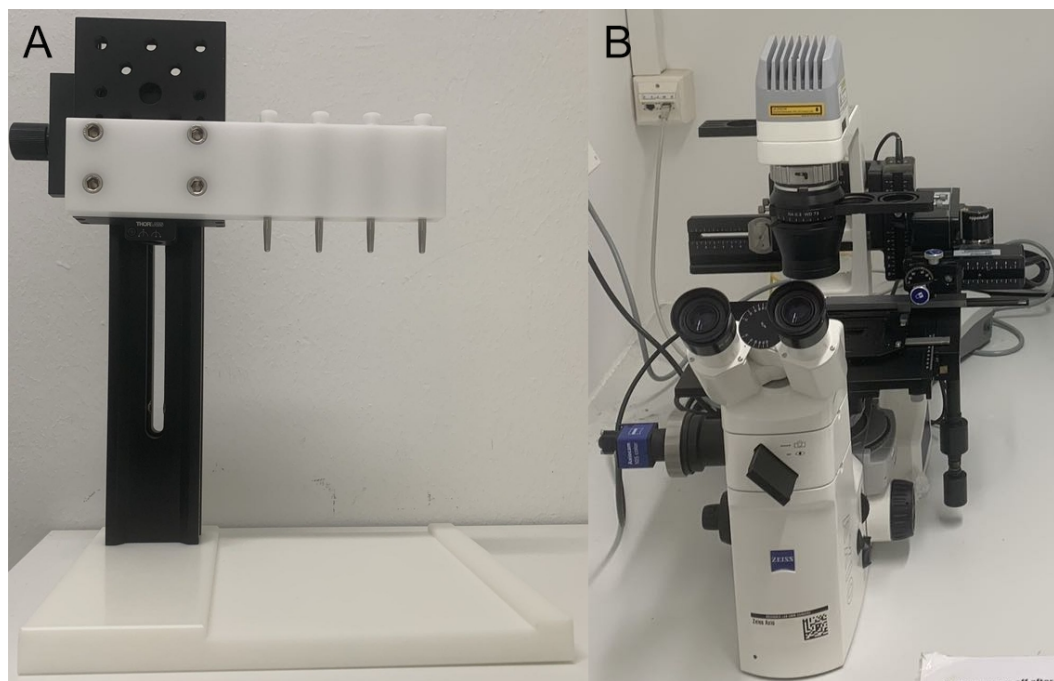
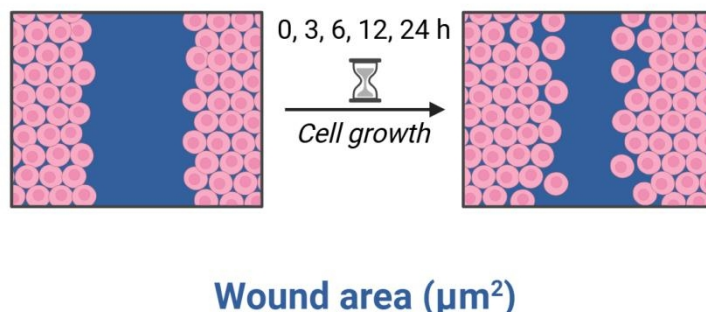


Figure 16. Scratch device specific for the 12-well plate (A), and the inverted fluorescence microscope (Zeiss Axio, Carl Zeiss Microscopy) (B).



Wound area (μm^2)

$$\text{Wound closure (\%)} = (\text{original wound area} - \text{area at each time point}) / \text{original wound area}$$

Figure 17. The observation time point in the migration assay and the equation of wound closure.

2.2.9 Apoptosis assay.

On the next step, FITC Annexin V/PI staining was used to identify early apoptosis (PI negative, FITC Annexin V positive) and late apoptosis/cell death (PI/FITC Annexin V positive) because early apoptotic cells with membrane integrity can exclude propidium iodide (PI), whereas cells in late apoptosis or dead show both Annexin V and PI staining as positive. The flow cytometry required large quantities of cells for

sorting, calculation, and subsequent analysis. Therefore, 6-well plates were utilized for cell planting. A density of 1.6×10^5 cells/well was selected to ensure sufficient cell harvesting 24 h after the seeding by preliminary experiments. Four groups were designed accordingly. Cells in the positive control group were treated with 1 μM staurosporine (Sigma-Aldrich, Darmstadt, Germany) and incubated for 24 h prior to cell harvesting. Cells in the light treatment groups were arranged to be exposed to different doses of BLI (4.5 and 18 J/cm^2). Cells in the control group received no intervention and were harvested simultaneously. According to the manual instruction, after trypsinization, all viable, apoptotic, and dead cells with the supernatants were completely harvested and centrifuged. After titration, a volume of 0.5 μL Annexin V and 2.5 μL PI (FITC Annexin V Apoptosis Detection Kit I, BD PharmingenTM, Franklin Lake, NJ, USA) was determined for cell staining. Simultaneously, unstained cells with the same treatments were also harvested for better comparisons. Then, these vortexed cells were placed and incubated in the darkness at RT for 15 min. Finally, after adding 100 μL of 1 \times binding buffer, a maximum of 10,000 events/tube were recorded by BD FACSCanto II (BD Bioscience, Heidelberg, Germany), and the acquired raw data were analyzed by FlowJo v10 (FlowJo LLC, Ashland, USA).

2.2.10 Cell viability assays after medium irradiation and refreshment

The following steps were designed to explore if specific conditions, such as medium irradiation or medium refreshment, could potentially impact the level of cell viability. Three cell lines were separately seeded in 96-well black plates. Cells in group 1 (indicated by a red rectangle) were controls without any interventions. Figure 18 illustrates cells in group 2 (blue rectangle) received the transferred medium after irradiation in group 3. After a complete medium removal in group 3 (green rectangle) and twice washing with DPBS, the process of medium refreshment was completed after adding 100 μL /well of fresh medium. As a positive control group (purple rectangle), only the process of irradiation with an irradiance of 10 mW/cm^2 was conducted, without medium change or medium refreshment. Notably, all culture medium in this experiment was phenol red-free.

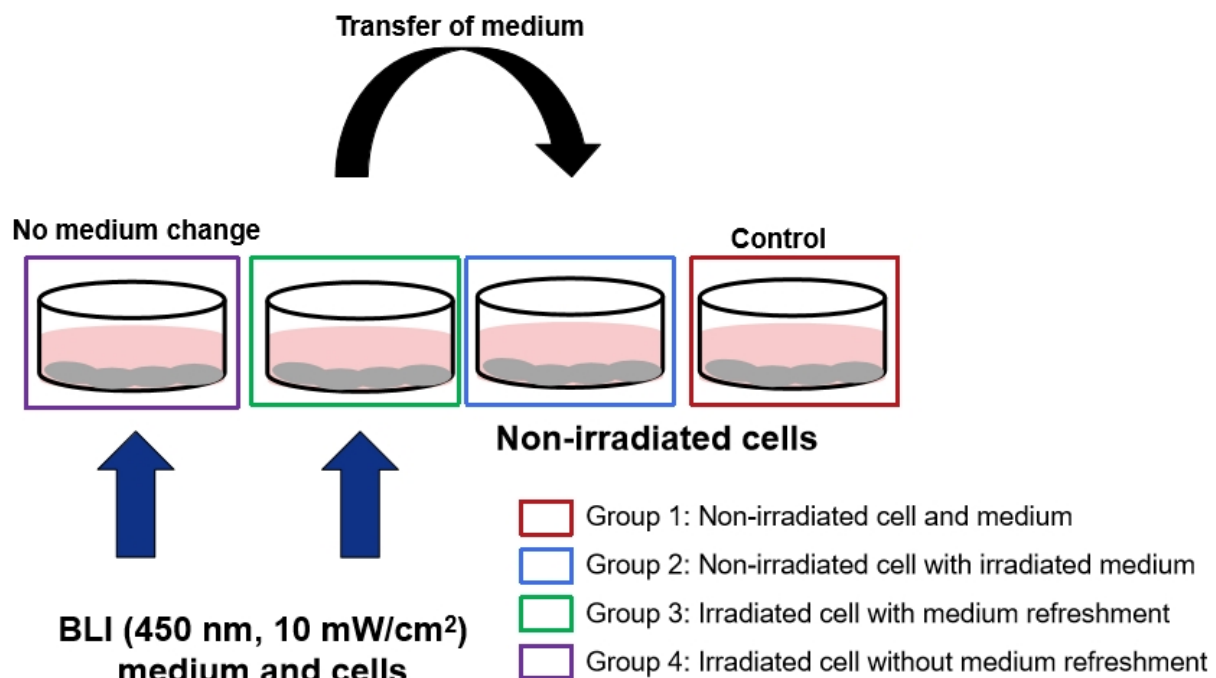


Figure 18. The illustration of steps on medium irradiation and medium refreshment.

2.2.11 Gene expression analysis

2.2.11.1 RNA isolation

To ensure a sufficient volume and concentration of total RNA samples submitted for further RNA sequencing. Similar to the process of apoptosis assays, 1.6×10^5 cells were seeded in a well of a 6-well plate and cells kept growing in a monolayer until harvesting. 24 h after the cell seeding, BLI treatments of different doses (4.5 and 18 J/cm²) were added to those adherent cells in treatment groups. Cells without any visual light exposure belonged to control groups. The total RNA was isolated by the RNeasy mini kit (Qiagen, Hilden, Germany) according to the manufacturer's instruction. Briefly, after washing twice with DPBS and completely removing the cell culture medium, cells were disrupted by adding 350 μ L Buffer RLT. Then, the same volume of 70% ethanol was added to those lysates and mixed thoroughly by pipetting. All samples were transferred to a spin column placed in a 2 mL collection tube and centrifuged for 1 min at 10000 \times g. After the flow-through was discarded, 700 μ L of Buffer RW1 was then added and centrifuged for another 1 min at 10000 \times g. After completely emptying the collection tube, 500 μ L Buffer RPE were added to the spin column and samples were centrifuged at 10000 \times g two times. Finally, after adding 25 μ L of RNA-free water and centrifugation again, we eluted enough total RNA for

subsequent assays of RNA quantification, quality control, library preparation, and RNA sequencing.

2.2.11.2 RNA quantification and quality control

NanoQuant plate and Spark® Multimode Microplate reader (Tecan, Männedorf, Switzerland) were applied to determine RNA quantity. The RNA purity was determined by the ratio of absorbance (A260/280), which should vary between 1.8 and 2.2 and meet the requirement of the NGS Core Facility in Mannheim for sequencing. Concerning RNA integrity (RIN), those samples meeting the requirement of A260/280 with a sufficient concentration over 50 ng/µL were submitted to the faculty. RIN values were calculated by the Agilent 2100 Bioanalyzer (Agilent Technologies, Santa Clara, CA, United States). A higher RIN value indicates a better-quality RNA sample.

2.2.11.3 Library preparation

The process of library preparation contains an overall eight steps, including purifying and fragmenting mRNA, synthesizing first strand cDNA, synthesizing second strand cDNA, adenylating 3' ends, ligating anchors, cleaning up fragments, amplifying libraries, and cleaning up library. Following the sequential steps according to the protocol from Illumina, a newly synthesized double-strand cDNA with the anchor was produced before PCR amplification. After steps of library amplification and cleaning up, we utilized the Agilent 2100 Bioanalyzer to check the quality and concentration of libraries.

2.2.11.4 RNA sequencing

With regards to RNA sequencing, 12 total RNA samples from three different groups (control, 4.5 and 18 J/cm² BLI groups) with four repetitions were delivered to the NGS Core Facility in Mannheim for further sequencing.

2.2.11.5 Bioinformatic analysis.

RNA-seq data processing was performed with R (version 4.3.0) and bioconductor (version 3.19) in Rstudio (version 1.1.463). Quality control of clean sequencing reads was performed using FastQC (Babraham Bioinformatics). Low-quality reads were removed using trim_galore (version 0.6.4). The resulting reads were aligned to the human genome version GRCh38.p13 and counted using kallisto version 0.46.1. The

count data was transformed to \log_2 -counts per million (logCPM) using the voom-function from the limma package (3.61.3). Differential expression analysis was performed using the limma package in R. A false positive rate of $\alpha = 0.05$ with false discovery rate (FDR) correction was taken as the level of significance. Volcano plots and heatmaps were created using ggplot2 package (version 3.5.0) and the complexHeatmap package (version 2.0.0). For enrichment analysis, the fgsea, the enrichmentbrowser, and the Enrichr packages were used. The pathway analysis was made with fgsea package and the enrichmentbrowser package in R using the pathway information from KEGG database (<https://www.genome.jp/kegg/pathway.html>). The protein-protein interaction (PPI) network was constructed by Cytoscape (3.10.2) after differentially expressed genes were retrieved from Search Tool for the Retrieval of Interacting Genes (STRING), which was accessed on 17th August, 2024. CytoHubba was used for exploring the importance of nodes in networks constructed by differentially expressed genes.

2.2.12 Statistical analysis.

Data were analyzed using GraphPad Prism (version 8.0.2, San Diego, CA, USA) with an unpaired Student's t-test, one-way ANOVA, or two-way ANOVA to compare groups. The Shapiro–Wilk normality test and Brown–Forsythe test were chosen to test normality and homogeneity of variance, respectively. All numerical data were expressed as either mean \pm standard deviation (SD) or median, interquartile range (25th and 75th percentiles, IQR), maximum, and minimum. A p-value < 0.05 was defined as statistically significant.

3 RESULTS

3.1 LED-based BLI prototype

3.1.1 Temperature measurements

Prior to imposing light treatments on cell lines, it is crucial to understand the thermal impact derived from irradiation. Especially under the condition of long-term irradiation, the biological effects on cells could be influenced by the large quantity of heat generated during the irradiation. The passively generated heat was measured and presented as temperature variation during different irradiation doses.

During the pre-run process lasting for 15 min, all the thermocouples were initially monitored for the thermal values of the environment, corresponding to the RT. These stabilized records acquired by type K thermocouples provided baseline temperature information. Initially, a sharp increase in temperature was observed as the 96-well plate was taken from the incubator maintained at 37 °C. After sudden shifting environments, the recorded temperatures changed drastically based on irradiances for the initial 15 min irradiation. Sensors located at various positions recorded the lowest temperatures with the irradiance of 10 mW/cm², which ranged from 23.5 to 27.8 °C. With the irradiance of 23 mW/cm², the temperature range was wider compared to 10 mW/cm²: Temperatures in the medium and above were both over 5 °C higher than those measured between wells (33.7 and 34.4 °C vs. 28.0 °C, respectively). With regard to the irradiance of 40 mW/cm², temperatures of positions 1 and 2 were still over 6 °C higher than the temperature of position 3 (42.6 and 43.6 °C vs. 36.4 °C, respectively). During the next 15 min, temperatures gradually dropped or climbed to relatively stable levels, albeit to a smaller extent. The temperature after 40 mW/cm² irradiation increased by over 1 °C during this period, regardless of position. And corresponding temperatures reached 44.8, 45.9, and 38.6 °C, respectively. In contrast, the variations in temperature following 10 and 23 mW/cm² irradiation remained within 1 °C.

Finally, temperatures gradually stabilized within a range of 24 to 27 °C and 31 to 37 °C for 10 and 23 mW/cm² BLI, respectively. (Figure 19A and B). After 2 hours of irradiation with an irradiance of 40 mW/cm², the temperature increased continuously,

reaching its highest values at 48.6, 49.0, and 41.6 °C in positions 1, 2, and 3, respectively (Figure 19C).

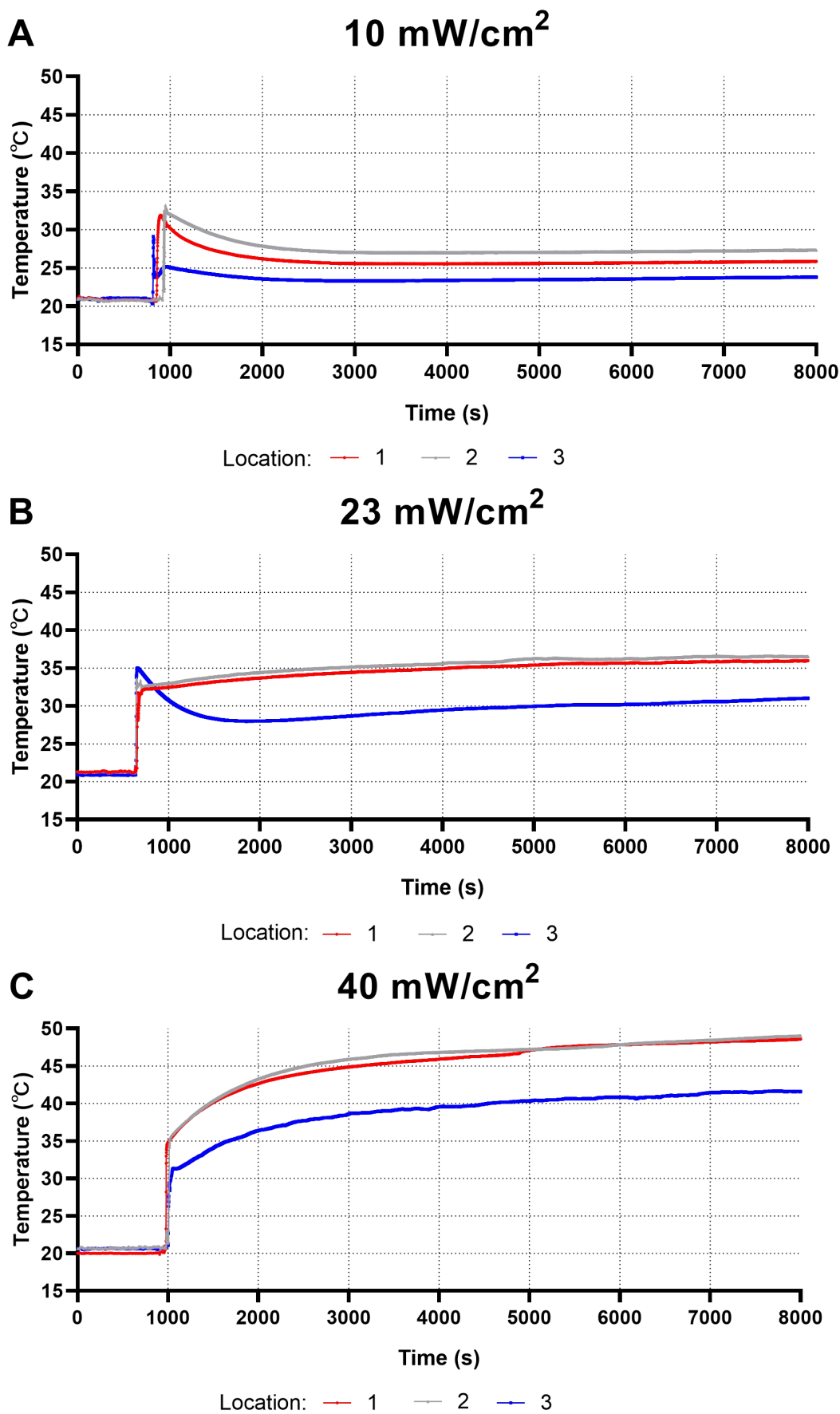


Figure 19. Temperature measurements in the 96-well black cell culture plate upon irradiation with 10, 23, and 40 mW/cm² (A, B, and C). The temperatures were recorded at three different locations. 1: The thermal changes in the medium; 2: The air temperature inside the well, and 3: The variation of temperature in the gap between two adjacent wells (which is not exposed directly to the light irradiation). Three independent experiments were performed (n = 3 repetitions). Data are shown as mean values from these experiments.

3.1.2 Distribution of light intensities

Before the in vitro experiments on cells, it is important to understand the light homogeneity on the 96-well plate in order to select areas that received light treatments appropriately. Through the photodiode-based device specific for visual light at the wavelength of 450 nm, light intensities were quantified, which facilitated further comparisons.

Figure 20A illustrates that higher light intensities were converted and displayed by a photodiode in the central area from columns 3 to 10, compared to the rest of the columns close to the edges. A 3D surface plot with contour lines shows the central area of the plate received more energy than areas on the edges. As shown in Figure 20B, values of light intensities were normalized to the maximum and projected to a 2D heatmap. Evidently, the light intensities at the edges of the plate (columns 1 and 12) were lower than those of other wells and approximately 10% lower than the maximum at A7. Moreover, both corners of H1 and H12 exhibited over 12% lower values in terms of light intensity. After quantification, all the data measured concerning light homogeneity were consistent with the data and conclusions provided by URG0.

Based on all the data presented below and suggestions from URG0 as well, on a 96-well plate, we exposed wells from C3 to F5 to BLI (12 wells in total) and designed a geometrically symmetrical area (C8 to F10) as controls (without irradiation), accordingly.

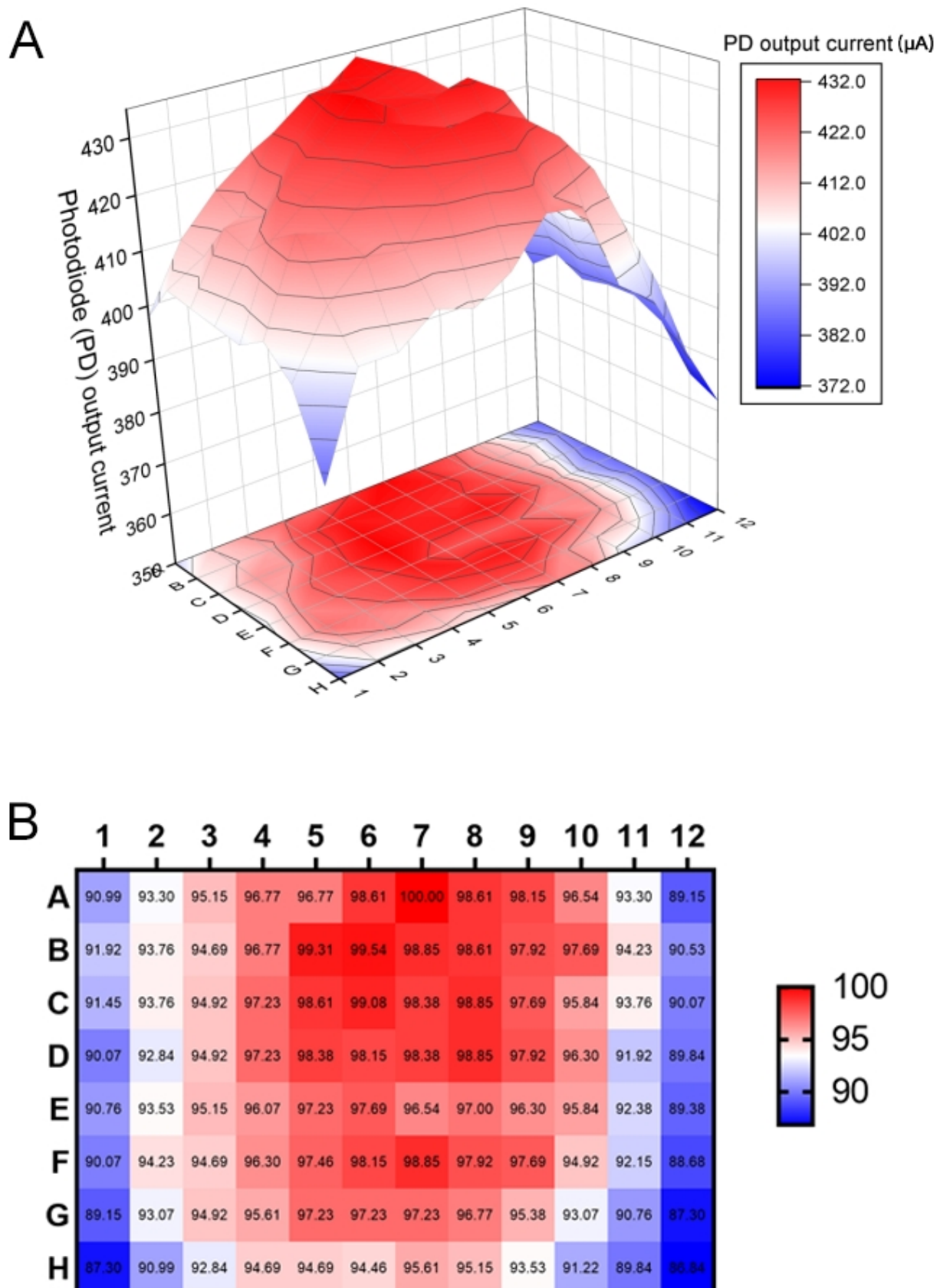


Figure 20. 3D surface plot (A) of light homogeneity, data are presented as current (μA). 2D heatmap (B) of light distribution at an irradiance of 23 mW/cm^2 . Data are presented as percentages (%) after normalization. The data shown in wells are mean values or normalized mean values ($n = 3$ repetitions).

3.2 Effects of BLI on cell viability and proliferation with different irradiances.

Overall, a clear biphasic response to BLI was observed in all the cell lines at all the irradiances used in the XTT assay.

In HaCaTs, BLI with the power density of 7 mW/cm² for 12 min (5.04 J/cm²) triggered the maximum increase in XTT absorbance of 11.5% compared to the non-irradiated cells. BLI at 10 mW/cm² with an irradiation duration of 7.5 min (4.5 J/cm²) resulted in a 6.7% rise in cell viability, and with 23 mW/cm² irradiance for the first 2.5 min (3.45 J/cm²), the cellular activity increased by 9.5% (Figure 21A). There were definitely downward trends in cell viability as the irradiation doses increased. After 20 min of irradiation with all irradiances, cell viability dropped dramatically and was significantly lower than the control group ($p < 0.0001$). With 120 min of irradiation irrespective of irradiance, reductions in cell viability were observed with 13.8% for 7 mW/cm², 19.8% for 10 mW/cm² and 13.5% for 23 mW/cm², respectively ($p < 0.0001$), in comparison to non-irradiated cells. Generally, with the increase of irradiation dose, the level of cell viability gradually decreased, even though the fluctuation presented during certain periods of time.

Not all changes in cell viability were paralleled by tendencies of cellular proliferation. During the first 20 min of irradiation on HaCaTs, there were no significant differences in cell proliferation after comparing with controls ($p > 0.05$). Only slight increases of 2.7%, 1.7%, and 1.8% were observed at 5, 10, and 2.5 min of irradiation, with irradiances of 7, 10, and 23 mW/cm², respectively. However, a clear decrease in cellular proliferation was observed with irradiation time which was longer than 20 min. A 15.9% decrease in cell proliferation was observed after 120 min of irradiation with the irradiance of 7 mW/cm² ($p < 0.0001$). A 15.1% decrease was observed when irradiation at 10 mW/cm² for 120 min ($p < 0.0001$), and BLI at 23 mW/cm² for 120 min induced a 31.2% decrease in the level of cell proliferation ($p < 0.0001$) in comparison to the non-irradiated controls (Figure 21B).

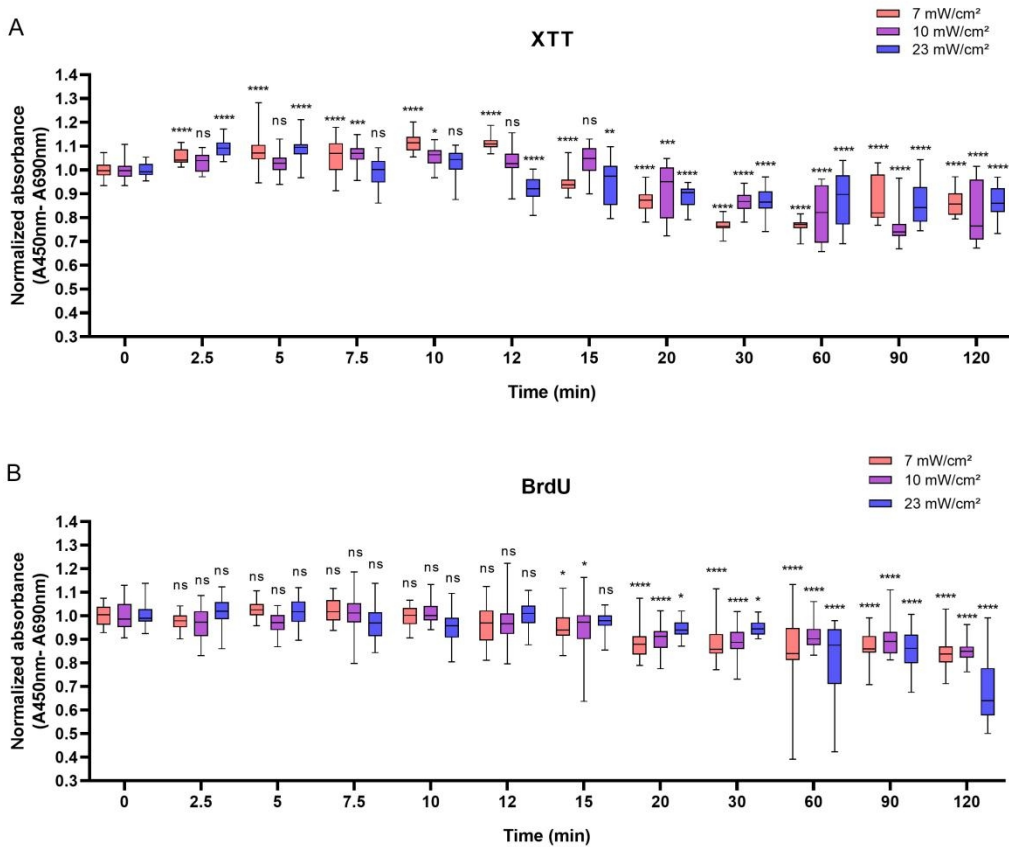


Figure 21. Response of HaCaTs after BLI with 0–120 min irradiation with 7, 10 and 23 mW/cm² in terms of (A) cell viability measured by XTT and (B) cellular proliferation measured by BrdU, 24 h after irradiation. For both the assays, the absorbance was normalized and compared to non-irradiated controls. Data are shown as boxplots with medians, IQRs and error bars for outliers ($n = 3$ repetitions, *: $p < 0.05$, **: $p < 0.01$, ***: $p < 0.001$, ****: $p < 0.0001$, ns: not significant, one-way ANOVA: Dunnett's test).

Like HaCaTs, NHDFs also responded in a biphasic manner to the light treatments, with an increase in cell viability at a shorter irradiation duration of up to 12 minutes and a decrease at a longer irradiation time, i.e., longer than 20 minutes (Figure 22A). While a modest increase of 10% was observed with 7 mW/cm² at 12 min (5.04 J/cm²), a peak value of 8.9% higher than the control group was observed with irradiation at 10 mW/cm² at 7.5 min (4.5 J/cm²). A marginal increase of 6.4% was noted using 23 mW/cm² for 7.5 min (10.35 J/cm²). Cellular proliferation also exhibited a bi-phasic characteristic, and an increase in cell viability in NHDFs was not always followed by an increase in cellular proliferation. When the light treatment with 7 mW/cm² BLI was applied, cell proliferation increased by 8.8% at 2.5 min (1.05 J/cm²). Paralleling an increase in irradiance from 10 to 23 mW/cm², a minor increase in cellular proliferation was observed from 6.8% at 7.5 min (4.5 J/cm²) ($p < 0.01$) to 13.2% at 12 min (16.56 J/cm²) ($p < 0.0001$, Figure 22B). After NHDFs were exposed to BLI for longer than 20 min, proliferation declined, and finally with 23 mW/cm² BLI, the cell proliferation

dropped by 47.8% ($p < 0.0001$) as compared to controls. With 7 and 10 mW/cm² BLI, a drop in cellular proliferation by 18.1% and 15.1% was also observed, respectively, yet the magnitude was much lower than 23 mW/cm² (Figure 22B).

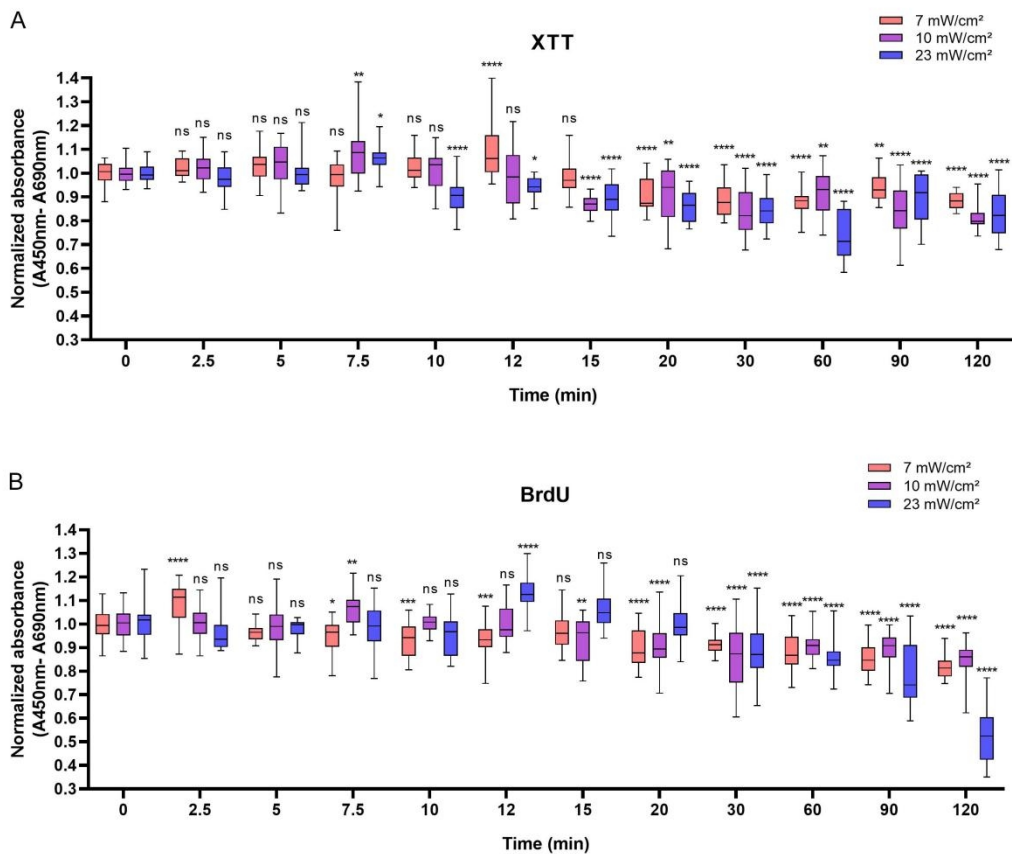


Figure 22. Overview of the response of NHDFs to BL with 0–120 min irradiation using 7, 10 and 23 mW/cm² by XTT and BrdU. The absorbance was normalized and compared to non-irradiated controls. A: Changes of cell viability under three light irradiances (7, 10, and 23 mW/cm²) 24 h after BLI, ranging from 0 to 120 min. B: Changes in cell proliferation measured 24 h after irradiation and grouped by the irradiation time from 0 to 120 min, as shown on the x-axis. Data are shown as boxplots with medians, IQRs and error bars for outliers ($n = 3$ repetitions, *: $p < 0.05$, **: $p < 0.01$, ***: $p < 0.001$, ****: $p < 0.0001$, ns: not significant, one-way ANOVA: Dunnett's test).

HUVECs also responded bi-phasically to the BLI. Lower power density (7 mW/cm²) irradiation caused a peak in cell viability of 13.7% compared to the non-irradiated controls at 12 min (5.04 J/cm²). At 10 min, higher power densities led to peaks of 8.1% and 5.9% for 10 mW/cm² (6 J/cm²) and 23 mW/cm² (13.8 J/cm²), respectively (Figure 23A). Similar to HaCaTs and NHDFs, an increase in cell viability did not correspond to the increase in cell proliferation in HUVECs. Irradiation with the power densities of 7, 10, and 23 mW/cm² increased proliferation by 16.1% ($p < 0.0001$) at 7.5 min, 5.9% ($p < 0.05$) at 7.5 min, and 11.7% ($p < 0.0001$) at 5 min, respectively. With an irradiation time of longer than 20 min, a decline in cell proliferation was

observed with a drop of 11.3% and 14.0% compared to the controls using 7 mW/cm² and 10 mW/cm² BLI at 120 min, respectively. At the irradiance of 23 mW/cm², a slight decrease by 12.6% ($p < 0.0001$) compared to the non-irradiated group at 120 min was observed (Figure 23B).

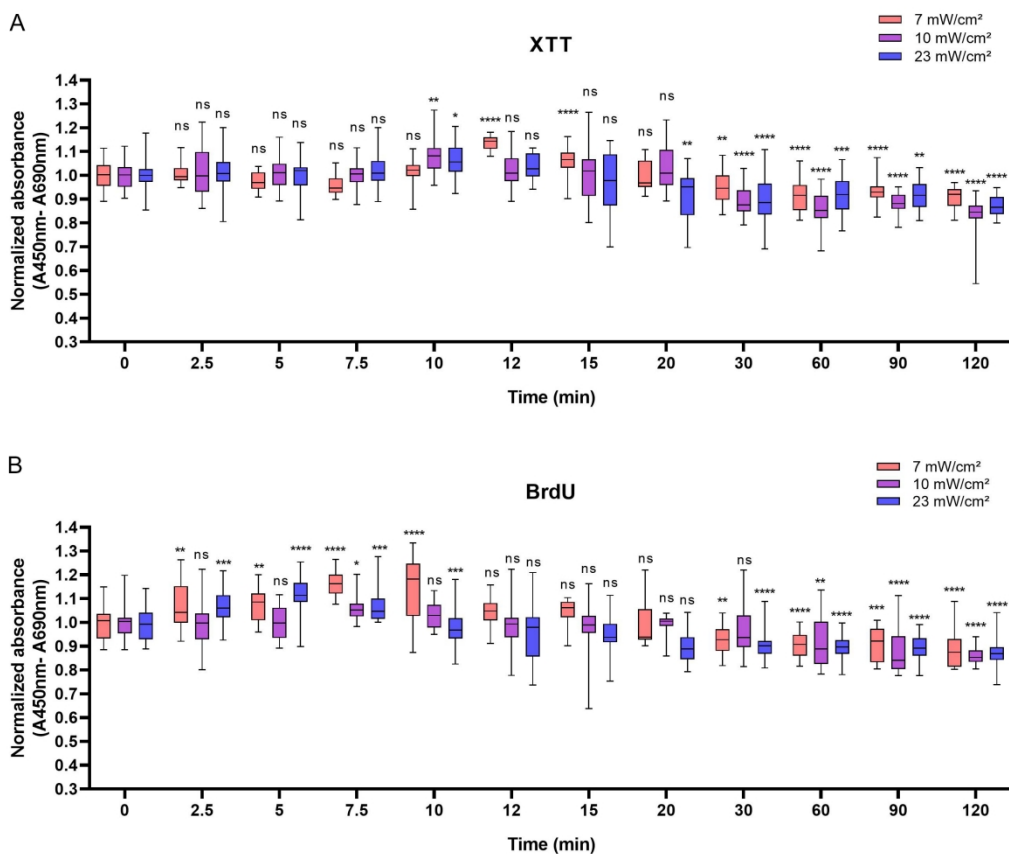


Figure 23. Overview of the response of HUVECs to BLI over 0–120 min with 7, 10 and 23 mW/cm² by XTT and BrdU. The absorbance was normalized and compared to non-irradiated controls. A: The normalized absorbance measured by XTT 24 h after BLI (7, 10 and 23 mW/cm²), duration of light treatment varied from 0 to 120 min. B: Changes of newly synthesized DNA 24 h after BLI with different irradiances of 7, 10 and 23 mW/cm². Data are shown as boxplots with medians, IQRs and error bars for outliers ($n = 3$ repetitions, *: $p < 0.05$, **: $p < 0.01$, ***: $p < 0.001$, ****: $p < 0.0001$, ns: not significant, one-way ANOVA: Dunnett's test).

In this in vitro study, our primary focus was the biostimulation effect following BLI on three cell types, which involved in biological processes of wound healing and angiogenesis. Therefore, after a comprehensive consideration of all the factors, including the effects of light doses on cells, thermal issues during irradiation, and the previous experimental settings, we selected an irradiance of 10 mW/cm² for durations of 7.5 (4.5 J/cm²) and 10 min (6 J/cm²) on the subsequent ATP quantification to explore the variation of ATP synthesis by HaCaTs, NHDFs, and HUVECs after the irradiation. For the sequential light treatment, the above-mentioned fluence of 4.5

J/cm^2 was selected as the dose of irradiation, following a long-term irradiation for 2 or 5 h with an irradiance of 23 mW/cm^2 .

3.3 Long-term BLI on three cell types

3.3.1 BLI utilizing 10 mW/cm^2 irradiance for 7h.

The above-mentioned assays focused on cellular responses to short-term irradiation with different irradiances. Based on that, assays of cell viability after a relatively long-term irradiation were conducted in order to assess the corresponding cellular responses. As seen in Figure 24, cell viability of HaCaTs was not significantly different from that of controls after 7 h of exposure to RT, though it did drop by 1.8% ($p > 0.05$). Whereas HaCaTs exposed to irradiation with the irradiance of 10 mW/cm^2 for 7 h had a decreased cell viability of 26.8% compared with controls ($p < 0.0001$). Both cell types of NHDFs and HUVECs demonstrated comparable trends in cell viability after prolonged exposure (7 h) to RT and irradiation. Cell viability of NHDFs and HUVECs significantly decreased by 12.8% and 13.7% after 7 h RT exposure, respectively ($p < 0.0001$). Finally, after a long time of irradiation with an irradiance of 10 mW/cm^2 , NHDFs experienced a greater drop of 52.5% compared to only 26.8% in HUVECs.

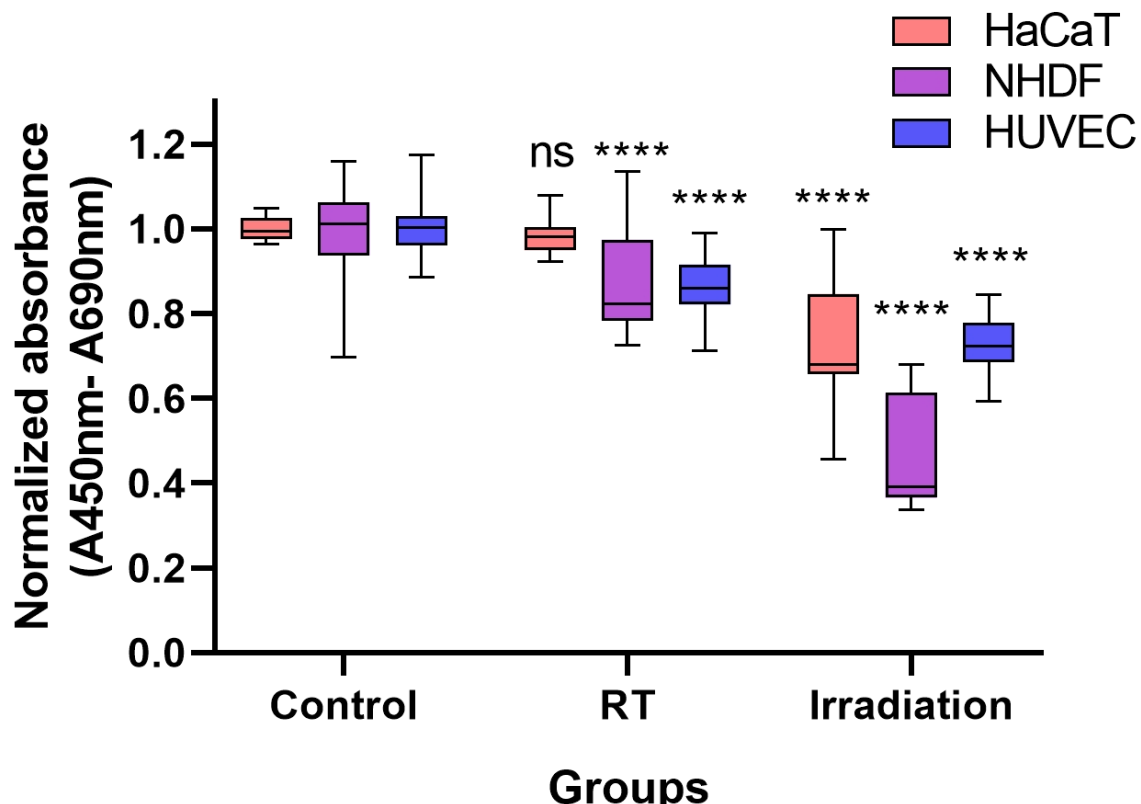


Figure 24. Cell viabilities of HaCaTs, NHDFs and HUVECs under three conditions: Non-irradiated controls, RT and 7h irradiation with 10mW/cm^2 irradiance. Data were normalized to controls. Data are shown as boxplots with medians, IQRs and error bars for outliers ($n = 3$ repetitions, ****: $p < 0.0001$, ns: not significant, one-way ANOVA: Dunnett's test).

3.3.2 BLI utilizing 23 mW/cm^2 irradiance for long-time irradiation.

In the next step, cellular responses to the long-time irradiation with a higher irradiance of 23 mW/cm^2 were further investigated as well. In Figure 25A, it was clear that the metabolic activities of NHDFs and HUVECs went down after 2 hours of irradiation with an irradiance of 23 mW/cm^2 . And they gradually declined and fell to the lowest normalized values of 0.376 after 6h irradiation and 0.473 after 7 h of BLI ($p < 0.0001$). Notably, 4 h of irradiation inhibited the viability of HaCaTs by 57.5%, rendering the level of cell viability lower than the other doses of irradiation added to this cell line. Subsequently, there was a gradual increase in cell viability. Ultimately, following 9 h of BLI and the 24 h of incubation, the quantification of cell viability reached a level of 0.693 compared to controls. Overall, the 23 mW/cm^2 irradiation significantly reduced cell viability of all three cell types in comparison to cells that were not exposed to irradiation.

Meanwhile, an additional group of the same cell lines exposed to RT provided supplementary information for further comparisons (Figure 25B). Different from the responses after irradiation with irradiance of 23 mW/cm^2 , cell lines under RT had a much slower rate of decrease in cell viability and finally declined by 4.8%, 8.4%, and 11.3% after 9, 7, and 7 h of irradiation, respectively.

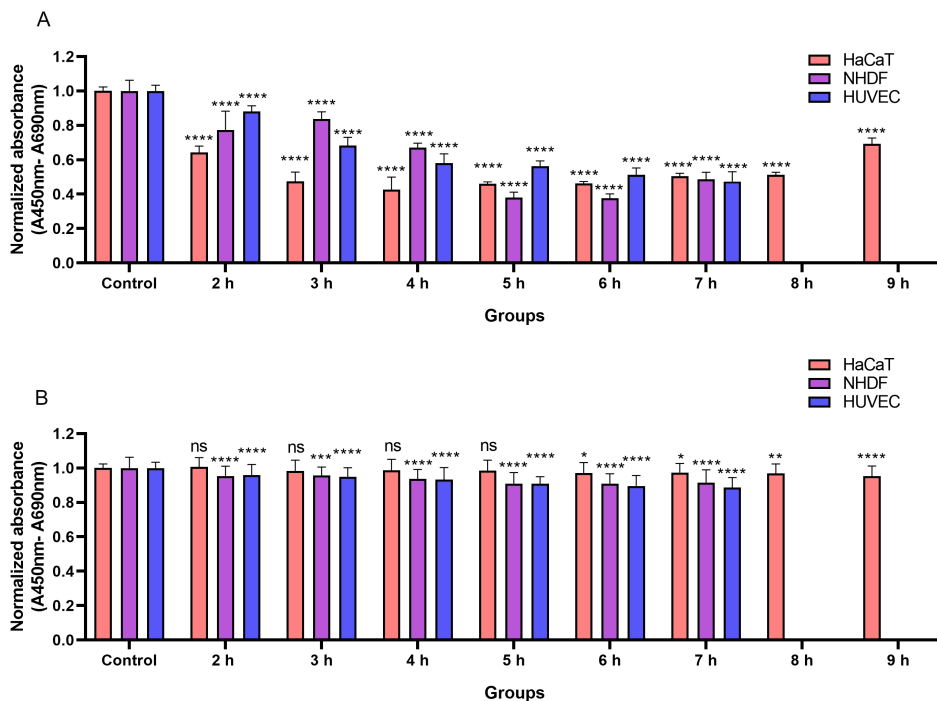


Figure 25. Cell viability after long-time BLI with irradiance of 23 mW/cm² on three cell types in A, and cell viability changes after different exposure time at RT in B. Data are shown as bar charts with mean \pm SD (n = 3 repetitions, *: p < 0.05, **: p < 0.01, ***: p < 0.001, ****: p < 0.0001, ns: not significant, one-way ANOVA: Dunnett's test). Absorbance was normalized by comparison to controls.

3.3.3 Sequential light treatments

3.3.3.1 Cell viability measurement after sequential light treatments

In group C, after HaCaTs which were exposed to 23 mW/cm² of light for 2 h (Figure 26A), viability of HaCaTs dropped by 48.1% after the light treatment. Then gradually the normalized cell viability recovered and rose to the level of 0.592 obtained on the next day without the irradiation of 10 mW/cm². The subsequent 4.5 J/cm² BLI exposure resulted in a 3.2% increase in cell viability (p < 0.01). The number of active cells in group A was slightly higher (3.0%) than those in group E (p < 0.05), but there was no significant difference in the number of metabolically active cells between groups E and cells that had been harvested 48 h after the long-time exposure in group D.

After increasing the irradiation dose and reaching the exposure time of up to 5 h, a comparable pattern of cellular behaviors were observed in Figure 26B. HaCaTs demonstrated a 2.1% higher cell viability in group B following a comparison with group D (p > 0.05). After comparing cell viability of groups A and E, we also observed a significant increase of 3.7% in terms of cell viability in group A (p < 0.0001). A

spontaneous increase of cell viability in HaCaTs without adding 4.5 J/cm² BLI was seen in group E, compared to group D ($p < 0.05$).

With regard to cell viability changes on NHDFs, long-term irradiation lasting for 2 h caused a 33.8% drop compared to controls (Figure 27A). Similar to the responses of HaCaTs, the level of cell viability in NHDFs immediately increased and reached 0.769 on the next day compared to non-irradiated controls. And 4.5 J/cm² irradiation induced an increase of cell viability by 4.5% ($p < 0.001$) in group B. Though there was still a rising trend in group A, no significant difference was observed between groups A and E ($p > 0.05$), which is different from the finding acquired in HaCaTs under the same condition.

When cells were exposed to 23 mW/cm² of irradiation for 5 h, activity of NHDFs dropped significantly, and cell viability dropped to 0.374 compared to controls (Figure 27B). After the subsequent cell culture and adding 4.5 J/cm² BLI to NHDFs, no significant difference was observed when comparing cell viability in groups B and D, and group A and E, respectively ($p > 0.05$). The cell viability continuously declined to the relative level of 0.282 in group E, compared to controls. This was significantly lower than the normalized value acquired in group D ($p < 0.0001$).

Finally, we applied the same schedule of light treatments to HUVECs, displaying results of the comparisons in Figure 28A. After 2 h of irradiation with an irradiance of 23 mW/cm², cell viability dropped by 40.8% compared to controls. As with biological responses of the other two cell types that were treated with sequential light, 4.5 J/cm² BLI increased cell viability of HUVECs by 4.5% ($p > 0.05$) in group B and 8.3% ($p < 0.001$) in group A, comparing the normalized values in groups D and E, respectively. The spontaneous rehabilitation of cell viability could also be seen when comparing normalized values in groups D and E (0.662 vs. 0.716, $p < 0.05$).

The 5 h of irradiation with an irradiance of 23 mW/cm² significantly impacted the cell viability of HUVECs, causing the normalized value of cell viability to drop to 0.517 compared to controls (Figure 28B). During the subsequent days, the level of cell viability continuously declined, finally falling to 0.361, as measured on the last day in group E without extra irradiation (cells harvested 72 h after long-term irradiation). After adding an extra 4.5 J/cm² dose of irradiation to groups B and A, there were no significant differences between the normalized values obtained in group A and E,

group B and D, respectively. A continuous decline of cell viability with time can be noticed when comparing the normalized values in groups E and C ($p < 0.0001$).

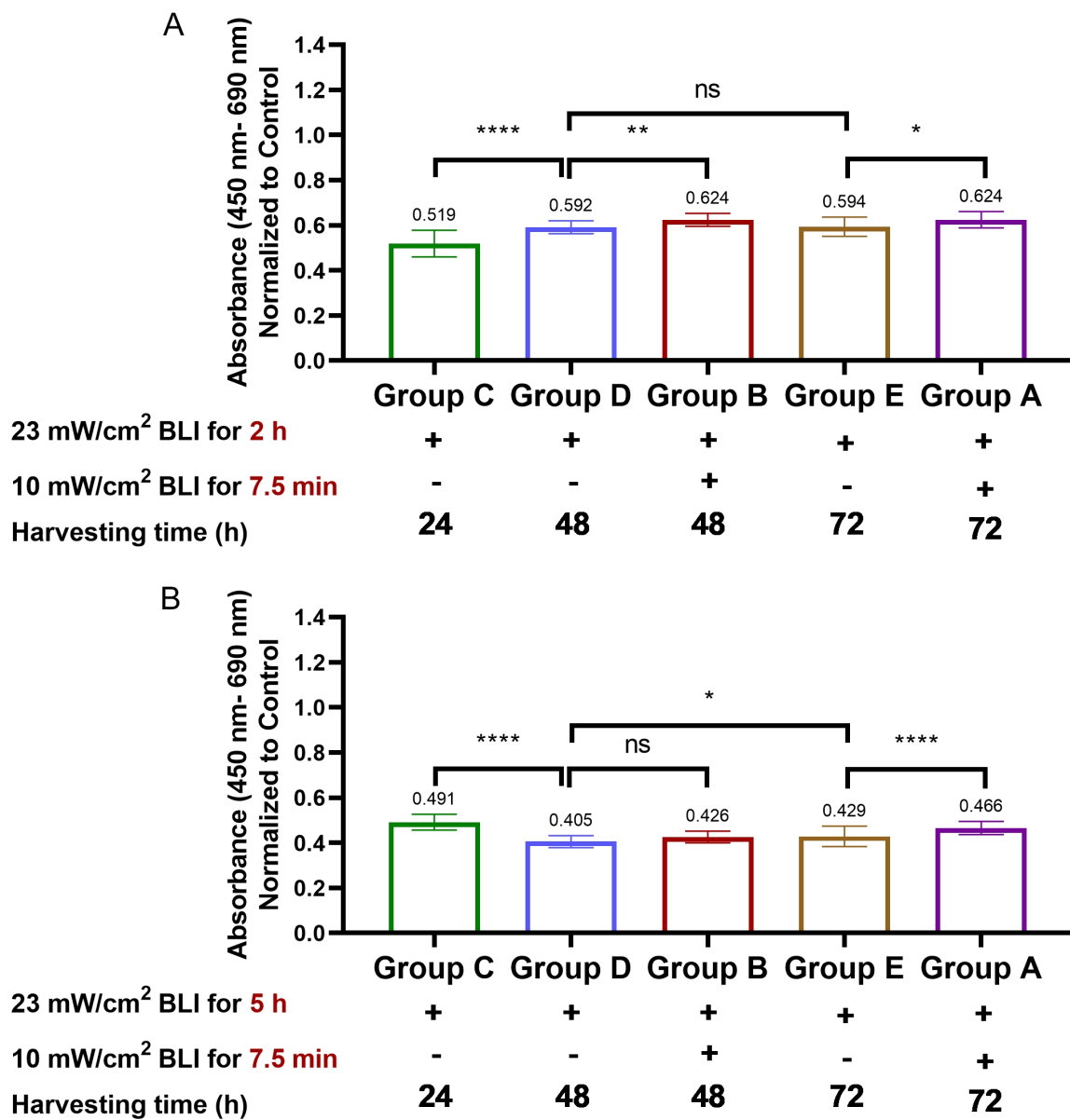


Figure 26. Viability of HaCaTs after sequential light treatment with irradiance of 23 mW/cm² for 2 h (A) and 5 h (B) irradiation followed by treatment protocols with/without further 4.5 J/cm² irradiation. Data are shown as bar charts with mean \pm SD ($n = 3$ repetitions, *: $p < 0.05$, **: $p < 0.01$, ****: $p < 0.0001$, ns: not significant, one-way ANOVA: Tukey HSD test). The absorbance of each group was normalized by comparisons to non-irradiated controls.

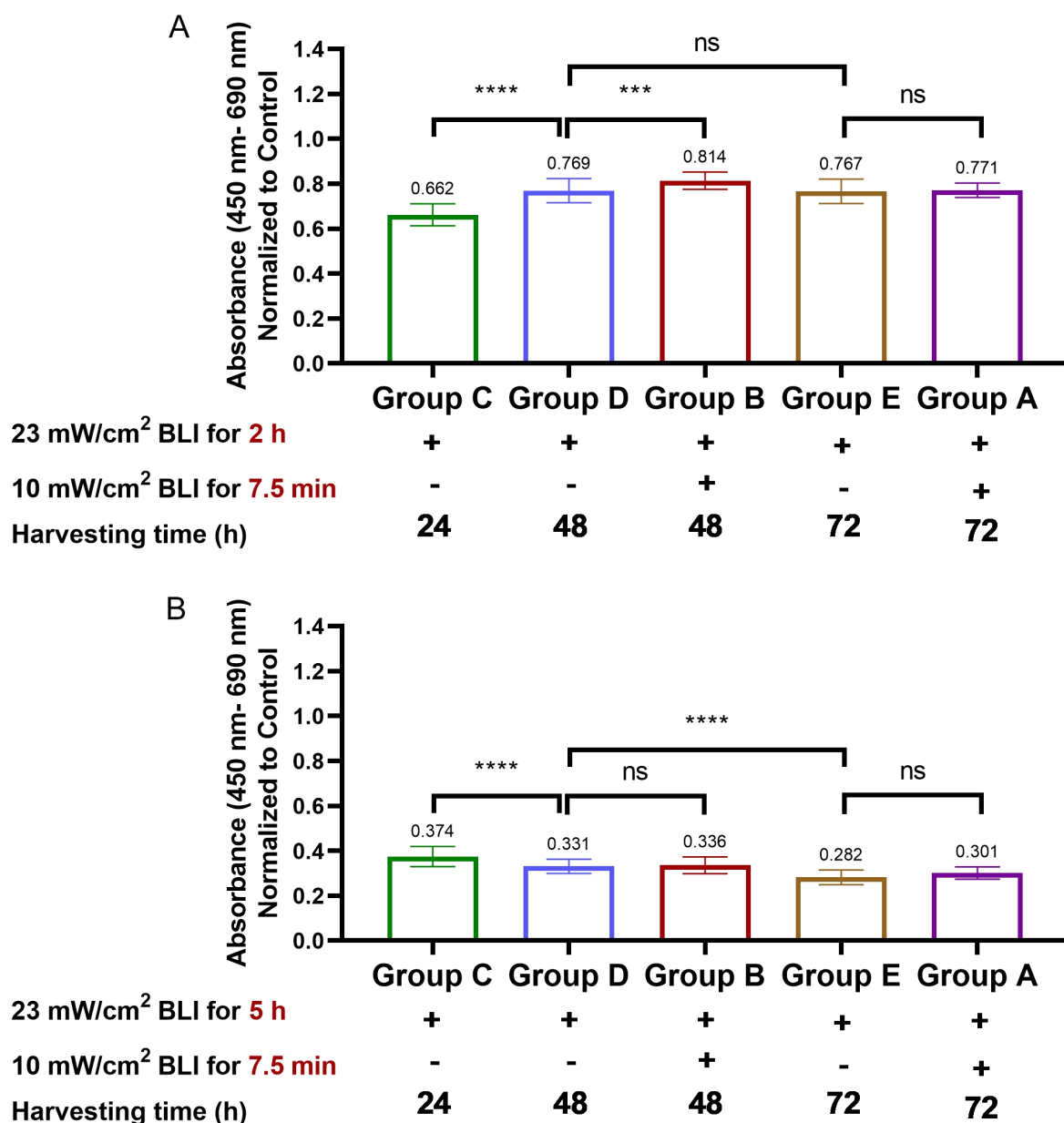


Figure 27. Changes of cell viability after long-term irradiation (2 and 5 h) at the irradiance of 23 mW/cm² on NHDFs along with 4.5 J/cm² BLI and corresponding controls: The sequential light treatments utilizing 2 h irradiation in A. And 5 h irradiation with 23 mW/cm² followed by 4.5 J/cm² BLI in B. Data are presented as bar charts with mean \pm SD ($n = 3$ repetitions, **: $p < 0.01$, ***: $p < 0.001$, ****: $p < 0.0001$, ns: not significant, one-way ANOVA: Tukey HSD test). Normalized absorbance was calculated by comparing to non-irradiated controls.

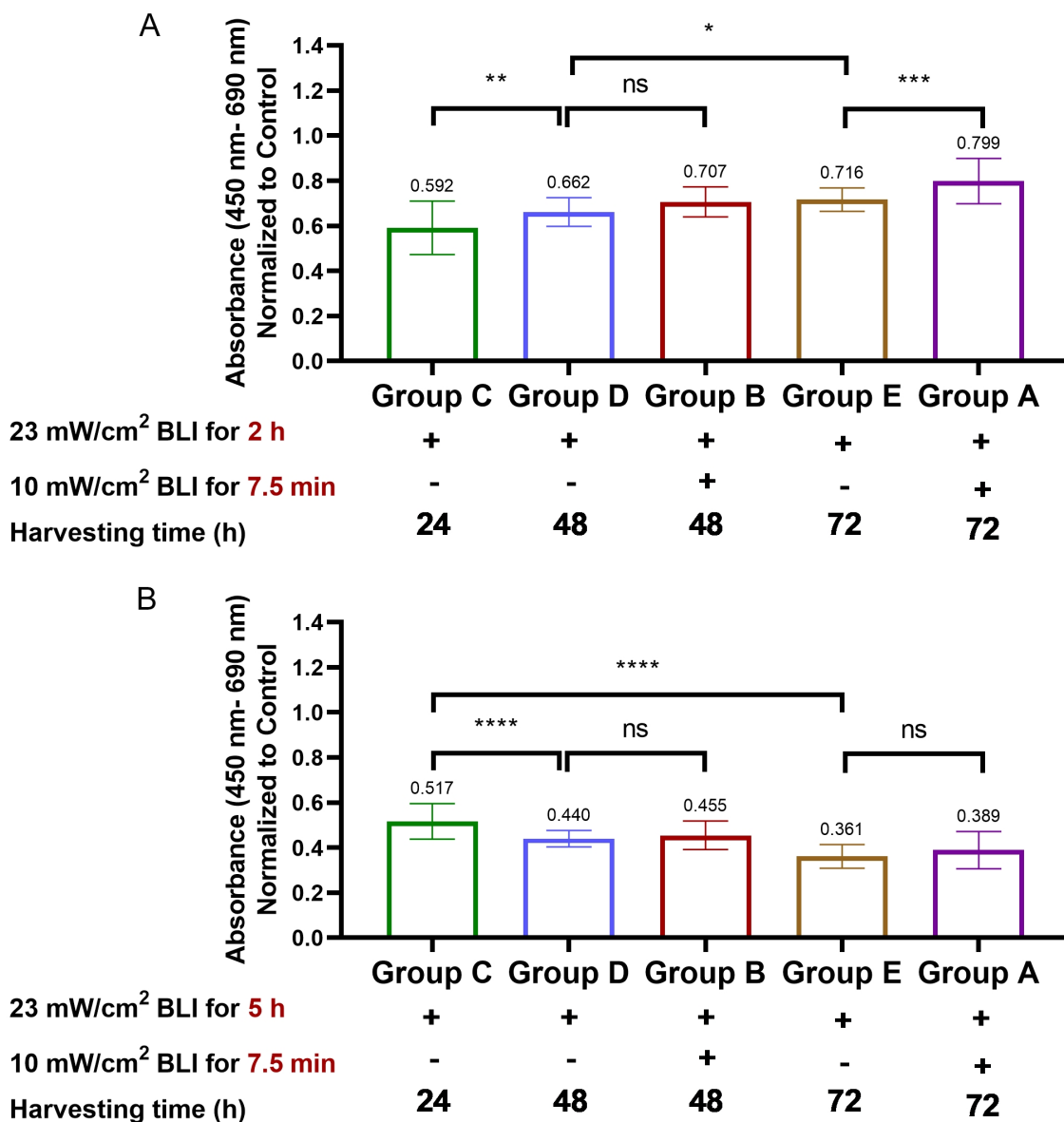


Figure 28. Variation of cell viability after BLI with different exposure time (2 and 5 h in A and B, respectively) followed by treatment of a low fluence (4.5 J/cm^2) on HUVECs. Data are presented as bar charts with mean \pm SD ($n = 3$ repetitions, *: $p < 0.05$, **: $p < 0.01$, ***: $p < 0.001$, ****: $p < 0.0001$, ns: not significant, one-way ANOVA: Tukey HSD test). All data were normalized by comparing with controls.

3.3.3.2 ATP quantification after sequential light treatments

The next phase involved measuring ATP quantification to investigate ATP synthesis in three cell lines following sequential light treatments with two irradiances (10 and 23 mW/cm²). In the last section, cell viability assay results provided the basis for ATP quantification after the same sequential light treatments. Therefore, an exposure irradiation time of 2 h was determined for assays in this section.

In terms of HaCaTs, 2 h irradiation with 23 mW/cm² caused a decreased level of ATP synthesis, resulting in normalized luminescence of 0.519 compared to controls without irradiation (Figure 29A). The quantification of ATP then steadily increased. The normalized luminescence after cell harvesting (72 h after long-term irradiation) reached 0.586, without any 4.5 J/cm² irradiation. However, by adding 4.5 J/cm² BLI, the progress of ATP synthesis was stimulated: Cells in groups B and A had significantly higher normalized luminescences than cells in groups D and E that had not been treated with sequential light treatments ($p < 0.001$ and $p < 0.0001$, respectively). We observed a spontaneous increase in ATP quantification when we compared the normalized values between groups D and E (0.586 vs. 0.527).

When 2h of long-term irradiation was added to NHDFs, a significant increase in normalized luminescence was observed comparing values of NHDFs harvested 72 h after the low-fluence irradiation at 4.5 J/cm² in groups A and controls group E ($p < 0.0001$) (Figure 29B). When the harvesting time was shortened to 48 hours after the irradiation, no difference in normalized luminescence was observed between groups B and D.

The analogous responses were found on ATP quantification after sequential light treatments were applied to HUVECs: A fluence of 4.5 J/cm² BLI increased the normalized luminescence by 6.1% comparing values of groups A and E ($p < 0.05$), and the normalized value in group A was close to the control group without irradiation, at 0.948 (Figure 29C).

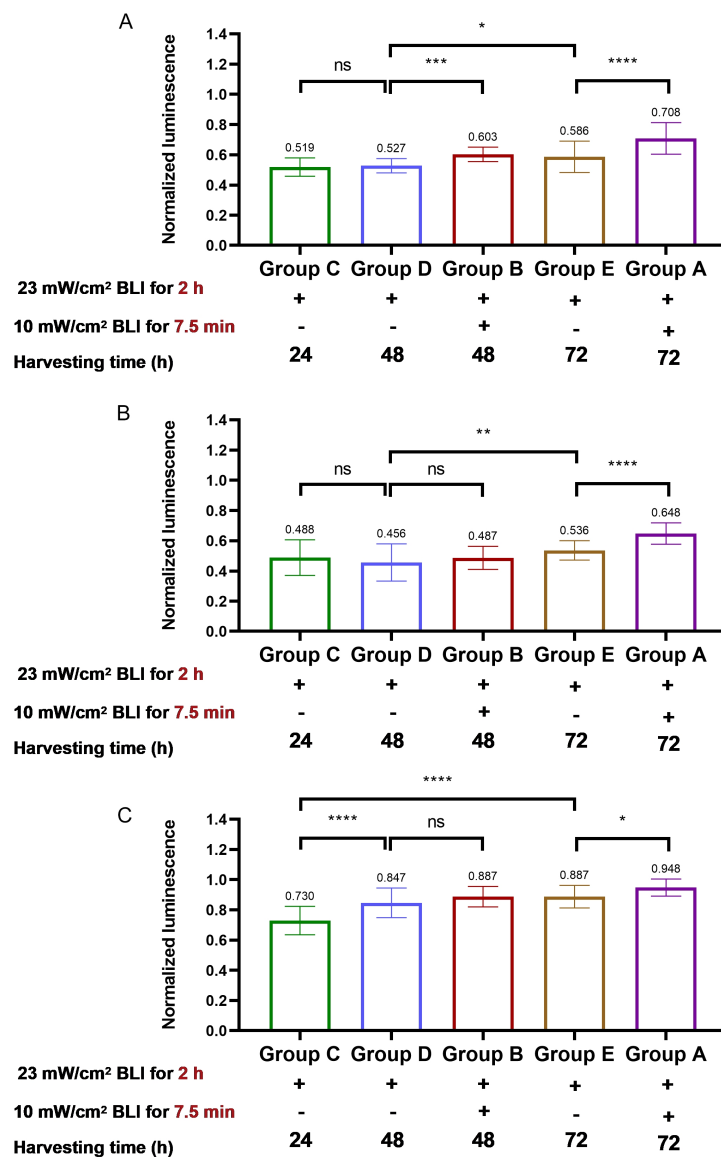


Figure 29. The quantification of ATP synthesis after sequential light treatments with two irradiances of 23 and 10 mW/cm². Groups were designed according to the harvesting time and treatment after long-term irradiation. A, B, and C show condition of ATP synthesis in HaCaTs, NHDFs, and HUVECs. Data are presented as bar charts with mean \pm SD (n = 3 repetitions, *: p < 0.05, **: p < 0.01, ***: p < 0.001, ****: p < 0.0001, ns: not significant, one-way ANOVA: Tukey HSD test). The normalized luminescence was calculated by comparison to controls without irradiation.

3.3.4 Cell viability after alteration of cell culture conditions

Furthermore, cell viability following different cell culture conditions and more treatment protocols was assessed to explore potential factors which influenced cellular behaviors.

3.3.4.1 Influences of direct medium irradiation and phenol red on cell viability

Factors of phenol red and medium irradiation were involved in the following assays measured by XTT: In HaCaTs, after irradiating the medium with a fluence of 6 J/cm^2 , there was no statistically significant difference ($p > 0.05$) between groups with or without phenol red (Figure 30A), with the normalized absorbance at 1.024 and 1.029 in the phenol red group and phenol red-free group, respectively. Medium irradiation significantly increased cell viability by 2.4% in the phenol red group and 2.9% in the phenol red-free group, comparing with their corresponding controls ($p < 0.05$).

There were some differences found from bar charts of medium irradiation for 7.5 and 10 min on NHDFs at the irradiance of 10 mW/cm^2 , corresponding to fluences of 4.5 and 6 J/cm^2 (Figure 30B and C). There was a 6.5% increase in cell viability in the phenol red group ($p < 0.0001$) and a 3.5% increase in the non-phenol red group ($p < 0.05$) after 7.5 min of irradiation on medium, whereas the presence of phenol red had no influence on cell viability after comparison. In contrast, there was only a marginal increment of cell viability after 6 J/cm^2 irradiation: 0.1% in the phenol red group and 1.2% in the phenol red-free group (both $p > 0.05$). Similar to the findings after 4.5 J/cm^2 BLI, phenol red has no significant influence on cell viability after comparison between normalized values in the phenol red group and those in the non-phenol red group after 6 J/cm^2 medium irradiation.

As shown in Figure 30D, HUVEC medium exposed to 6 J/cm^2 radiation significantly increased cell viability by 7.9% ($p < 0.0001$) with phenol red and 6.3% ($p < 0.0001$) without phenol red. Moreover, the component of phenol red did not influence cell viability after medium irradiation ($p > 0.05$).

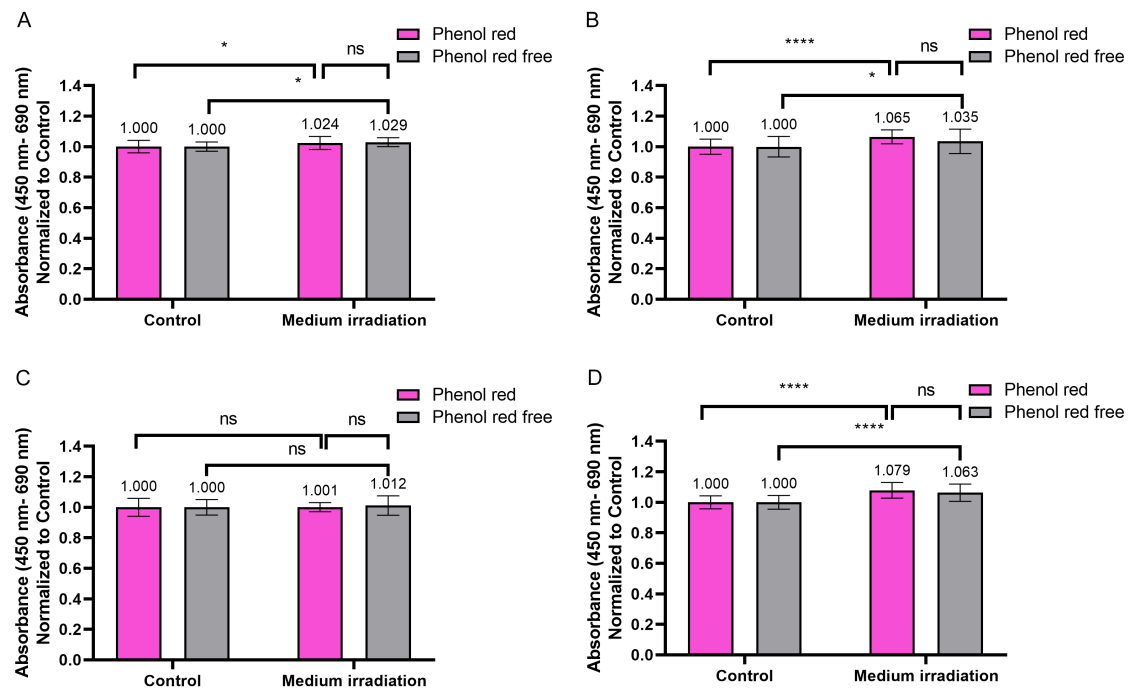


Figure 30. Cell viability assays after medium irradiation on HaCaTs, NHDFs, and HUVECs with/without the presence of phenol red. A: 6 J/cm² BLI on HaCaTs. B and C: 4.5 and 6 J/cm² BLI on NHDFs. D: 6 J/cm² BLI on HUVECs. Normalized absorbances were calculated by comparing to controls. Data are presented as bar charts with mean \pm SD, with mean values shown above error bars ($n = 3$ repetitions, *: $p < 0.05$, ****: $p < 0.0001$, ns: not significant, two-way ANOVA: Sidak's multiple comparison).

3.3.4.2 Irradiation on cells, transfer of irradiated medium, and medium refreshment influenced cell viability

In this section, we supplied four cell culture conditions with three cell lines at an irradiance of 10 mW/cm² to investigate cell viability under different treatment protocols. The details of protocols are described in Section 2.2.10.

In Figure 31A, HaCaTs in group 4 after irradiation with blue light had the highest normalized value at 1.076 ($p < 0.0001$). The influence of irradiation on cell viability was attenuated after medium refreshment in group 3. And the normalized absorbance stabilized at 1.002, which was at a relatively low level, and there was no significant difference compared to controls. In group 2, irradiation on both the medium and HaCaTs followed by only medium transfer resulted in 4.4% higher cell viability than controls ($p < 0.05$).

In terms of NHDFs, irradiation increased cell viability with fluences of 4.5 and 6 J/cm², although there were some differences (Figures 31B and C). The number of active cells in group 2 went up by 4.2% and 4.8% after medium transfer following

simultaneous medium and cells irradiation at 4.5 and 6 J/cm² BLI, respectively. The differences between the other two treatment groups (medium refreshment in group 3, cells and medium irradiation in group 4) and controls were not statistically significant after 6 J/cm² BLI ($p > 0.05$). In contrast, the obviously different findings were observed after 4.5 J/cm² BLI (group 2 vs. control: $p < 0.01$, group 3 vs. control: $p < 0.001$).

The normalized values of cell viability in HUVECs fluctuated within a relatively small range after 6 J/cm² BLI. Comparing the normalized value in group 4 to controls yielded only a 3.8% increase in cell viability ($p < 0.001$) (Figure 31D).

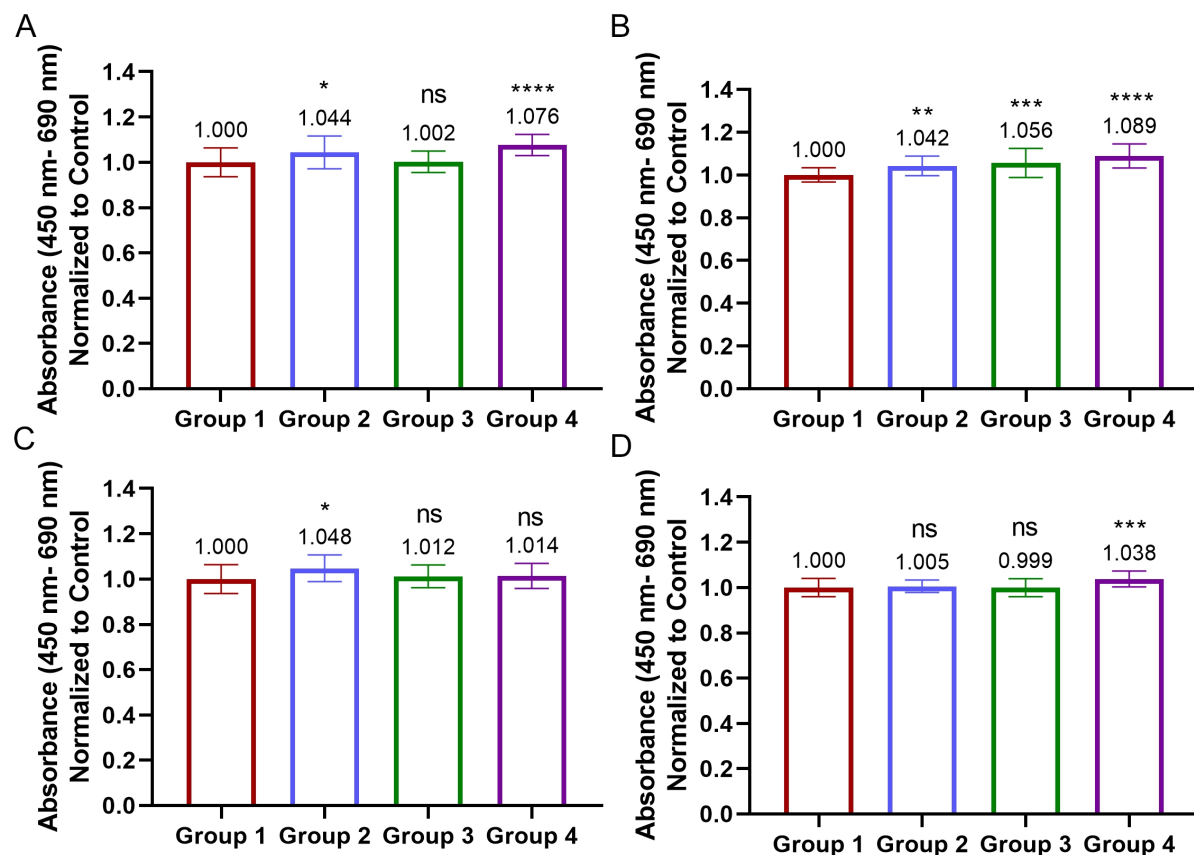


Figure 31. Normalized absorbances measured by XTT with three treatments: cell and medium irradiation followed by medium transfer in group 2, medium refreshment in group 3, simultaneous irradiation on cell and medium in group 4, and controls in group 1. A: 6 J/cm² BLI on HaCaTs. B and C: 4.5 and 6 J/cm² BLI on NHDFs. D: 6 J/cm² BLI on HUVECs. Values of absorbances were all normalized to controls without irradiation. Data are presented as mean \pm SD, and corresponding mean values are shown above error bars ($n = 3$ repetitions, *: $p < 0.05$, **: $p < 0.01$, ***: $p < 0.001$, ****: $p < 0.0001$, ns: not significant, one-way ANOVA: Dunnett's test).

3.4 Effects of BLI on ATP quantification

A low-fluence ($7.5 \text{ min} \times 10 \text{ mW/cm}^2$, 4.5 J/cm²) BLI increased ATP quantification for each cell type compared with controls, even though only a 2.2% rise was found in

HUVECs ($p > 0.05$). In terms of NHDFs, the ATP amount significantly increased by 5.4% after 4.5 J/cm² BLI ($p < 0.01$), while a fluence of 6 J/cm² (10 min \times 10 mW/cm²) did not significantly alter the ATP concentration of NHDFs. The normalized luminescence of HaCaTs and HUVECs that was proportional to ATP amount increased over time and reached 1.064 ($p < 0.0001$) and 1.033 ($p < 0.05$) after 6 J/cm² irradiation, respectively (Figure 32).

As a result, the fluence of 4.5 J/cm² BLI was determined for further assays on cell migration, apoptosis, and gene expression.

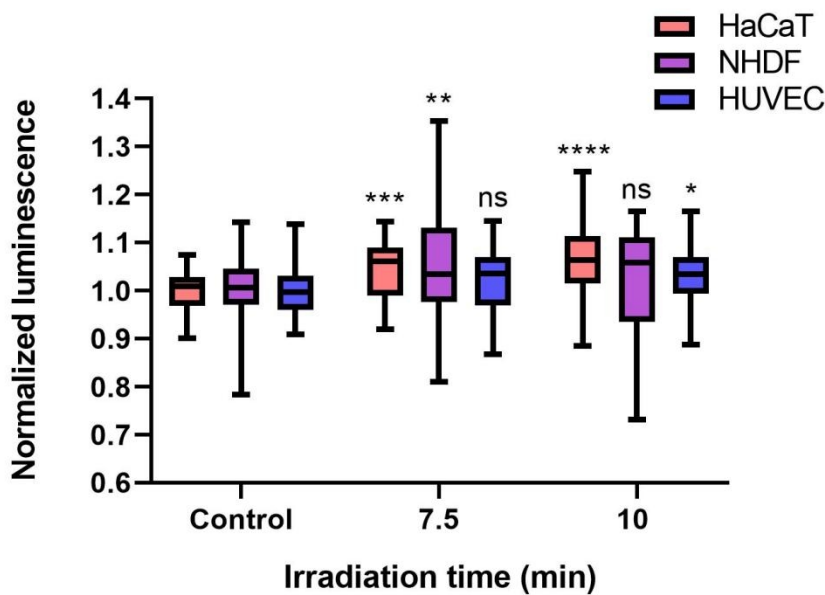


Figure 32. BLI altered ATP quantification of HaCaTs, NHDFs and HUVECs at two fluences (4.5 and 6 J/cm²). Data are shown as boxplots with medians, IQRs and error bars for outliers ($n = 3$ repetitions, *: $p < 0.05$, **: $p < 0.01$, ***: $p < 0.001$, ****: $p < 0.0001$, ns: not significant, one-way ANOVA: Dunnett's test). The luminescence was normalized to controls without irradiation.

3.5 Effects of the low-fluence irradiation (4.5 J/cm²) on cell migration

In comparison to controls, no significant difference in wound closure were observed in HaCaTs at any time points after irradiation ($p > 0.05$, Figure 33A). However, 6 h after 4.5 J/cm² BLI, NHDFs exhibited a significantly higher wound closure rate than controls ($p < 0.01$). Furthermore, as migration progressed in NHDFs, the difference values in wound closure continued to increased, from 5.8% at 6 h to 10.7% at 12 h (Figure 33B). In terms of HUVEC migration, a significant difference in wound closure was observed only at 12 h post-irradiation ($p < 0.0001$) (Figure 33C). Additionally, both NHDFs and HUVECs achieved complete wound closure within 24 h after irradiation (data not shown), whereas HaCaTs demonstrated substantially lower wound closure percentages than those values acquired in NHDFs and HUVECs 24 h

after irradiation, with values merely over 50% in both the control (51.93%) and irradiation groups (50.41%) (Figure 33A).

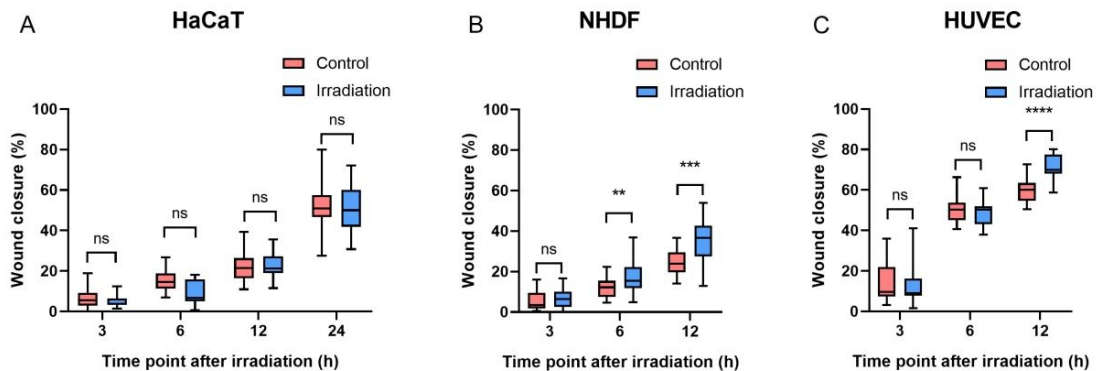


Figure 33. The levels of migration were quantified at different time points after BLI on three cell types (A: HaCaTs, B: NHDFs and C: HUVECs). Data are shown as boxplots with medians, IQRs and error bars for outliers. (n = 3 repetitions, **: p < 0.01, ***: p < 0.001, ****: p < 0.0001, ns: not significant, unpaired Student's t-test).

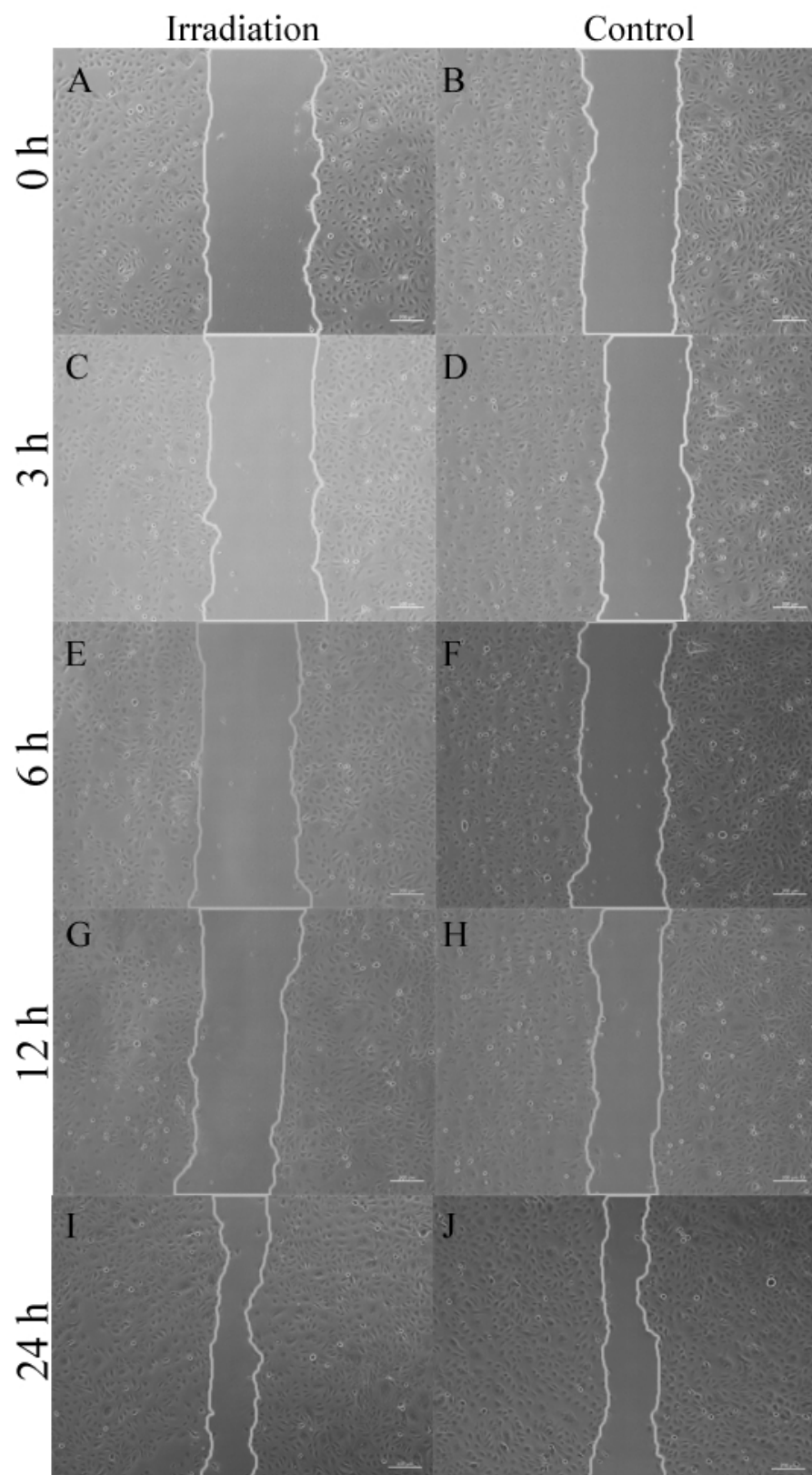


Figure 34. Representative images of the scratch assays of HaCaTs following exposure to 4.5 J/cm^2 at 0, 3, 6, 12, and 24 h after irradiation. All images have the identical scale bar of $200 \mu\text{m}$.

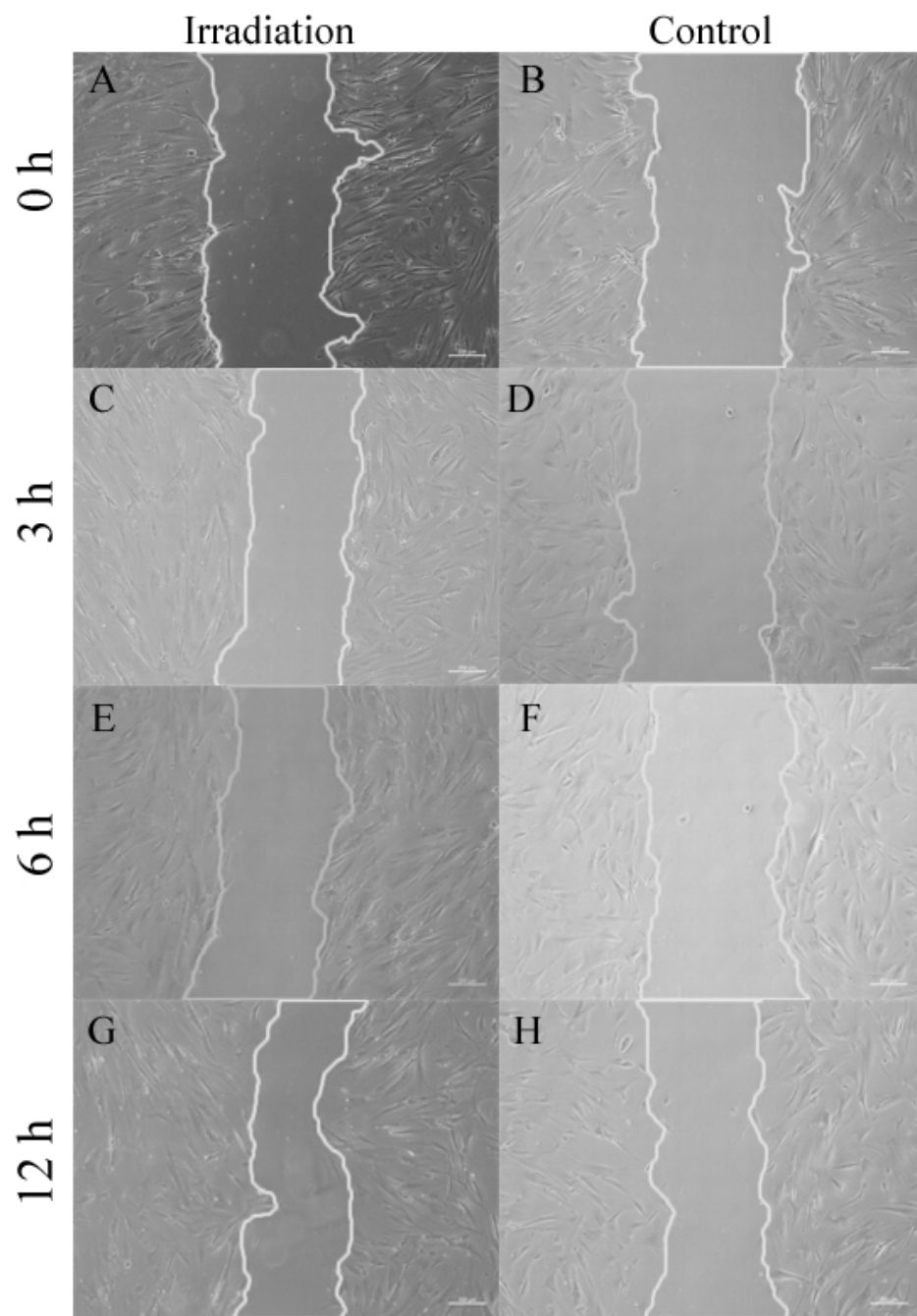


Figure 35. Representative images of migration assays in NHDFs after 4.5 J/cm^2 BLI. Images of wound closure were captured at 0, 3, 6, and 12 h after irradiation. The scale bar are $200 \mu\text{m}$ used for all images.

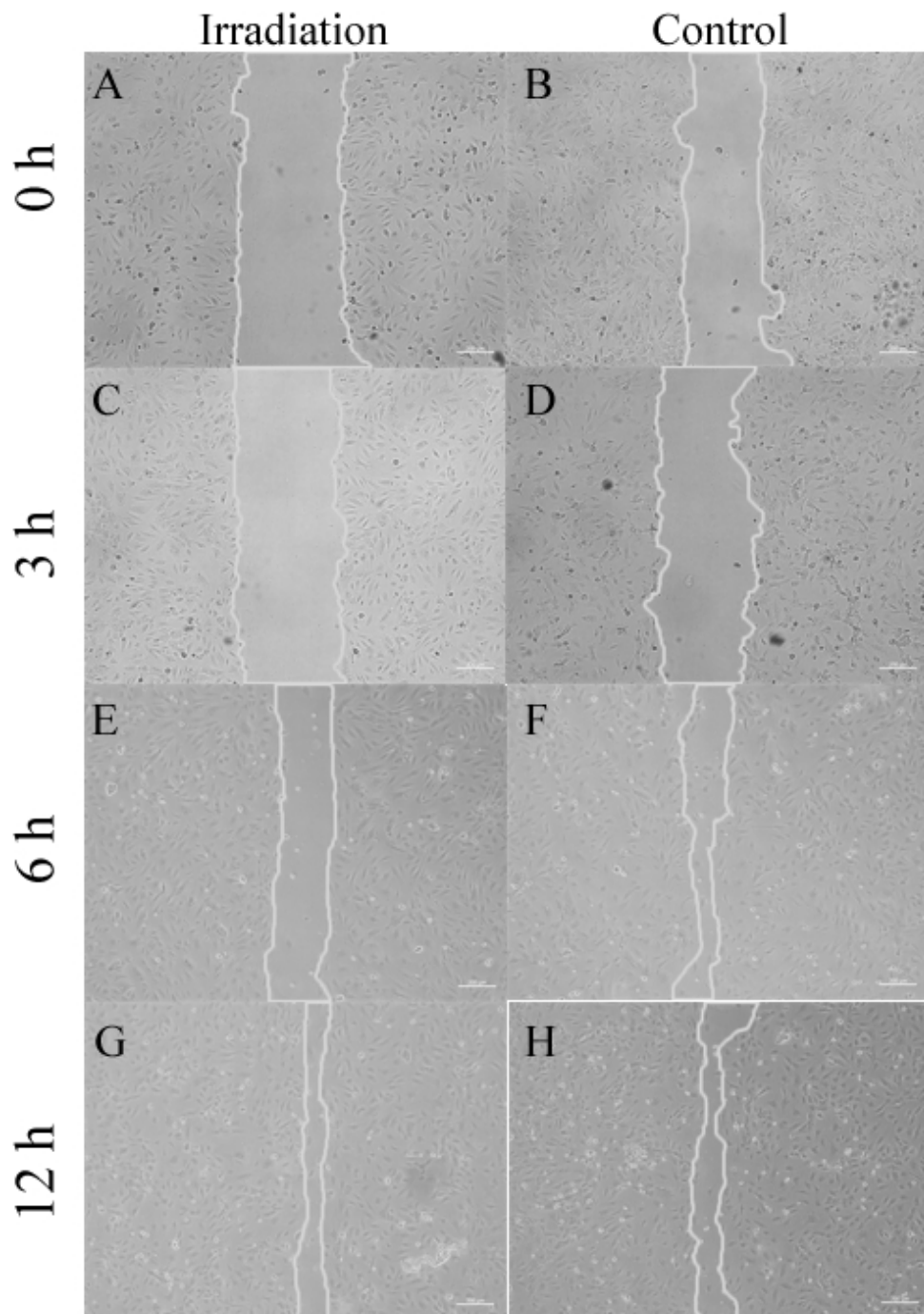


Figure 36. Representative images of HUVECs in migration assays after 4.5 J/cm^2 BLI, with the same scale bar at $200 \mu\text{m}$. The conditions of wound closure were observed by microscope at 0, 3, 6, and 12 h after irradiation.

3.6 Effect of 4.5 and 18 J/cm^2 BLI on cell apoptosis

Based on the findings from the previous kinetic assays, apoptosis assays after BLI at the specific fluences of 4.5 and 18 J/cm^2 were further designed by Annexin V/PI staining to evaluate the apoptotic status. Both Annexin V+/PI- and Annexin V+/PI+ populations were considered apoptotic. In Figure 37, apoptosis in the irradiation group (4.5 and 18 J/cm^2 BLI) was not significantly different from controls in HaCaTs,

NHDFs, and HUVECs. After sorting, only cells exposed to 1 μ M staurosporine for 24 h in the positive control group showed a significantly increased apoptotic level measured by flow cytometry after comparison with controls. Exemplary results of Annexin V/PI staining after sorting were shown in Figure 38.

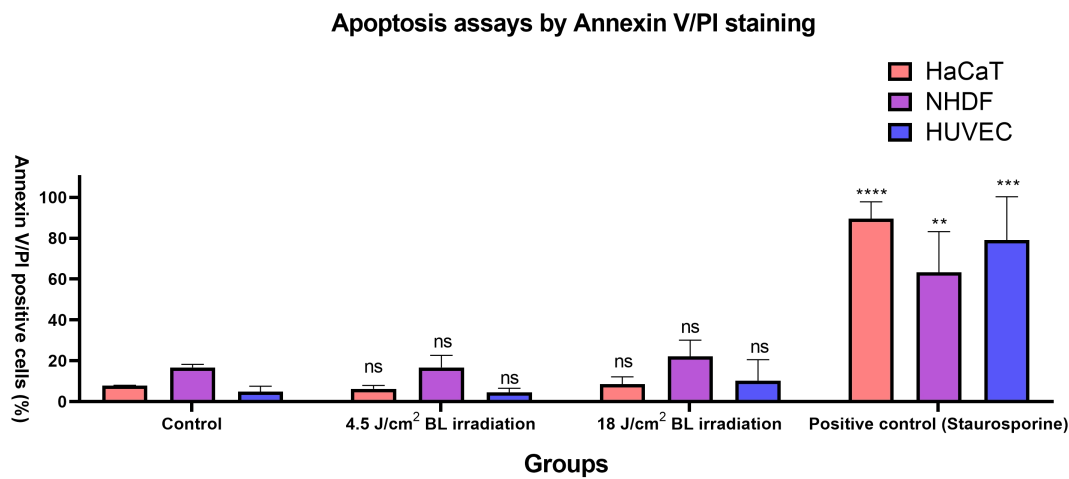


Figure 37. The populations of apoptotic cells quantified by Annexin V/PI staining among groups of 4.5 and 18 J/cm^2 irradiation, 1 μM staurosporine (positive controls) and untreated controls. Data are shown as column bar with mean \pm SD. (n = 3 repetitions, **: p < 0.01, ***: p < 0.001, ****: p < 0.0001, ns: not significant, one-way ANOVA: Dunnett's test).

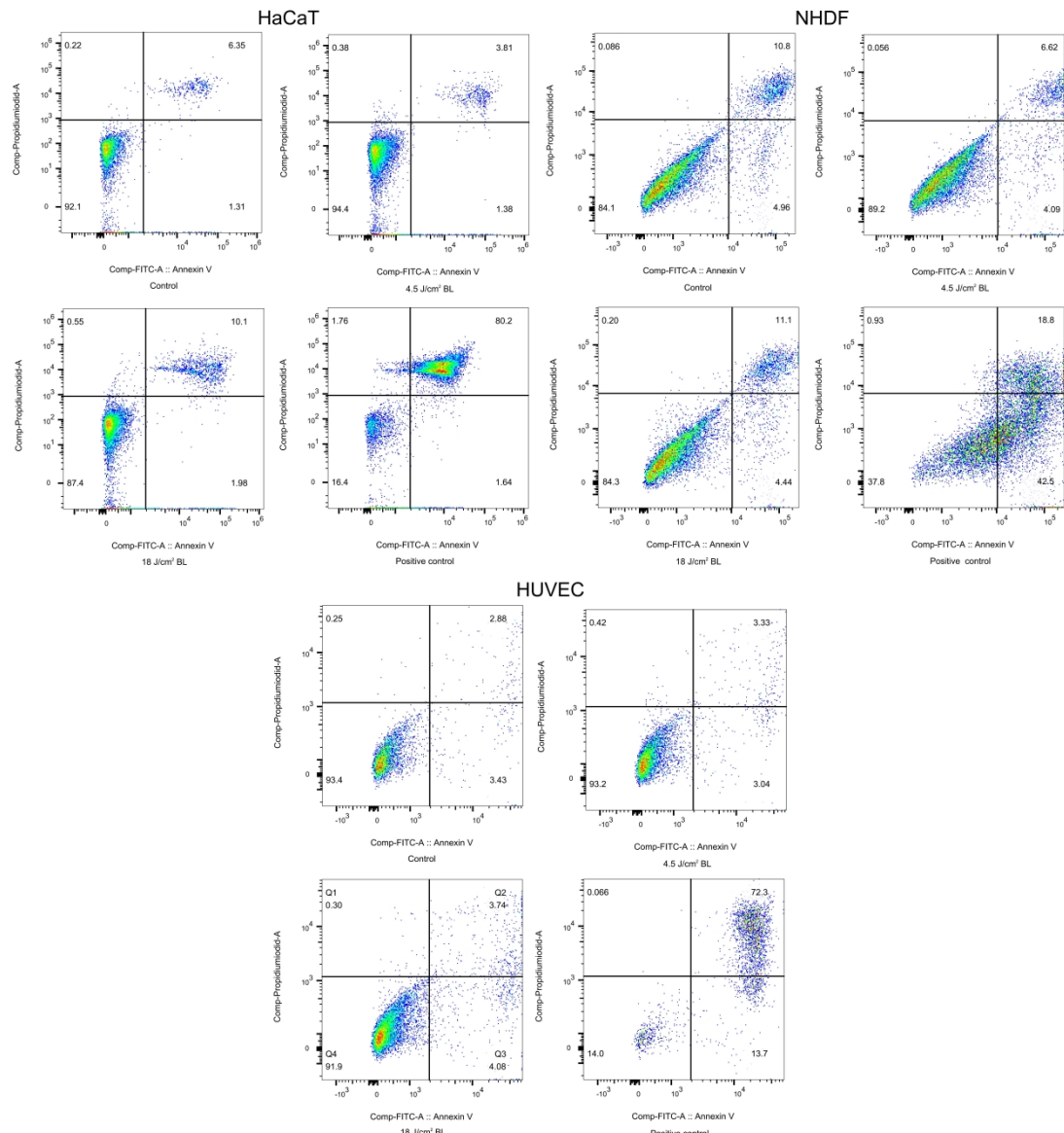


Figure 38. Exemplary results of Annexin V/PI staining on three cell types, with three treatments: 4.5 J/cm², 18 J/cm² irradiation, 1 μM staurosporine (positive controls) and controls.

3.7 Gene expression analysis after RNA sequencing

Following an overall assessment of cellular responses after different doses of BLI, two fluences of 4.5 and 18 J/cm² were selected to explore the impacts of light treatments on gene expression. Since NHDFs play a profound role in signaling cascades, interact with keratinocytes and endothelial cells throughout phases of wound healing and angiogenesis, we decided to move forward with RNA sequencing using NHDFs. The correlation heatmap (Figure 39) showed excellent reliability and repeatability with distinct clusters. After differential expression analysis, 291 out of 621 genes were upregulated compared to controls after 4.5 J/cm² (Figure 40). The expressions of genes were reported to regulate cellular viability, motility, and

proliferation, such as MET, EREG, and MEMO1, were significantly increased. Two collagen genes, COL5A3 and COL8A1, were also significantly up-regulated. When the energy density increased to 18 J/cm², 1376 genes were upregulated, which was more than 1265 down-regulated genes in the 18 J/cm² BLI groups (Figure 40). After gene set enrichment analysis (GSEA), only pathways from the KEGG database that met the following thresholds: FDR < 0.25, nominal p-value < 0.05, and |normalized enrichment score (NES)| > 1 were considered to be enriched significantly. ErbB pathway (NES = 1.62), TGF-β pathway (NES = 1.58), and VEGF pathway (NES = 1.43) were enriched after 4.5 J/cm² irradiation (Figure 41A, B, and C). After 18 J/cm² irradiation, the down-regulated genes were enriched in DNA replication (NES = -2.29), cell cycle (NES = -1.94), and mismatch repair (NES = -1.72) (Figure 41D, E, and F).

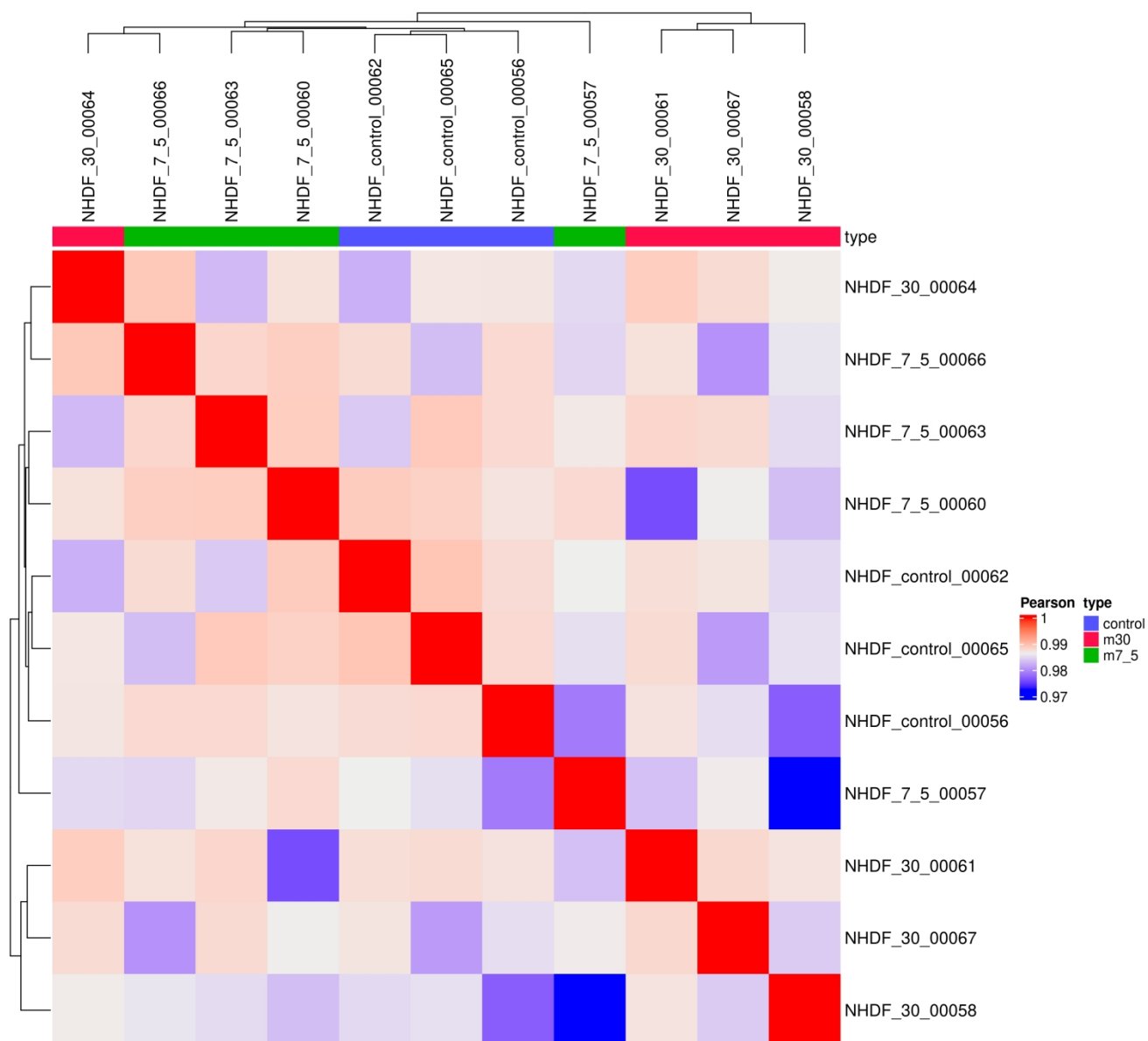


Figure 39. The correlation heatmap showing correlation coefficient of sample between groups (controls, 4.5 J/cm² BLI and 18 J/cm² BLI).

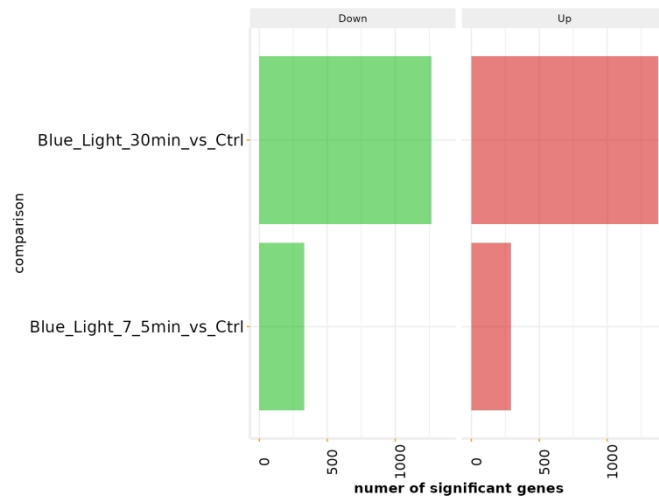


Figure 40. The number of differential expression genes after the differential expression analysis.

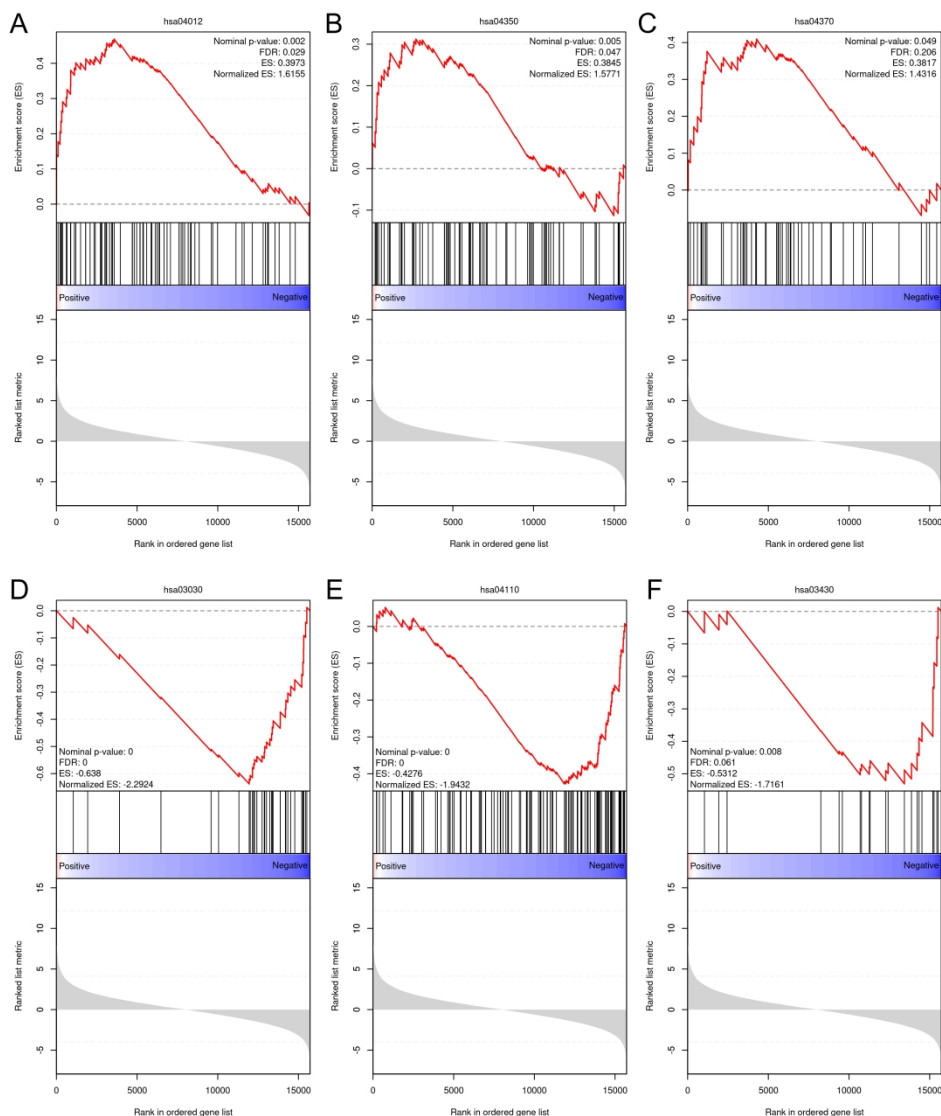


Figure 41. GSEA plots of the up-regulated and down-regulated gene set enriched in different pathways from the KEGG database. A: ErbB signaling pathway (hsa04012); B: TGF-β signaling

pathway (hsa04350); C: VEGF signaling pathway (hsa04370); D: DNA replication (hsa03030); E: cell cycle (hsa04110); F: mismatch repair (hsa03430).

Furthermore, Gene Ontology (GO) term enrichment analysis was applied. The ridge plot in Figure 42A shows the enrichment in the GO biological process (BP) category through GSEA. The up-regulated genes were significantly enriched in wound healing (GO:0042060) after 4.5 J/cm² BLI. Figure 42B indicates down-regulated genes were enriched in several processes of mitosis, including mitotic sister chromatid segregation (GO:0000070), chromosome segregation (GO:0007059), and nuclear division (GO:0000280) after 18 J/cm² irradiation ($p.\text{adjust} < 0.0001$).

Meanwhile, additional GSEA was conducted based on the Reactome database to provide more information on pathway enrichment. Figure 43A suggests 4.5 J/cm² BLI upregulated genes involved in translation, while 18 J/cm² BLI downregulated genes in the pathway of mRNA splicing (Figure 43B).

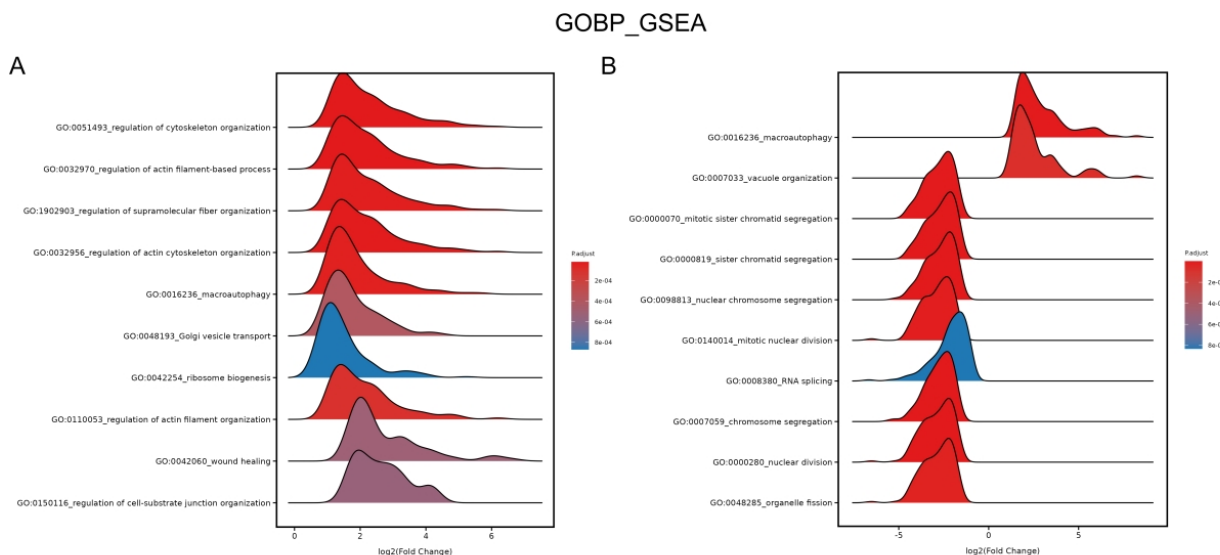


Figure 42. Ridge plots of enrichment in GO BP after 4.5 J/cm² (A) and 18 J/cm² (B) BLI on NHDFs. Plots show the enriched GO terms, p values and \log_2 (fold change) values.

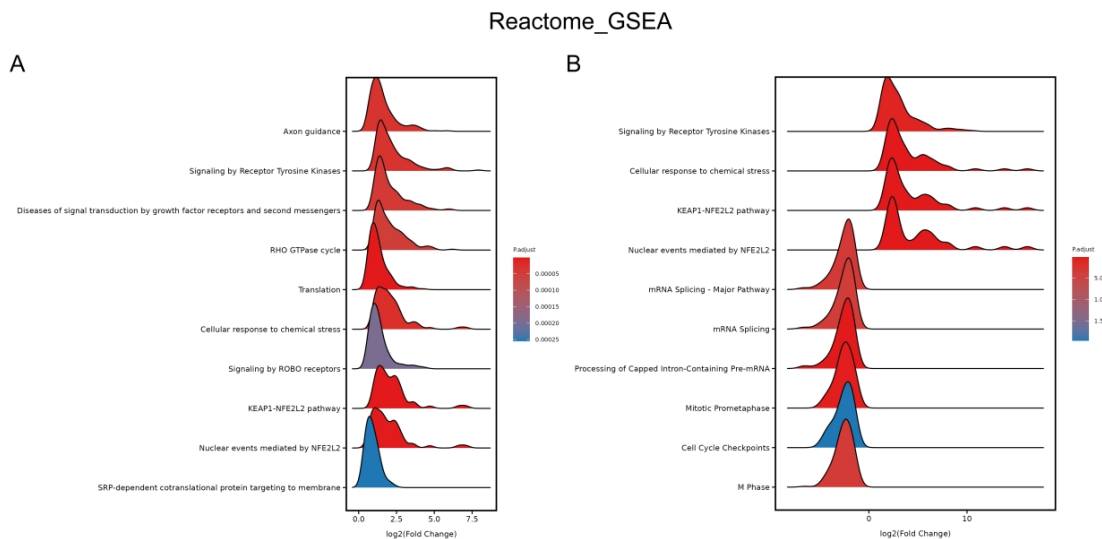


Figure 43. Ridge plots of enrichment from the Reactome database after 4.5 J/cm^2 (A) and 18 J/cm^2 (B) BLI on NHDFs. Plots show the enriched pathways, p values and \log_2 (fold change) values.

Two PPI networks were constructed based on data from the STRING database. We selected an interaction score > 0.15 to construct a network for the low fluence (4.5 J/cm^2) group and an interaction score > 0.7 for the high fluence (18 J/cm^2) group. In Figure 44, the PPI network contained 87 nodes representing the differentially expressed genes. MET achieved the highest degree, ranking No. 1 by the maximal clique centrality (MCC) method in CytoHubba. MET had a much higher score than the second gene of TXNRD1 (157 in MET vs. 91 in TXNRD1) after the calculation. As a result, MET was identified as a hub gene containing 24 connections with other genes in this network.

In terms of the high fluence irradiation on NHDFs, there were up to 498 nodes in the network (Figure 45). Among those differentially expressed genes, CDC20 ranked first, followed by AURKB, CCNB1, CCNB2, PLK1, CDCA3, TPX2, PTTG1, and SPAG5 after calculation. All these genes had scores exceeding 41000, indicating that they were hub genes in the high-fluence group. TP53 had the highest node degree of 64, which indicated the broad connections between TP53 and other differentially expressed genes after 18 J/cm^2 irradiation.

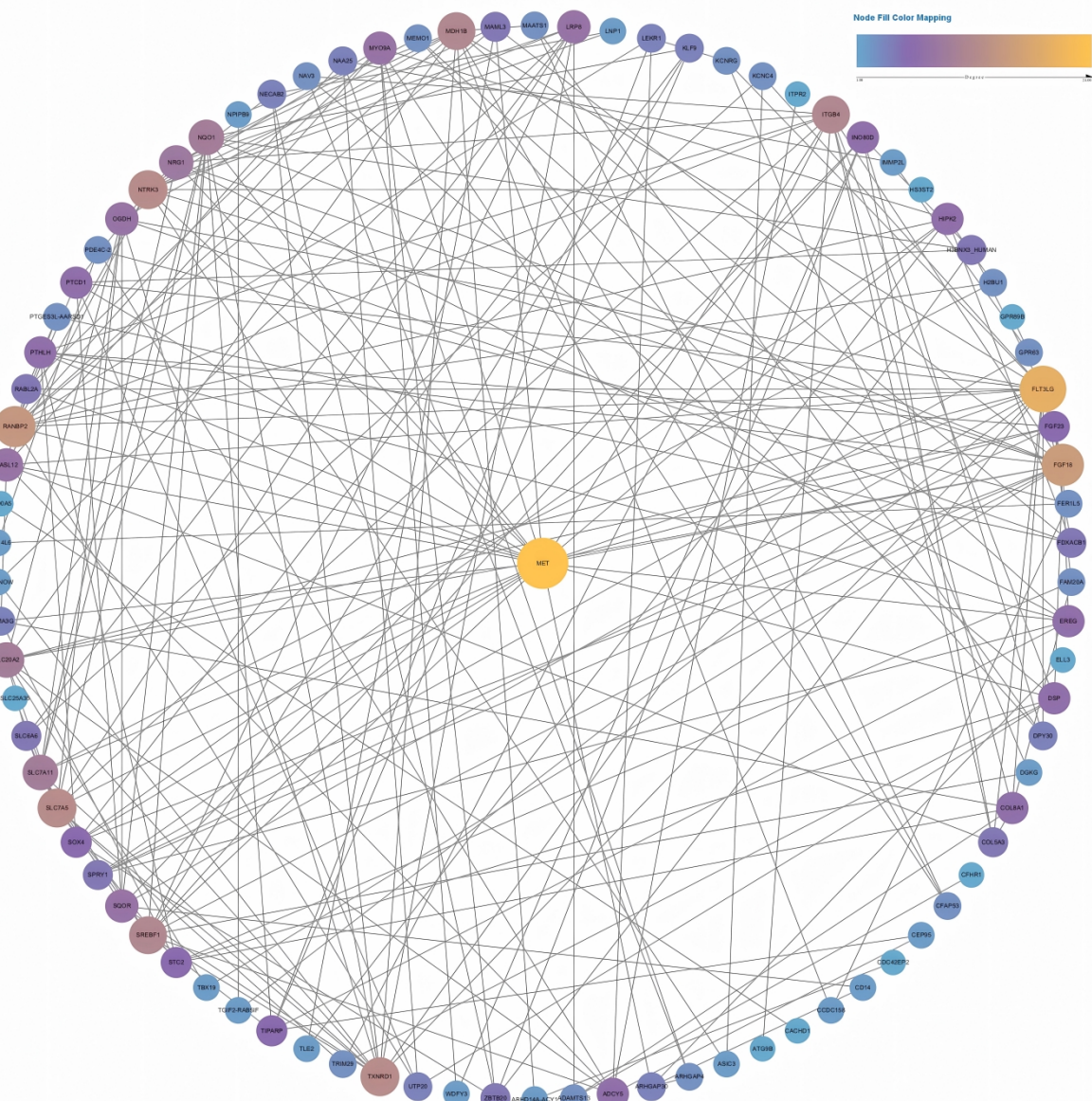


Figure 44. The PPI network of differentially expressed genes in the low fluence (4.5 J/cm^2 BLI) irradiation group. The size and color of nodes indicate node degree.

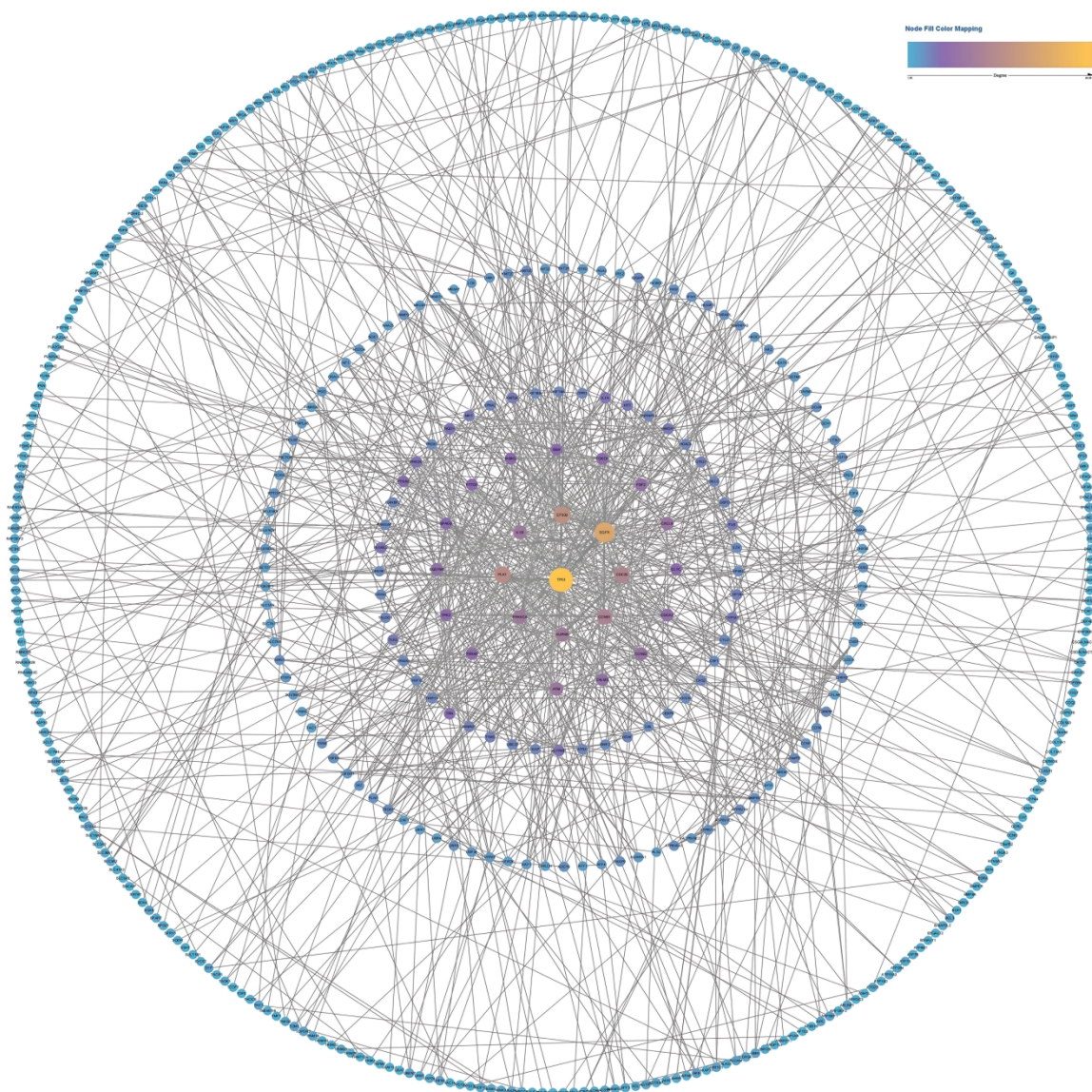


Figure 45. The PPI network containing all nodes (differential expression genes) in the high fluence (18J/cm^2 BLI) irradiation group. The size and color of nodes indicate node degree.

4 DISCUSSION

4.1 Influence of BLI on cell lines of HaCaT, NHDF and HUVEC

Our study primarily investigated on the PBM after a relatively low fluence BLI at the wavelength of 450 nm on three cell lines: HaCaTs, NHDFs, and HUVECs, which exert extensive and essential roles in processes of wound healing and angiogenesis. Firstly, we observed clear dose-dependent biphasic effects by combining findings of cell viability and proliferation across a range of irradiation doses. Secondly, most kinetic assays, including cell viability, proliferation, ATP quantification, and migration, found that a low-fluence irradiation at 4.5 J/cm² stimulated the cellular activities in all three cell lines. Thirdly, cells behaved cell-type-dependently after BLI, and obviously different cellular responses were observed and measured by the aforementioned kinetic assays. Notably, irradiation at 4.5 and 18 J/cm² did not incur an increased level of cell apoptosis.

In terms of long-term irradiation, cellular responses also differed after long-term BLI, again indicating the existence of cell-type-dependent responses to BLI. Following the long-time irradiation (2 h irradiation with an irradiance of 23 mW/cm²) and the promotive irradiation with a fluence of 4.5 J/cm², the sequential light treatments verified that the 4.5 J/cm² radiation boosted cell activities, which were confirmed by cell viability and ATP concentration. Extending the exposure time up to 5 h clearly and simultaneously showed the dose- and cell-type-dependent effects on cell lines. Additionally, different treatment protocols, such as medium irradiation and medium refreshment, potentially had influence on cell viability, although there were no measurable interaction or the interaction between BLI and phenol red had no influence on cell viability measured under our irradiation setup.

Finally, RNA sequencing and subsequent bioinformatic analysis revealed the mechanism of PBM following 4.5 J/cm² BLI and the inhibitory effect of light treatment after 18 J/cm² BLI. 4.5 J/cm² BLI activated signaling pathways of ErbB, TGF- β , and VEGF, while 18 J/cm² BLI primarily inhibited cell activity by DNA replication, cell cycle, and mismatch repair.

4.2 Experimental settings of temperature measurements

The irradiances of 10, 23, and 40 mW/cm² were selected based in part on the experimental objectives of the blue light prototype from URG, and the biological

influences of temperature during irradiation were also taken into account. Such experimental settings of temperature measurement are also consistent with our previous research ¹²¹. Similarly, RT was measured and recorded during the pre-run for 15 min until the stabilization of real-time values, which provided a baseline for the subsequent temperature measurements with different irradiation doses and facilitated further comparisons of temperatures. Usually, in the lab, the temperature varies within a narrow range between 18 and 22°C, which is consistent with the data presented in Figure 19. The medium-filled plate underwent a pre-warming process in the incubator at 37°C, leading to a sharp rise when sensors reached the positions depicted in Figure 14. We preferred a comprehensive understanding of the temperature variation at different positions on a 96-well black plate, although measuring temperature at only three positions still provided limited information.

In the 10 and 23 mW/cm² groups, all temperatures measured by the thermocouple were no more than 37.5°C, which was close to human body temperature. In the case of 40 mW/cm² (as depicted in figure 19C), the temperature rapidly escalated and ultimately reached a peak of over 45°C. This temperature is clearly higher than the average body temperature and is not suitable for in vitro cell culture. Under this condition, protein denaturation can occur, resulting in irreversible damage to cell integrity ¹²². Pan et al. reported morphological changes in the cytoskeleton and stagnation at G0/G1 cell cycle stages after 1 h of heat stress at 43°C ¹²³. Even though Reissis Y et al. reported that exposure under 48°C for 2 to 3 min might not affect the cell function and viability of human mesenchymal stem cells ¹²⁴, we could not predict or ignore the potential effects of heat stress on HaCaTs, NHDFs and HUVECs. In our study, we aimed at assessing cellular responses under BLI in various time frames. Therefore, we conducted our study using lower power densities of 10 and 23 mW/cm².

4.3 New LED-based BLI prototype

Unlike the previous irradiation mode, which used the LED light source from the MEDILIGHT system and BioLight LED lamp, our new LED-based BLI prototype utilized the light source beneath the cell culture plate. This configuration addresses two major disadvantages of the previous setup: Firstly, due to the absorption spectrum of black plates, energy losses are inevitable once light is emitted above plates, reaching around 85% (provided by URG0). Furthermore, if desired power densities are maintained on the cell layer, a much higher current should be pumped

by the driver to compensate for such energy losses. The high energy from light source subsequently can lead to overheating on both LEDs and plates in the case of illumination on the top. Eventually, the detrimental effects derived from critical heating can result in destructive consequences on cells. Secondly, other confounding factors from the medium (color, pH, etc.) can potentially influence cellular responses during visible light penetrating culture medium from the surface to the layer of cells.

Based on the new illumination system, the photodiode directly measured light intensity immediately after photons penetrated through the plate bottom, which minimize further light loss during the propagation and accurately reflected the light intensity on cells. Compared with the previous experimental settings of light intensity measurement on the MEDILIGHT system, the BioLight LED lamp and the 843-R laser power meter (Newport Corporation, Irvine, CA, USA), more accurate data on light distribution were obtained and used for further assessments by our new LED-based BLI prototype and photodiode-based device.

Additionally, the reflective box can ensure the emission of homogeneous blue light at the wavelength of 450 nm. Evidently, there are some improvements on experimental designs compared to the old irradiation settings. As shown in Figures 6 and 10, thanks to the sealed reflective box and 96-well black plates, disturbance of ambient light can be effectively minimized.

All aforementioned technical advances in irradiation ensure optimal cell culture conditions, and further improve the accuracy of measurement on cellular performance after BLI.

4.4 PBM after BLI on HaCaTs

This study assessed cell viability, proliferation, migration, ATP quantification, and apoptosis in HaCaTs. We proved that fluences of 4.5 and 6 J/cm² can increase the level of cell viability with an irradiance of 10 mW/cm² through the process of PBM. ATP quantification consistently revealed a promotive effect at 4.5 and 6 J/cm² BLI, indicating an increased level of metabolic activity. The similar responses of both cell viability and ATP concentration were probably attributed to activation of the electron transportation chain on functional mitochondria after irradiation, leading to more reduction of tetrazolium dye and increased ATP synthesis via ATP synthase (Figure 5). In contrast, neither cell proliferation nor migration of HaCaTs showed any significant biostimulation effects. In terms of cell viability, Wataha et al. observed a 30% increase in succinate dehydrogenase (SDH) activity in human diploid foreskin

keratinocytes after exposure to a 5 J/cm^2 laser with a wavelength between 400 and 500 nm, in comparison to no-light controls ¹²⁵, which is similar to our findings of biostimulation measured by XTT. Castellano-Pellicena et al. also performed multiple assays to measure metabolic activities, DNA synthesis, and migration after 2 and 30 J/cm^2 BLI ⁹⁹. In terms of migration, 2 J/cm^2 BLI did not stimulate or accelerate the process of cell migration, which aligned with our findings at a low-fluence irradiation (4.5 J/cm^2). However, there was still a noticeable conclusion different from our finding in DNA synthesis: 2 J/cm^2 BLI significantly reduced EdU incorporation, showing that it had inhibitory effects on cell proliferation. Consistently, Fushimi et al. used BLI (456 nm) at a low level of 0.3 J/cm^2 on HaCaTs, showing that the migration rate remained unchanged after this low-dose light exposure ¹²⁶. Additionally, wavelength-dependent cellular behaviors were observed with visible light at different wavelengths ¹²⁶. Although relatively low doses of BLI were applied to keratinocytes from all these researches, the objective existence of heterogeneity of irradiation setups, including parameters, light source dimensions, and other underlying factors involving differences in cell culture environments and cell types, could result in the discrepancy of conclusions. Moreover, the inconsistency of cell viability and proliferation has been widely reported, with miscorrelation between metabolic activities and DNA contents ^{127, 128}. This accounts for the inconsistent findings observed in XTT and BrdU assays.

4.5 PBM after BLI on NHDF

Based on the previous irradiation parameters of the BioLight LED lamp and MEDILIGHT system, including the wavelength, irradiance, etc ¹²⁹, exploration of metabolism, proliferation, and migration of NHDFs by analogous experimental methods were designed after BLI via the new LED-based prototype. Furthermore, the mechanism revealed by RNA sequencing and bioinformatic analysis in our in vitro study provides an experimental basis for future clinical application of PBM.

The emitted 450 nm blue light from our LED-based prototype significantly stimulated cell viability, proliferation, and migration after 4.5 J/cm^2 BLI on NHDFs. The following transcriptome analysis indicated that PBM after 4.5 J/cm^2 BLI increased the expression of genes related to ErbB, TGF- β , and VEGF pathways. Meanwhile, MET, MEMO1, EREG, COL8A1, and COL5A3 were also found to be upregulated, which were involved in the modulation of versatile cellular functions related to cell viability, motility, proliferation, and collagen biosynthesis. Mason-Meyers et al. reported that

doses (3, 5, 10, and 55 J/cm²) of BLI stimulated protein synthesis ¹³⁰. Meanwhile, the clear biphasic effect was observed on the wound closure rate: 55 J/cm² BLI inhibited cell migration, whereas 5 J/cm² BLI induced intense cell migration. A study conducted by Mignon et al. also found that metabolic activities of reticular and papillary fibroblasts increased after a low dose (2 J/cm²) compared to non-irradiated controls. As the doses increased to 30 J/cm², the stimulation of reticular fibroblasts remained, while the metabolism of papillary fibroblasts declined ¹³¹. Zhang et al. performed cell migration assays using human skin fibroblasts that had been exposed to 3 J/cm² BLI, showing that the 465 nm wavelength radiation promoted cell migration ¹³². Our in vitro experiments not only consistently showed that continuous irradiation mode at the wavelength of 450 nm stimulated fibroblasts in a favorable manner, but also provided evidence of gene expression after 4.5 J/cm² BLI on NHDFs, along with pathways on modulation in wound healing and angiogenesis after PBM.

RNA sequencing following the low-fluence at 4.5 J/cm² irradiation indicated mechanisms related to PBM. By the bioinformatic analysis, both the up-regulated and down-regulated genes and pathways were clearly identified. The ErbB signaling pathway encompasses various steps through interaction with signal transducers, which facilitates autophosphorylation and downstream signaling cascades. It modulates cell proliferation, migration, differentiation, apoptosis, and motility via the PI3K/AKT, JAK/STAT, and MAPK pathways. Jere et al. reported that 5 J/cm² 660 nm irradiation promotes PBM on fibroblasts by EGF, and the JAK/STAT pathway activated cell proliferation and migration ¹³³. Karoussis et al. reported that 12 J/cm² (810 nm) low-level-laser therapy promoted gingival fibroblast proliferation by expression of EGF ¹³⁴. In our study, enrichment analysis suggested that 450 nm BLI upregulated the expression of epiregulin (EREG) and the ErbB pathway. By the increased interactions with the EGFR, downstream responses of cell viability and proliferation were promoted. Moreover, upregulation of MEMO1, a molecule originally associated with the ErbB2 receptor, was found to have an essential role in effective cell migration upon interactions with receptors ¹³⁵. TGF- β contributed to the process of wound healing by attenuating inflammation, stimulating angiogenesis, activating fibroblasts, collagen biosynthesis and deposition, and ECM remodeling ¹³⁶. Both the PI3K/AKT and JAK/STAT signaling pathways could be activated by TGF- β , resulting in downstream responses related to metabolism, growth, and proliferation ¹³⁷. Mignon et al. reported the inhibitory effect after BLI and specifically pointed out the

downregulation of TGFB2 in two subpopulations of fibroblasts after a dose of 30 J/cm² irradiation ¹³⁸. There is consensus that the up-regulated VEGF pathway plays an essential role in angiogenesis, and vessel formation appears to be a series of highly complicated and coordinated processes with the involvement of multiple regulation mechanisms ¹³⁹⁻¹⁴¹. In our study, results of enrichment analysis provided evidence that activated fibroblasts were involved in angiogenesis by the VEGF pathway after 450 nm BLI. A similar conclusion was discovered by Karoussis et al., who proved upregulated gene expression of VEGF by qPCR after energy density of 12 J/cm² irradiation on gingival fibroblasts, although the existence of cell-type differences ¹³⁴. Besides the conclusion from the enrichment analysis, by differential expression analysis, we also found 4.5 J/cm² irradiation induced significant upregulation of MET. Furthermore, the bioinformatic analysis of the PPI network depicted the interaction of the differentially expressed genes and emphasized the pivotal role of MET in PBM. HGF/c-MET signaling was proved to be involved in cutaneous wound healing ^{142, 143}. Yoshida et al. found that local and continuous delivery of anti-HGF to subcutaneous lesions inhibited the growth of vessels and expansion of granulation tissue, indicating that the upregulation of c-MET expression in granulation tissue benefited neovascularization and granulation tissue formation ¹⁴⁴. Other highly expressed genes, such as COL5A3 and COL8A1, demonstrated a positive impact on collagen biosynthesis following a 4.5 J/cm² BLI. The product of collagen V is a form of fibrillar collagen with functions of structural integrity and tissue support. Moreover, it participated in the modulation of cellular behaviors and functions ¹⁴⁵. As a non-fibrillar and short-chain collagen, collagen VIII engaged in vascular remodeling by regulating the migration, proliferation, and adhesion of vascular smooth muscle cells ¹⁴⁶.

4.6 PBM after BLI on HUVEC

Even though the theoretical basis and our experiment results supported that BLI had a profound influence on endothelial cells, promoting angiogenesis and wound healing, there was limited literature reporting PBM using visible light in the blue spectrum. Rohringer et al. observed a trend of increased proliferation 72 h post-irradiation with a fluence of 24 J/cm² on HUVECs, and opposite trends were obtained, with a significant decrease in assays of cell metabolic activity ¹⁴⁷. Dungel et al. used 30 J/cm² BLI at 470 nm on a model of rat skin flaps and reported increased blood

vessels, which was a sign of pro-angiogenic effects¹⁴⁸. Our study of PBM following irradiation on HUVECs was designed based on the previous configuration of the MEDILIGHT system, with distinct heterogeneities in irradiation mode and culture conditions during irradiation: First, in our study, all HUVECs were exposed to continuous BLI, whereas the MEDILIGHT system employed a pulsed irradiation mode (30 seconds on and 30 seconds off). Secondly, light sources in our study were positioned beneath the plate. On the contrary, LEDs in the MEDILIGHT system were attached to the lid. The difference in the positions of LEDs rendered light propagated with opposite directions. Thirdly, LEDs in the MEDILIGHT system were powered by a rechargeable battery, which aimed at meeting the requirements of in-home application. In this study, LEDs powered by alternating current meant more stable light intensities were obtained by cells, and the stabilization of energy supplies benefited the long-term irradiation.

In HUVECs, the biostimulation effect after light treatments with an irradiance of 10 mW/cm² induced a peak in cell viability with a fluence of 6 J/cm². However, when comparing the normalized values of the other cell lines (HaCaT and NHDF), we found that 4.5 J/cm² BLI primarily facilitated both cell viability and proliferation of NHDFs and HaCaTs after the exposure time of 7.5 min instead of 10 min. This minor difference in the optional irradiation setting partially results from cell-type specificities. Therefore, to select an irradiation parameter that generates a common biostimulation suitable for all cell lines, compromises should be made regarding the selection of optimal fluence in HUVECs. Surprisingly, following a 4.5 J/cm² dose of BLI, positive effects on cell viability and proliferation after the light treatment were still obtained, which confirmed the retained effectiveness of 4.5 J/cm² BLI on PBM for all cell lines. To sum up, the 450 nm BLI effectively promoted responses of HUVECs in terms of metabolism, proliferation, migration, without incurring apoptosis-related consequence after the low-fluence (4.5 J/cm²) irradiation.

4.7 The inhibitory effect after BLI on cell lines

Since the introduction of the "Arndt-Schulz Law" in 1887, more and more studies in the fields of PBM, both in vitro and in vivo, have extensively documented the biphasic effect. Three cell lines in our study obviously experienced inhibitions in cell viability and proliferation once excessive energy was generated and imposed on cells after extending blue light exposure. Usually over 30 min of irradiation, regardless of irradiance, the inhibitory effect presented in a clear pattern. After the irradiation time

extended over 2 h, the gradually increased inhibition resulted in cytotoxicity and finally led to cell death, as demonstrated by the subsequent measurements of cell viability. XTT assays showed that only HaCaTs had a marginal increase in cell viability after 5 h of exposure to 23 mW/cm² irradiation. The difference was partly attributed to cell-type difference: HaCaT is an immortalized cell type, whereas the other two cells in our study are primary cell lines. Furthermore, when referring to results of sequential light treatment in Section 3.3.3.1 and long-time irradiation in Section 3.3.2, we found that cytotoxicity after 5 h of irradiation with the irradiance of 23 mW/cm² caused irreversible damage, especially to NHDFs and HUVECs. Undoubtedly, the great inhibitions after long-term irradiation influenced not only metabolic activity but also the survival of cell lines and clearly indicated the potential application in clinical practice. However, when light exposure was shortened to 2 h with the irradiance of 23 mW/cm², normalized values reflecting cell viability gradually increased, suggesting cell viability tended to recover after 2 h irradiation. Moreover, this recover trend was further enhanced following 4.5 J/cm² BLI at irradiance of 10 mW/cm². Our sequential light treatments after BLI demonstrate inhibitory or even mortal influences on cell lines after long-term irradiation (2 and 5 h) and confirmed the stimulatory effects after 4.5 J/cm² irradiation.

Researchers have widely reported the effectiveness of antimicrobial blue light (aBL) as a therapeutic approach against multidrug-resistant bacterial strains due to its broad-spectrum antibacterial capability. On gram-negative pathogens, Wang et al. investigated the inactivation of *Acinetobacter baumannii* and *Pseudomonas aeruginosa* after 432 J/cm² light treatment and proved the effectiveness of aBL¹⁴⁹. Then, in mouse burn models, fluences of 360 and 540 J/cm² were added to demonstrate the inactivation of *A. baumannii* after blue light treatments¹⁴⁹. Angarano et al. applied an array of visual lights at wavelengths ranging from 400 to 698 nm to both gram-positive (*Staphylococcus epidermidis*) and gram-negative bacteria (*Pseudomonas fluorescens*), concluding that light at a wavelength of 400 nm successfully inactivated *P. fluorescens* and *S. epidermidis*, with fluence varying from 10.1 to 420.5 J/cm²¹⁵⁰. However, the inactivation attenuated once the wavelength increased to 420 nm, influencing only *P. fluorescens* with a fluence of 6.9 J/cm². Additionally, in vitro and in vivo studies conducted by Leanse et al. revealed no evidence of aBL resistance following the sequential aBL treatment of gram-negative bacteria¹⁵¹.

In terms of cell lines, Avola et al. found that cell viability changed depending on the dose of BLI. The inhibitory effect of BLI caused cell viability to decrease and drop to a level of 23% after 85 J/cm^2 of irradiation ¹⁵². Mamalis et al. reported dose-dependent responses of proliferation, migration speed, and ROS, indicating that with an increase in fluence, a corresponding inhibitory effect occurred ¹⁵³. After irradiating fibroblasts at 3, 55, 110, and 220 J/cm^2 BLI at a wavelength of 470 nm, Masson-Meyers et al. assessed toxicity, observing that cell viability varied depending on the methods used (MTT, neutral red, trypan blue, and live/dead fluorescence) after 470 nm BLI ¹⁵⁴. Likewise, as the doses of BLI increased on fibroblasts, cytotoxicity gradually became apparent in our study. Evidently, the aforementioned literature provided evidence that overexposure to BLI led to adverse effects on various cell types. However, most reports mainly focused on the downstream cellular responses, lacking mechanistic investigation. In our study, by RNA sequencing and the following bioinformatic analysis, 18 J/cm^2 BLI predominantly inhibited pathways of DNA replication, cell cycle, and mismatch repair, with significant downregulation of mitosis-related genes (CDC20, AURKB, CCNB1, PLK1, CDCA3, TPX2, PTTG1, and SPAG5) and the gene correlated to the cell cycle (CCNB2). The changes at gene level led to the occurrence of a corresponding negative effect on cell viability and proliferation. Similarly, Mignon et al. reported downregulated genes (CDC20, PLK1) of the cell cycle pathway in reticular and papillary fibroblasts following 2 and 30 J/cm^2 BLI. Additionally, the gene of COL8A1 related to collagen biosynthesis was also found to be differently expressed ¹³⁸.

4.8 The influence from cell culture condition and treatment protocol

According to the study by Mignon et al. ¹⁵⁵, which showed the variations in metabolic activities under various conditions (treatment protocols), such as serum concentration, medium refreshment, confluence, etc., we designed the experimental setting in Section 2.2.10 to explore the influencing factors that affected cell viability. From the results of Section 3.3.4.1, clear evidence of interactions between the components of medium and irradiation was found. Riboflavin, a component of the DMEM, acted as a biomolecule and contributed to the photosensitization of free radical formation. In terms of ROS production following photosensitization, Bouillaguet et al. found ROS production by photoactivation requiring blue light (wavelength at 380 to 500 nm) exposure ¹⁵⁶. Eichler et al. revealed that the endogenous photosensitizer of riboflavin was responsible for ROS production in cardiac and sperm cells ¹⁵⁷. Our findings

indicate that photosensitization by riboflavin possibly contributed to the increased production of ROS during medium irradiation. During PBM, the increase in mitochondrial membrane potential plays a crucial role in stimulating electron transport, promoting the production of ROS¹⁵⁸. Multiple biological processes have proven to benefit from a low level of ROS. In our study, after medium irradiation with a low fluence of 4.5 or 6 J/cm², the produced ROS below the threshold could positively act on cell viability.

Based on the description in Section 2.2.10, treatments with medium irradiation followed by transfer also led to cell viability increases in non-irradiated cells. In this experimental setting, cells and medium were simultaneously exposed to BLI, with more influencing factors involved. Therefore, it cannot be explained by the aforementioned assumption regarding medium irradiation. Interestingly, the decline in cell viability with medium refreshment compared to cells without medium refreshment demonstrated the existence of promotive effects in the medium. Indeed, more research is required to delve into the mechanism and pinpoint the factors released by the cells in the medium. Currently, the existence of a combined biological effect from cell and medium irradiation can be concluded.

5 SUMMARY

The wound-healing properties of blue light irradiation have been well described in in vitro and in vivo models. In this study, we aim to systematically and precisely study the PBM after BLI (wavelength 450 nm) in vitro on skin cells—endothelial cells, keratinocytes, and fibroblasts involved in wound healing and angiogenesis—using an LED-based blue light irradiation device developed by URGO.

Biphasic effect and dose dependence were widely observed on these three cell lines, i.e., cellular response varies based on the dose of energy. In cell viability assays, we commonly found that a low fluence of irradiation with an irradiation time of less than 15 min stimulated cell viability. However, as radiant exposure increased, the inhibitory effect gradually became obvious. Particularly, when combined with findings of cell viability following a long-term irradiation lasting over 2 hours at an irradiance of 23 mW/cm², the significant reduction in cell viability indicated the presence of cytotoxicity. Measurement of BrdU assays also indicated the cell behaved biphasically to BLI. Surprisingly, cell proliferation was not obviously stimulated by any dose of BLI in HaCaTs.

Then sequential light treatments on cell lines were to verify the effectiveness of the booster effect (4.5 J/cm²) after the inhibitory effect of 2 and 5 h irradiation with 23 mW/cm². Through cell viability assays, the booster effect was proved to accelerate the recovery of cell viability after 2 h irradiation, whereas 5 h irradiation with 23 mW/cm² had profound impacts on cell viability of NHDFs and HUVECs. Combined with the consistent findings from ATP quantification, 2 h irradiation with the irradiance of 23 mW/cm² had a short-term influence on cellular metabolism. However, the continuous decreases in cell viability indicated potentially irreversible changes occurred after 5 h BLI with 23 mW/cm² on NHDFs and HUVECs.

Alteration of cell culture conditions, especially the medium irradiation and medium refreshment, induced changes in cell viability, such phenomena possibly attributed to the effect of medium components after irradiation. However, more explorations on mechanisms are still necessary in future studies.

RNA sequencing revealed the mechanism of PBM after 4.5 J/cm² and inhibition after 18 J/cm². NHDFs were stimulated by upregulation of ErbB, TGF- β , and VEGF pathways. While 18 J/cm² BLI mainly downregulated DNA replication, cell cycle, and mismatch repair pathways. Combining the findings from apoptosis assays, we

Summary

observed that 18 J/cm² BLI primarily influences cell proliferation, without noticeable effects on apoptosis or cell death.

6 REFERENCES

1. Bashir, H, Seykora, JT, Lee, V: Invisible shield: review of the corneal epithelium as a barrier to UV radiation, pathogens, and other environmental stimuli. *Journal of ophthalmic & vision research*, 12: 305, 2017.
2. Verma, A, Zanoletti, A, Kareem, KY, Adelodun, B, Kumar, P, Ajibade, FO, Silva, LF, Phillips, AJ, Kartheeswaran, T, Bontempi, E: Skin protection from solar ultraviolet radiation using natural compounds: a review. *Environmental Chemistry Letters*, 22: 273-295, 2024.
3. Montagna, W: *The structure and function of skin*, Elsevier, 2012.
4. Rawlings, A, Harding, C: Moisturization and skin barrier function. *Dermatologic therapy*, 17: 43-48, 2004.
5. Romanovsky, AA: Skin temperature: its role in thermoregulation. *Acta physiologica*, 210: 498-507, 2014.
6. Mohamed, SA, Harget, R: Surgical anatomy of the skin. *Surgery (Oxford)*, 40: 1-7, 2022.
7. Kanitakis, J: Anatomy, histology and immunohistochemistry of normal human skin. *European journal of dermatology*, 12: 390-401, 2002.
8. Menon, GK, Cleary, GW, Lane, ME: The structure and function of the stratum corneum. *International journal of pharmaceutics*, 435: 3-9, 2012.
9. Harding, CR: The stratum corneum: structure and function in health and disease. *Dermatologic therapy*, 17: 6-15, 2004.
10. Freedberg, IM, Tomic-Canic, M, Komine, M, Blumenberg, M: Keratins and the keratinocyte activation cycle. *Journal of Investigative Dermatology*, 116: 633-640, 2001.
11. Sotiropoulou, PA, Blanpain, C: Development and homeostasis of the skin epidermis. *Cold Spring Harbor perspectives in biology*, 4: a008383, 2012.
12. Halper, J, Kjaer, M: Basic components of connective tissues and extracellular matrix: elastin, fibrillin, fibulins, fibrinogen, fibronectin, laminin, tenascins and thrombospondins. *Progress in heritable soft connective tissue diseases*: 31-47, 2014.
13. Olczyk, P, Mencner, Ł, Komosinska-Vassev, K: The role of the extracellular matrix components in cutaneous wound healing. *BioMed research international*, 2014: 747584, 2014.

14. Venus, M, Waterman, J, McNab, I: Basic physiology of the skin. *Surgery (Oxford)*, 28: 469-472, 2010.
15. Sherratt, MJ: Tissue elasticity and the ageing elastic fibre. *Age*, 31: 305-325, 2009.
16. Gosline, JM: The physical properties of elastic tissue. *International review of connective tissue research*, 7: 211-249, 1976.
17. Bos, JD, Kapsenberg, ML: The skin immune system Its cellular constituents and their interactions. *Immunology Today*, 7: 235-240, 1986.
18. Metz, M, Siebenhaar, F, Maurer, M: Mast cell functions in the innate skin immune system. *Immunobiology*, 213: 251-260, 2008.
19. MOGHADDAM, FD, BERTANI, FR, TAY, F: Skin Anatomy. *Carrier-mediated Gene and Drug Delivery for Dermal Wound Healing*, 4, 2023.
20. Yamate, J: The skin and subcutis. In: *Boorman's pathology of the rat*. Elsevier, 2018, pp 323-345.
21. Walløe, L: Arterio-venous anastomoses in the human skin and their role in temperature control. *Temperature*, 3: 92-103, 2016.
22. Moore Jr, JE, Bertram, CD: Lymphatic system flows. *Annual review of fluid mechanics*, 50: 459-482, 2018.
23. Skobe, M, Detmar, M: Structure, function, and molecular control of the skin lymphatic system. *Journal of Investigative Dermatology Symposium Proceedings*. Elsevier, 2000 pp 14-19.
24. Olszewski, WL: The lymphatic system in body homeostasis: physiological conditions. *Lymphatic research and biology*, 1: 11-24, 2003.
25. BUILDER, V: LYMPHATIC SYSTEM REVIEW. *Mosby's Pathology for Massage Professionals-E-Book: Mosby's Pathology for Massage Professionals-E-Book*: 265, 2021.
26. Woo, WM: Skin structure and biology. *Imaging Technologies and Transdermal Delivery in Skin Disorders*: 1-14, 2019.
27. Starcher, B, Aycock, RL, Hill, CH: Multiple roles for elastic fibers in the skin. *Journal of Histochemistry & Cytochemistry*, 53: 431-443, 2005.
28. Walters, KA, Roberts, MS: The structure and function of skin. In: *Dermatological and transdermal formulations*. CRC press, 2002, pp 19-58.
29. Walters, KA, Roberts, MS: Skin Morphology, Development and Physiology. In: *Cosmetic Formulation*. CRC Press, 2019, pp 29-46.

30. Ghaben, AL, Scherer, PE: Adipogenesis and metabolic health. *Nature reviews Molecular cell biology*, 20: 242-258, 2019.
31. Gurtner, GC, Werner, S, Barrandon, Y, Longaker, MT: Wound repair and regeneration. *Nature*, 453: 314-321, 2008.
32. Scalise, A, Bianchi, A, Tartaglione, C, Bolletta, E, Pierangeli, M, Torresetti, M, Marazzi, M, Di Benedetto, G: Microenvironment and microbiology of skin wounds: the role of bacterial biofilms and related factors. *Seminars in vascular surgery*. Elsevier, 2015 pp 151-159.
33. Martins-Green, M, Petreaca, M, Wang, L: Chemokines and their receptors are key players in the orchestra that regulates wound healing. *Advances in wound care*, 2: 327-347, 2013.
34. Potekaev, NN, Borzykh, OB, Medvedev, GV, Pushkin, DV, Petrova, MM, Petrov, AV, Dmitrenko, DV, Karpova, EI, Demina, OM, Shnayder, NA: The role of extracellular matrix in skin wound healing. *Journal of Clinical Medicine*, 10: 5947, 2021.
35. Rodrigues, M, Kosaric, N, Bonham, CA, Gurtner, GC: Wound healing: a cellular perspective. *Physiological reviews*, 99: 665-706, 2019.
36. Barrientos, S, Stojadinovic, O, Golinko, MS, Brem, H, Tomic - Canic, M: Growth factors and cytokines in wound healing. *Wound repair and regeneration*, 16: 585-601, 2008.
37. Moulin, V: Growth factors in skin wound healing. *European journal of cell biology*, 68: 1-7, 1995.
38. Baum, CL, Arpey, CJ: Normal cutaneous wound healing: clinical correlation with cellular and molecular events. *Dermatologic surgery*, 31: 674-686, 2005.
39. Guo, Sa, DiPietro, LA: Factors affecting wound healing. *Journal of dental research*, 89: 219-229, 2010.
40. Hirt, PA, Castillo, DE, Yosipovitch, G, Keri, JE: Skin changes in the obese patient. *Journal of the American Academy of Dermatology*, 81: 1037-1057, 2019.
41. Anderson, K, Hamm, RL: Factors that impair wound healing. *Journal of the American College of Clinical Wound Specialists*, 4: 84-91, 2012.
42. Caldwell, MD: Bacteria and antibiotics in wound healing. *Surgical Clinics*, 100: 757-776, 2020.
43. Sen, CK: Human wound and its burden: updated 2020 compendium of estimates. *Advances in wound care*, 10: 281-292, 2021.

44. Suhag, D: Skin and Wound Healing Biomaterials. In: *Handbook of Biomaterials for Medical Applications, Volume 2: Applications*. Springer, 2024, pp 281-320.
45. Burgess, JL, Wyant, WA, Abdo Abujamra, B, Kirsner, RS, Jozic, I: Diabetic wound-healing science. *Medicina*, 57: 1072, 2021.
46. Wilkinson, HN, Hardman, MJ: Wound healing: cellular mechanisms and pathological outcomes. *Open biology*, 10: 200223, 2020.
47. Singh, S, Young, A, McNaught, C-E: The physiology of wound healing. *Surgery (Oxford)*, 35: 473-477, 2017.
48. Sedighi, M, Namdari, M, Mahmoudi, P: An overview of angiogenesis and chemical and physiological angiogenic factors: short review. *Journal of Chemical Health Risks*, 2023.
49. Honnegowda, TM, Kumar, P, Udupa, EGP, Kumar, S, Kumar, U, Rao, P: Role of angiogenesis and angiogenic factors in acute and chronic wound healing. *Plastic and Aesthetic Research*, 2: 243-249, 2015.
50. Liekens, S, De Clercq, E, Neyts, J: Angiogenesis: regulators and clinical applications. *Biochemical pharmacology*, 61: 253-270, 2001.
51. Mackman, N, Tilley, RE, Key, NS: Role of the extrinsic pathway of blood coagulation in hemostasis and thrombosis. *Arteriosclerosis, thrombosis, and vascular biology*, 27: 1687-1693, 2007.
52. Diller, RB, Tabor, AJ: The role of the extracellular matrix (ECM) in wound healing: a review. *Biomimetics*, 7: 87, 2022.
53. Zubair, M, Ahmad, J: Role of growth factors and cytokines in diabetic foot ulcer healing: a detailed review. *Reviews in Endocrine and Metabolic Disorders*, 20: 207-217, 2019.
54. Wang, J: Neutrophils in tissue injury and repair. *Cell and tissue research*, 371: 531-539, 2018.
55. Kolaczkowska, E, Kubes, P: Neutrophil recruitment and function in health and inflammation. *Nature reviews immunology*, 13: 159-175, 2013.
56. Phillipson, M, Kubes, P: The healing power of neutrophils. *Trends in immunology*, 40: 635-647, 2019.
57. Yussof, SJM, Omar, E, Pai, DR, Sood, S: Cellular events and biomarkers of wound healing. *Indian Journal of Plastic Surgery*, 45: 220-228, 2012.
58. Mathew-Steiner, SS, Roy, S, Sen, CK: Collagen in wound healing. *Bioengineering*, 8: 63, 2021.

59. Amar, S, Smith, L, Fields, GB: Matrix metalloproteinase collagenolysis in health and disease. *Biochimica et Biophysica Acta (BBA)-Molecular Cell Research*, 1864: 1940-1951, 2017.
60. Xue, M, Jackson, CJ: Extracellular matrix reorganization during wound healing and its impact on abnormal scarring. *Advances in wound care*, 4: 119-136, 2015.
61. Pastar, I, Stojadinovic, O, Yin, NC, Ramirez, H, Nusbaum, AG, Sawaya, A, Patel, SB, Khalid, L, Isseroff, RR, Tomic-Canic, M: Epithelialization in wound healing: a comprehensive review. *Advances in wound care*, 3: 445-464, 2014.
62. Wikramanayake, TC, Stojadinovic, O, Tomic-Canic, M: Epidermal differentiation in barrier maintenance and wound healing. *Advances in wound care*, 3: 272-280, 2014.
63. Rousselle, P, Braye, F, Dayan, G: Re-epithelialization of adult skin wounds: Cellular mechanisms and therapeutic strategies. *Advanced Drug Delivery Reviews*, 146: 344-365, 2019.
64. Chin, GA, Diegelmann, RF, Schultz, GS: Cellular and molecular regulation of wound healing. *Basic and Clinical Dermatology*, 33: 17, 2005.
65. Carvalho, JCO: *Dermal epidermal separation for skin rejuvenation*. Med. Dissertation. Medizinische Fakultät Mannheim, Universität Heidelberg, 2015.
66. Bainbridge, P: Wound healing and the role of fibroblasts. *Journal of wound care*, 22, 2013.
67. Harvanová, G, Duranková, S, Bernasovská, J: The role of cytokines and chemokines in the inflammatory response. *Alergologia Polska-Polish Journal of Allergology*, 10: 210-219, 2023.
68. Hartupee, J, Mann, DL: Role of inflammatory cells in fibroblast activation. *Journal of molecular and cellular cardiology*, 93: 143-148, 2016.
69. Davidson, S, Coles, M, Thomas, T, Kollias, G, Ludewig, B, Turley, S, Brenner, M, Buckley, CD: Fibroblasts as immune regulators in infection, inflammation and cancer. *Nature Reviews Immunology*, 21: 704-717, 2021.
70. Van Linthout, S, Miteva, K, Tschöpe, C: Crosstalk between fibroblasts and inflammatory cells. *Cardiovascular research*, 102: 258-269, 2014.
71. Grotendorst, GR: Connective tissue growth factor: a mediator of TGF- β action on fibroblasts. *Cytokine & growth factor reviews*, 8: 171-179, 1997.

72. Takehara, K: Growth regulation of skin fibroblasts. *Journal of dermatological science*, 24: S70-S77, 2000.

73. Narine, K, Wever, OD, Valckenborgh, DV, Francois, K, Bracke, M, Desmet, S, Mareel, M, Nooten, GV: Growth factor modulation of fibroblast proliferation, differentiation, and invasion: implications for tissue valve engineering. *Tissue Engineering*, 12: 2707-2716, 2006.

74. Farooq, M, Khan, AW, Kim, MS, Choi, S: The role of fibroblast growth factor (FGF) signaling in tissue repair and regeneration. *Cells*, 10: 3242, 2021.

75. Fernández-Guarino, M, Hernández-Bule, ML, Bacci, S: Cellular and molecular processes in wound healing. *Biomedicines*, 11: 2526, 2023.

76. Melrose, J: Glycosaminoglycans in wound healing. *Bone and Tissue Regeneration Insights*, 7: BTRI. S38670, 2016.

77. Caldeira, J, Sousa, A, Sousa, D, Barros, D: Extracellular matrix constitution and function for tissue regeneration and repair. In: *Peptides and proteins as biomaterials for tissue regeneration and repair*. Elsevier, 2018, pp 29-72.

78. Rousselle, P, Montmasson, M, Garnier, C: Extracellular matrix contribution to skin wound re-epithelialization. *Matrix Biology*, 75: 12-26, 2019.

79. Darby, IA, Laverdet, B, Bonté, F, Desmoulière, A: Fibroblasts and myofibroblasts in wound healing. *Clinical, cosmetic and investigational dermatology*: 301-311, 2014.

80. Singh, M, Yadav, R, Rehman, A, Solanki, PR: Wound healing and management. In: *Nanotechnological Aspects for Next-Generation Wound Management*. Elsevier, 2024, pp 55-69.

81. Karamysheva, A: Mechanisms of angiogenesis. *Biochemistry (Moscow)*, 73: 751-762, 2008.

82. van Hinsbergh, VW: Angiogenesis: basics of vascular biology. *Vascularization for Tissue Engineering and Regenerative Medicine*: 3-31, 2021.

83. Qutub, AA, Popel, AS: Elongation, proliferation & migration differentiate endothelial cell phenotypes and determine capillary sprouting. *BMC systems biology*, 3: 1-24, 2009.

84. Chen, W, Xia, P, Wang, H, Tu, J, Liang, X, Zhang, X, Li, L: The endothelial tip-stalk cell selection and shuffling during angiogenesis. *Journal of cell communication and signaling*, 13: 291-301, 2019.

85. Li, S, Huang, NF, Hsu, S: Mechanotransduction in endothelial cell migration. *Journal of cellular biochemistry*, 96: 1110-1126, 2005.
86. Tonnesen, MG, Feng, X, Clark, RA: Angiogenesis in wound healing. *Journal of investigative dermatology symposium proceedings*. Elsevier, 2000 pp 40-46.
87. Eming, SA, Brachvogel, B, Odorisio, T, Koch, M: Regulation of angiogenesis: wound healing as a model. *Progress in histochemistry and cytochemistry*, 42: 115-170, 2007.
88. Caporali, A, Martello, A, Miscianinov, V, Maselli, D, Vono, R, Spinetti, G: Contribution of pericyte paracrine regulation of the endothelium to angiogenesis. *Pharmacology & therapeutics*, 171: 56-64, 2017.
89. Wanjare, M, Kusuma, S, Gerecht, S: Perivascular cells in blood vessel regeneration. *Biotechnology journal*, 8: 434-447, 2013.
90. Mester, E, Szende, B, Spiry, T, Scher, A: Stimulation of wound healing by laser rays. *Acta chirurgica academiae scientiarum hungaricae*, 13: 315-324, 1972.
91. Mester, E, Mester, AF, Mester, A: The biomedical effects of laser application. *Lasers in surgery and medicine*, 5: 31-39, 1985.
92. Barolet, AC, Villarreal, AM, Jfri, A, Litvinov, IV, Barolet, D: Low-intensity visible and near-infrared light-induced cell signaling pathways in the skin: a comprehensive review. *Photobiomodulation, Photomedicine, and Laser Surgery*, 41: 147-166, 2023.
93. Crous, A, Abrahamse, H: The signalling effects of photobiomodulation on osteoblast proliferation, maturation and differentiation: a review. *Stem Cell Reviews and Reports*: 1-20, 2021.
94. Hamblin, MR: Mechanisms of photobiomodulation in the brain. In: *Photobiomodulation in the Brain*. Elsevier, 2019, pp 97-110.
95. Kashiwagi, S, Morita, A, Yokomizo, S, Ogawa, E, Komai, E, Huang, PL, Bragin, DE, Atochin, DN: Photobiomodulation and nitric oxide signaling. *Nitric Oxide*, 130: 58-68, 2023.
96. da Silva, TG, Ribeiro, RS, Mencalha, AL, de Souza Fonseca, A: Photobiomodulation at molecular, cellular, and systemic levels. *Lasers in Medical Science*, 38: 136, 2023.
97. Wang, Y, Huang, Y-Y, Wang, Y, Lyu, P, Hamblin, MR: Photobiomodulation (blue and green light) encourages osteoblastic-differentiation of human adipose-

derived stem cells: role of intracellular calcium and light-gated ion channels. *Scientific reports*, 6: 33719, 2016.

98. Terakita, A: The opsins. *Genome biology*, 6: 1-9, 2005.

99. Castellano - Pellicena, I, Uzunbajakava, NE, Mignon, C, Raafs, B, Botchkarev, VA, Thornton, MJ: Does blue light restore human epidermal barrier function via activation of Opsin during cutaneous wound healing? *Lasers in surgery and medicine*, 51: 370-382, 2019.

100. Wicks, NL, Chan, JW, Najera, JA, Ciriello, JM, Oancea, E: UVA phototransduction drives early melanin synthesis in human melanocytes. *Current Biology*, 21: 1906-1911, 2011.

101. Buscone, S, Mardaryev, AN, Raafs, B, Bikker, JW, Sticht, C, Gretz, N, Farjo, N, Uzunbajakava, NE, Botchkareva, NV: A new path in defining light parameters for hair growth: Discovery and modulation of photoreceptors in human hair follicle. *Lasers in surgery and medicine*, 49: 705-718, 2017.

102. Sikka, G, Hussmann, GP, Pandey, D, Cao, S, Hori, D, Park, JT, Steppan, J, Kim, JH, Barodka, V, Myers, AC: Melanopsin mediates light-dependent relaxation in blood vessels. *Proceedings of the National Academy of Sciences*, 111: 17977-17982, 2014.

103. Heiskanen, V, Hamblin, MR: Photobiomodulation: lasers vs. light emitting diodes? *Photochemical & Photobiological Sciences*, 17: 1003-1017, 2018.

104. Attinger, CE, Janis, JE, Steinberg, J, Schwartz, J, Al-Attar, A, Couch, K: Clinical approach to wounds: debridement and wound bed preparation including the use of dressings and wound-healing adjuvants. *Plastic and reconstructive surgery*, 117: 72S-109S, 2006.

105. Kramer, A, Dissemond, J, Kim, S, Willy, C, Mayer, D, Papke, R, Tuchmann, F, Assadian, O: Consensus on wound antisepsis: update 2018. *Skin pharmacology and physiology*, 31: 28-58, 2018.

106. Hosseini, M, Shafiee, A: Engineering bioactive scaffolds for skin regeneration. *Small*, 17: 2101384, 2021.

107. Boateng, J, Catanzano, O: Advanced therapeutic dressings for effective wound healing—a review. *Journal of pharmaceutical sciences*, 104: 3653-3680, 2015.

108. Dhivya, S, Padma, VV, Santhini, E: Wound dressings—a review. *BioMedicine*, 5: 22, 2015.

109. Suan, LP, Bidin, N, Cherng, CJ, Hamid, A: Light-based therapy on wound healing: a review. *Laser Physics*, 24: 083001, 2014.
110. Yadav, A, Gupta, A: Noninvasive red and near - infrared wavelength - induced photobiomodulation: promoting impaired cutaneous wound healing. *Photodermatology, photoimmunology & photomedicine*, 33: 4-13, 2017.
111. Walski, T, Dąbrowska, K, Drohomirecka, A, Jędruchniewicz, N, Trochanowska-Pauk, N, Witkiewicz, W, Komorowska, M: The effect of red-to-near-infrared (R/NIR) irradiation on inflammatory processes. *International Journal of Radiation Biology*, 95: 1326-1336, 2019.
112. Lohr, NL, Ninomiya, JT, Warltier, DC, Weihrauch, D: Far red/near infrared light treatment promotes femoral artery collateralization in the ischemic hindlimb. *Journal of molecular and cellular cardiology*, 62: 36-42, 2013.
113. Cicchi, R, Rossi, F, Alfieri, D, Bacci, S, Tatini, F, De Siena, G, Paroli, G, Pini, R, Pavone, FS: Observation of an improved healing process in superficial skin wounds after irradiation with a blue - LED haemostatic device. *Journal of Biophotonics*, 9: 645-655, 2016.
114. Cheon, MW, Kim, TG, Lee, YS, Kim, SH: Low level light therapy by Red–Green–Blue LEDs improves healing in an excision model of Sprague–Dawley rats. *Personal and ubiquitous computing*, 17: 1421-1428, 2013.
115. Mosti, G, Gasperini, S: Observations made on three patients suffering from ulcers of the lower limbs treated with Blue Light. *Chronic Wound Care Management and Research*: 23-28, 2018.
116. Marchelli, M, Perniciaro, G, Granara, D, Bedin, F, Di Leo, L, Viaggi, C, Orlando, G, Gagliano, C, Bottaro, L: Photobiomodulation with blue light in non-healing wounds: case series evaluation. *Wounds Int*, 10: 63-66, 2019.
117. Dini, V, Romanelli, M, Oranges, T, Davini, G, Janowska, A: Blue light emission in the management of hard-to-heal wounds. *Italian Journal of Dermatology and Venereology*, 156: 709-713, 2020.
118. Mellergaard, M, Fauvergne, S, Scarpa, C, Pozner, VL, Skov, S, Hebert, L, Nielsen, M, Bassetto, F, Téot, L: Evaluation of fluorescent light energy for the treatment of acute second-degree burns. *Military medicine*, 186: 416-423, 2021.

119. Kan, K, Mu, Y, Bouschbacher, M, Sticht, C, Kuch, N, Sigl, M, Rahbari, N, Gretz, N, Pallavi, P, Keese, M: Biphasic effects of blue light irradiation on human umbilical vein endothelial cells. *Biomedicines*, 9: 829, 2021.
120. Jaffe, EA, Nachman, RL, Becker, CG, Minick, CR: Culture of human endothelial cells derived from umbilical veins. Identification by morphologic and immunologic criteria. *The Journal of clinical investigation*, 52: 2745-2756, 1973.
121. Klapczynski, AS: *Influence of photobiomodulation with blue light on the metabolism, proliferation and gene expression of human fibroblasts*. Med. Dissertation. Medizinische Fakultät Mannheim, Universität Heidelberg, 2019.
122. Stańczyk, M, Van Rietbergen, B: Thermal analysis of bone cement polymerisation at the cement–bone interface. *Journal of biomechanics*, 37: 1803-1810, 2004.
123. Pan, Z, Shao, Y, Geng, Y, Chen, J, Su, L: The effect of heat stress on the cytoskeleton and cell cycle of human umbilical vein endothelial cell in vitro. *Zhonghua wei Zhong Bing ji jiu yi xue*, 27: 639-642, 2015.
124. Reissis, Y, García-Gareta, E, Korda, M, Blunn, GW, Hua, J: The effect of temperature on the viability of human mesenchymal stem cells. *Stem cell research & therapy*, 4: 1-11, 2013.
125. Wataha, J, Lewis, J, Lockwood, P, Hsu, S, Messer, R, Rueggeberg, F, Bouillaguet, S: Blue light differentially modulates cell survival and growth. *Journal of dental research*, 83: 104-108, 2004.
126. Fushimi, T, Inui, S, Nakajima, T, Ogasawara, M, Hosokawa, K, Itami, S: Green light emitting diodes accelerate wound healing: characterization of the effect and its molecular basis in vitro and in vivo. *Wound Repair and Regeneration*, 20: 226-235, 2012.
127. Quent, VM, Loessner, D, Friis, T, Reichert, JC, Hutmacher, DW: Discrepancies between metabolic activity and DNA content as tool to assess cell proliferation in cancer research. *Journal of cellular and molecular medicine*, 14: 1003-1013, 2010.
128. Balzer, J, Heuer, K, Demir, E, Hoffmanns, MA, Baldus, S, Fuchs, PC, Awakowicz, P, Suschek, CV, Opländer, C: Non-thermal dielectric barrier discharge (DBD) effects on proliferation and differentiation of human fibroblasts are primarily mediated by hydrogen peroxide. *PloS one*, 10: e0144968, 2015.

129. Becker, A, Klapczynski, A, Kuch, N, Arpino, F, Simon-Keller, K, De la Torre, C, Sticht, C, van Abeelen, FA, Oversluizen, G, Gretz, N: Gene expression profiling reveals aryl hydrocarbon receptor as a possible target for photobiomodulation when using blue light. *Scientific reports*, 6: 33847, 2016.
130. Masson-Meyers, DS, Bumah, VV, Enwemeka, CS: Blue light does not impair wound healing in vitro. *Journal of Photochemistry and Photobiology B: Biology*, 160: 53-60, 2016.
131. Mignon, C, Uzunbajakava, NE, Raafs, B, Moolenaar, M, Botchkareva, NV, Tobin, DJ: Photobiomodulation of distinct lineages of human dermal fibroblasts: a rational approach towards the selection of effective light parameters for skin rejuvenation and wound healing. *Mechanisms of Photobiomodulation Therapy XI*. SPIE, 2016 pp 27-42.
132. Zhang, H, Liu, S, Yang, X, Chen, N, Pang, F, Chen, Z, Wang, T, Zhou, J, Ren, F, Xu, X: LED phototherapy with gelatin sponge promotes wound healing in mice. *Photochemistry and photobiology*, 94: 179-185, 2018.
133. Jere, SW, Hourel, NN, Abrahamse, H: Photobiomodulation at 660 nm stimulates proliferation and migration of diabetic wounded cells via the expression of epidermal growth factor and the JAK/STAT pathway. *Journal of Photochemistry and Photobiology B: Biology*, 179: 74-83, 2018.
134. Karoussis, IK, Kyriakidou, K, Psarros, C, Afouxenides, P, Vrotsos, IA: Dosage Effects of an 810 nm Diode Laser on the Proliferation and Growth Factor Expression of Human Gingival Fibroblasts. *Journal of Lasers in Medical Sciences*, 12, 2021.
135. Schotanus, MD, Van Otterloo, E: Finding MEMO—emerging evidence for MEMO1's function in development and disease. *Genes*, 11: 1316, 2020.
136. Penn, JW, Grobbelaar, AO, Rolfe, KJ: The role of the TGF- β family in wound healing, burns and scarring: a review. *International journal of burns and trauma*, 2: 18, 2012.
137. Deng, Z, Fan, T, Xiao, C, Tian, H, Zheng, Y, Li, C, He, J: TGF- β signaling in health, disease, and therapeutics. *Signal transduction and targeted therapy*, 9: 61, 2024.
138. Mignon, C, Uzunbajakava, NE, Castellano - Pellicena, I, Botchkareva, NV, Tobin, DJ: Differential response of human dermal fibroblast subpopulations to

visible and near - infrared light: Potential of photobiomodulation for addressing cutaneous conditions. *Lasers in Surgery and Medicine*, 50: 859-882, 2018.

139. Melincovici, CS, Boșca, AB, Şuşman, S, Mărginean, M, Mihu, C, Istrate, M, Moldovan, I-M, Roman, AL, Mihu, CM: Vascular endothelial growth factor (VEGF)-key factor in normal and pathological angiogenesis. *Rom J Morphol Embryol*, 59: 455-467, 2018.

140. Shibuya, M: Vascular endothelial growth factor (VEGF) and its receptor (VEGFR) signaling in angiogenesis: a crucial target for anti-and pro-angiogenic therapies. *Genes & cancer*, 2: 1097-1105, 2011.

141. Ahmad, A, Nawaz, MI: Molecular mechanism of VEGF and its role in pathological angiogenesis. *Journal of Cellular Biochemistry*, 123: 1938-1965, 2022.

142. Czyz, M: HGF/c-MET Signaling in Melanocytes and Melanoma. *International journal of molecular sciences*, 19: 3844, 2018.

143. Conway, K, Price, P, Harding, KG, Jiang, WG: The molecular and clinical impact of hepatocyte growth factor, its receptor, activators, and inhibitors in wound healing. *Wound Repair and Regeneration*, 14: 2-10, 2006.

144. Yoshida, S, Yamaguchi, Y, Itami, S, Yoshikawa, K, Tabata, Y, Matsumoto, K, Nakamura, T: Neutralization of hepatocyte growth factor leads to retarded cutaneous wound healing associated with decreased neovascularization and granulation tissue formation. *Journal of investigative dermatology*, 120: 335-343, 2003.

145. Mak, KM, Png, CYM, Lee, DJ: Type V collagen in health, disease, and fibrosis. *The Anatomical Record*, 299: 613-629, 2016.

146. Hansen, NUB, Willumsen, N, Sand, JMB, Larsen, L, Karsdal, MA, Leeming, DJ: Type VIII collagen is elevated in diseases associated with angiogenesis and vascular remodeling. *Clinical biochemistry*, 49: 903-908, 2016.

147. Rohringer, S, Holnthoner, W, Chaudary, S, Slezak, P, Priglinger, E, Strassl, M, Pill, K, Mühleder, S, Redl, H, Dungel, P: The impact of wavelengths of LED light-therapy on endothelial cells. *Scientific reports*, 7: 10700, 2017.

148. Dungel, P, Hartinger, J, Chaudary, S, Slezak, P, Hofmann, A, Hausner, T, Strassl, M, Wintner, E, Redl, H, Mittermayr, R: Low level light therapy by LED of different wavelength induces angiogenesis and improves ischemic wound healing. *Lasers in surgery and medicine*, 46: 773-780, 2014.

149. Wang, Y, Wu, X, Chen, J, Amin, R, Lu, M, Bhayana, B, Zhao, J, Murray, CK, Hamblin, MR, Hooper, DC: Antimicrobial blue light inactivation of gram-negative pathogens in biofilms: in vitro and in vivo studies. *The Journal of infectious diseases*, 213: 1380-1387, 2016.
150. Angarano, V, Smet, C, Akkermans, S, Watt, C, Chieffi, A, Van Impe, JF: Visible light as an antimicrobial strategy for inactivation of *Pseudomonas fluorescens* and *Staphylococcus epidermidis* biofilms. *Antibiotics*, 9: 171, 2020.
151. Leanse, LG, Harrington, OD, Fang, Y, Ahmed, I, Goh, XS, Dai, T: Evaluating the potential for resistance development to antimicrobial blue light (at 405 nm) in Gram-negative bacteria: in vitro and in vivo studies. *Frontiers in Microbiology*, 9: 2403, 2018.
152. Avola, R, Graziano, ACE, Pannuzzo, G, Cardile, V: RETRACTED: Blue Light Induces Down-Regulation of Aquaporin 1, 3, and 9 in Human Keratinocytes. *Cells*, 7: 197, 2018.
153. Mamalis, A, Garcha, M, Jagdeo, J: Light emitting diode - generated blue light modulates fibrosis characteristics: Fibroblast proliferation, migration speed, and reactive oxygen species generation. *Lasers in surgery and medicine*, 47: 210-215, 2015.
154. Masson-Meyers, DS, Bumah, VV, Enwemeka, CS: A comparison of four methods for determining viability in human dermal fibroblasts irradiated with blue light. *Journal of Pharmacological and Toxicological Methods*, 79: 15-22, 2016.
155. Mignon, C, Uzunbajakava, N, Raafs, B, Botchkareva, NV, Tobin, DJ: Photobiomodulation of human dermal fibroblasts in vitro: decisive role of cell culture conditions and treatment protocols on experimental outcome. *Scientific reports*, 7: 2797, 2017.
156. Bouillaguet, S, Wataha, JC, Zapata, O, Campo, M, Lange, N, Schrenzel, J: Production of reactive oxygen species from photosensitizers activated with visible light sources available in dental offices. *Photomedicine and laser surgery*, 28: 519-525, 2010.
157. Eichler, M, Lavi, R, Shainberg, A, Lubart, R: Flavins are source of visible - light - induced free radical formation in cells. *Lasers in Surgery and Medicine: The Official Journal of the American Society for Laser Medicine and Surgery*, 37: 314-319, 2005.

REFERENCES

158. Hamblin, MR: Mechanisms and mitochondrial redox signaling in photobiomodulation. *Photochemistry and photobiology*, 94: 199-212, 2018.

7 APPENDIX

Response of HaCaTs to BLI in terms of change in cellular metabolic activity quantified via XTT assay

Time (min)	7 mW/cm ²	10 mW/cm ²	23 mW/cm ²
	Effect/ Dose (J/cm ²)/ Variation		
2.5	****/1.05/5.3%↑	ns/1.5/3.3%↑	****(Peak)/3.45/9.5%↑
5	****/2.1/7.8%↑	ns/3/2.9%↑	****/6.9/8.8%↑
7.5	****/3.15/5.9%↑	***(Peak)/4.5/6.7%↑	ns/10.35/1.2%↓
10	****/4.2/11.5%↑	* /6/5.5%↑	ns/13.8/3.6%↑
12	****(Peak)/5.04/11.5↑	ns/7.2/3.5%↑	****/16.56/8.1%↓
15	****/6.3/5.4%↓	ns/9/4.2%↑	**/20.7/5.5%↓
20	****/8.4/13.1%↓	***/12/7.7%↓	****/27.6/11.1%↓
30	****/12.6/23.2%↓	****/18/13.4%↓	****/41.4/12.8%↓
60	****/25.2/23.2%↓	****/36/18.7%↓	****/82.8/11.8%↓
90	****/37.8/13.4%↓	****/54/22.2%↓	****/124.2/14.2%↓
120	****/50.4/13.8%↓	****/72/19.8%↓	****/165.6/13.5%↓

Table 2: Statistic for Figure 21A. Using the one-way ANOVA, ****: p < 0.0001, ***: p < 0.001, **: p < 0.01, *: p < 0.05, ns: not statistically significant. Comparisons were performed between light treatment groups and non-treatment groups. Statistically significant differences are indicated by a nominal p-value < 0.05.

Response of HaCaTs to BLI in terms of change in cell proliferation quantified via BrdU assay

Time (min)	7 mW/cm ²	10 mW/cm ²	23 mW/cm ²
	Effect/ Dose (J/cm ²)/ Variation		
2.5	ns/1.05/2.2%↓	ns/1.5/3.4%↓	ns (Peak)/3.45/1.8%↑
5	ns (Peak)/2.1/2.7%↑	ns/3/2.8%↓	ns/6.9/1.8%↑
7.5	ns/3.15/2.2%↑	ns /4.5/0.8%↑	ns/10.35/2.9%↓
10	ns/4.2/0.1%↓	ns(Peak)/6/1.7%↑	ns/13.8/4.9%↓
12	ns/5.04/3.3%↓	ns/7.2/3.3%↓	ns/16.56/1.1%↓
15	* /6.3/4.8%↓	* /9/5.1%↓	ns/20.7/2.4%↓
20	****/8.4/11.1%↓	****/12/9.5%↓	* /27.6/5.6%↓
30	****/12.6/11.2%↓	****/18/11.2%↓	* /41.4/5.2%↓
60	****/25.2/13.8%↓	****/36/8.8%↓	****/82.8/17.3%↓
90	****/37.8/13.3%↓	****/54/10.1%↓	****/124.2/14.3%↓
120	****/50.4/16.0%↓	****/72/15.1%↓	****/165.6/31.2%↓

Table 3: Statistic for Figure 21B. Using the one-way ANOVA, ****: p < 0.0001, *: p < 0.05, ns: not statistically significant. Comparisons were performed between light treatment groups and non-treatment groups. Statistically significant differences are indicated by a nominal p-value < 0.05.

Response of NHDFs to BLI in terms of change in cellular metabolic activity quantified via XTT assay

Time (min)	7 mW/cm ²			10 mW/cm ²			23 mW/cm ²		
	Effect/ Dose (J/cm ²)/ Variation								
2.5	ns/1.05/2.1%↑			ns/1.5/2.5%↑			ns/3.45/2.6%↓		
5	ns (Peak)/2.1/3.1%↑			ns/3/4.0%↑			ns/6.9/1.0%↑		
7.5	ns/3.15/1.8%↓			**(Peak)/4.5/8.9%↑			* (Peak)/10.35/6.4%↑		
10	ns/4.2/2.6%↑			ns/6/0.8%↓			****/13.8/10.2%↓		
12	****(Peak)/5.04/10%↑			ns/7.2/1.6%↓			*/16.56/5.7%↓		
15	ns/6.3/2.1%↓			****/9/13.0%↓			****/20.7/10.9%↓		
20	****/8.4/8.9%↓			**/12/8.9%↓			****/27.6/13.9%↓		
30	****/12.6/10.7%↓			****/18/16.0%↓			****/41.4/14.7%↓		
60	****/25.2/12.4%↓			**/36/8.7%↓			****/82.8/26.2%↓		
90	**/37.8/6.1%↓			****/54/16.1%↓			****/124.2/10.9%↓		
120	****/50.4/11.6%↓			****/72/18.6%↓			****/165.6/17.0%↓		

Table 4: Statistic for Figure 22A. Using the one-way ANOVA, ****: p<0.0001, ***: p<0.001, **: p<0.01, *: p < 0.05, ns: not statistically significant. Comparisons were performed between light treatment groups and non-treatment groups. Statistically significant differences are indicated by a nominal p-value < 0.05.

Response of NHDFs to BLI in terms of change in cell proliferation quantified via BrdU assay

Time (min)	7 mW/cm ²			10 mW/cm ²			23 mW/cm ²		
	Effect/ Dose (J/cm ²)/ Variation								
2.5	****(Peak)/1.05/8.8%↑			ns/1.5/0.6%↑			ns/3.45/3.9↓		
5	ns/2.1/3.6%↓			ns/3/1.9%↓			ns/6.9/1.7%↓		
7.5	*/3.15/4.8%↓			**(Peak)/4.5/6.8%↑			ns/10.35/0.4%↑		
10	***/4.2/6.8%↓			ns/6/0.5%↑			ns/13.8/4.3↓		
12	***/5.04/6.2%↓			ns/7.2/0.4%↑			****(Peak)/16.56/13.3%↑		
15	ns/6.3/3.3%↓			**/9/6.4%↓			ns/20.7/5.9%↑		
20	****/8.4/9.7%↓			***/12/9.9%↓			ns/27.6/0.4%↓		
30	****/12.6/8.9%↓			*/18/13.9%↓			****/41.4/11.8%↓		
60	****/25.2/11.5%↓			***/36/9.5%↓			****/82.8/14.8%↓		
90	****/37.8/14.3%↓			***/54/11.4%↓			****/124.2/20.7%↓		
120	****/50.4/18.2%↓			***/72/15.2%↓			****/165.6/47.8%↓		

Table 5: Statistics for Figure 22B. Using the one-way ANOVA, ****: p < 0.0001, ***: p < 0.001, **: p < 0.01, *: P < 0.05, ns: not statistically significant. Comparisons were performed between light treatment groups and non-treatment groups. Statistically significant differences are indicated by a nominal p-value < 0.05.

Response of HUVECs to BLI in terms of change in cellular metabolic activity quantified via XTT assay

Time (min)	7 mW/cm ²	10 mW/cm ²	23 mW/cm ²
	Effect/ Dose (J/cm ²)/ Variation		
2.5	ns/1.05/0.4%↑	ns/1.5/1.2%↑	ns/3.45/1.0%↑
5	ns/2.1/2.8%↓	ns/3/0.7%↑	ns/6.9/0.9%↑
7.5	ns/3.15/3.9%↓	ns/4.5/0.6%↑	ns/10.35/2.2%↑
10	ns/4.2/1.3%↑	**(Peak)/6/8.1%↑	*(Peak)/13.8/5.9%↑
12	****(Peak)/5.04/13.7%↑	ns/7.2/1.7%↑	ns/16.56/3.6%↑
15	****/6.3/6.5%↑	ns/9/1.2%↓	ns/20.7/2.9%↓
20	ns/8.4/0.03%↓	ns/12/3.4%↓	**/27.6/7.3%↓
30	**/12.6/5.4%↓	****/18/11.1%↓	****/41.4/10.5%↓
60	****/25.2/8.6%↓	****/36/14.4%↓	****/82.8/8.1%↓
90	****/37.8/7.1%↓	**/54/11.4%↓	**/124.2/8.0%↓
120	****/50.4/9.3%↓	****/72/16.4%↓	****/165.4/12.8%↓

Table 6: statistic for Figure 23A. Using the one-way ANOVA, ****: p < 0.0001, ***: p < 0.001, **: p < 0.01, *: p < 0.05, ns: not statistically significant. Comparisons were performed between light treatment groups and non-treatment groups. Statistically significant differences are indicated by a nominal p-value < 0.05.

Response of HUVECs to BLI in terms of change in cell proliferation quantified via BrdU assay

Time (min)	7 mW/cm ²	10 mW/cm ²	23 mW/cm ²
	Effect/ Dose (J/cm ²)/ Variation		
2.5	**/1.05/7.5%↑	ns/1.5/0.5%↓	***/3.45/6.3%↑
5	**/2.1/7.4%↑	ns/3/0.1%↑	****(Peak)/6.9/11.7%↑
7.5	****(Peak)/3.15/16.1%↑	*(Peak)/4.5/5.9%↑	***/10.35/7.2%↑
10	****/4.2/15.2%↑	ns/6/3.3%↑	ns/13.8/2.2%↓
12	ns/5.04/4.7%↑	ns/7.2/1.4%↓	ns/16.56/4.3%↓
15	ns/6.3/4.9%↑	ns/9/1.8%↓	ns/20.7/4.8%↓
20	ns/8.4/0.7%↓	ns/12/0.7%↓	****/27.6/9.4%↓
30	**/12.6/7.3%↓	ns/18/3.1%↓	****/41.4/8.7%↓
60	****/25.2/9.4%↓	**/36/7.9%↓	****/82.8/9.5%↓
90	****/37.8/9.5%↓	****/54/11.2%↓	****/124.2/10.5%↓
120	****/50.4/11.2%↓	****/72/14.0%↓	****/165.6/12.6%↓

Table 7: statistic for Figure 23B. Using the one-way ANOVA, ****: p<0.0001, ***: p < 0.001, **: p < 0.01, *: p < 0.05, ns: not statistically significant. Comparisons were performed between light treatment groups and non-treatment groups. Statistically significant differences are indicated by a nominal p-value < 0.05.

8 CURRICULUM VITAE AND PUBLICATIONS

Personal information

Name : Jingbo Shao

Date of birth: 13.10.1989

Place of birth: Changshu, Jiangsu Province, China

Father: Shigang Shao

Mother Yanmin Wu

Education

10/2019 – Present	Dr. sc. hum Department of Surgery, University Medical Center Mannheim, Medical Faculty Mannheim, Heidelberg University, Mannheim, Germany Doctor Thesis: Photobiomodulation of blue light irradiation on human keratinocytes, fibroblasts and endothelia cells involved in wound healing and angiogenesis
09/2023 – 07/2016	Master's Degree of Medicine Department of interventional radiology, The First Affiliated Hospital of Soochow University, Soochow University, Suzhou, Jiangsu Province, China Master thesis: The application and value of TcPO ₂ in evaluating the degree of lower extremity ischemia reperfusion injury of rabbits
09/2008 – 07/2013	Bachelor's Degree of Medicine Medical school of Nantong University, Nantong, Jiangsu Province, China

Publications:

First authorship

1. **Shao J**, Zhou Q, Jin F, Reissfelder C, Sigl M, Yagublu V, Keese M. A Systematic Review and Bayesian Network Meta-Analysis on the Effect of Different Anticoagulants on the Prophylaxis of Post-Thrombotic Syndrome after Deep Venous Thrombosis. *Journal of Clinical Medicine*. 2023 Nov 30;12(23):7450.

2. **Shao J**, Clément S, Reissfelder C, Téoule P, Gretz N, Guo F, Hajizada S, Uhlig S, Mößinger K, de la Torre C et al. Photobiomodulation of 450 nm Blue Light on Human Keratinocytes, Fibroblasts, and Endothelial Cells: An In Vitro and Transcriptomic Study on Cells Involved in Wound Healing and Angiogenesis. *Biomedicines*. 2025 Aug 1;13:1876.

Co-authorship

1. Jin F, Yang Z, **Shao J**, Tao J, Reißfelder C, Loges S, Zhu L, Schölch S. ARID1A mutations in lung cancer: biology, prognostic role, and therapeutic implications. *Trends in Molecular Medicine*. 2023 Aug 1;29(8):646-58.
3. Jin F, Zhu L, **Shao J**, Yakoub M, Schmitt L, Reißfelder C, Loges S, Benner A, Schölch S. Circulating tumour cells in patients with lung cancer universally indicate poor prognosis. *European Respiratory Review*. 2022 Dec 31;31(166).

9 ACKNOWLEDGEMENT

First of all, I would like to thank Prof. Michael Keese for his very patient supervision during my research career as a Dr. sc. hum candidate in Germany. Without his guidance, I would not have been able to engage with and complete such an intriguing topic on blue light irradiation. Meanwhile, I am also quite grateful for the supervision of Prof. Norbert Gretz. Even though I never have the chance to express my gratitude to him directly, I value the experience that he brought to the project and will always remember his support and suggestions. Without his assistance, I would not have been able to achieve significant improvements over the past few years. I am grateful for the collaboration with URGO and thankful for the invitation to let me join the international project.

Secondly, I would like to thank Dr. Vugar Yagublu and Dr. Yusuf Muhammed for the continuous support during the past two years. I really appreciate the trust and inspiration from our group members. I really like the feeling of wholly integrating into the research group and being full of energy to complete the task of research every day. I would like to present my thankfulness to PD. Patrick Téoule, Prof. Sebastian Schölch, and Prof. Christoph Reißfelder for providing a wonderful platform, which is a helpful support to ensure the completion of my project.

Simultaneously, I want to thank the Next Generation Sequencing and FlowCore of the Medical Faculty Mannheim in Heidelberg University. I am particularly grateful to Dr. Carolina De La Torre, Dr. Carsten Sticht, and Stefanie Uhlig for their invaluable help with RNA sequencing and flow cytometry. Thank you all, my colleagues in the surgical lab at UMM. I got a lot of mental support from our daily conversations and discussions.

Last but not least, I want to express my immense thankfulness to my parents and wife. Without their advice, patience, understanding, and love, I should not have the courage to continue my study and complete my journey as a student abroad.